CHAPTER FIVE

Flow Boiling and Flow Condensation in Reduced Gravity

Issam Mudawar
Purdue University Boiling and Two-Phase Flow Laboratory (PU-BTPFL), School of Mechanical Engineering, West Lafayette, IN, United States

Contents

Abstract

Future space missions are projected to increase greatly in scope, complexity, and duration compared to previous space endeavors and bring about unprecedented increases in power requirements and heat dissipation demands. These challenges will necessitate substantial reductions in weight to power ratio of the propulsion system, as well as weight of the space vehicle's subsystems, including the Thermal Control System (TCS) responsible for controlling the temperature and humidity of the internal operating

Advances in Heat Transfer, Volume 49
ISSN 0065-2717
https://doi.org/10.1016/bs.aiht.2017.06.002

environment. Achieving these weight reductions will require detailed understanding of the influence of reduced gravity on two-phase flow and heat transfer in both the propulsion power cycle and the TCS. This chapter will review published literature concerning reduced gravity flow boiling and flow condensation mechanisms and predictive tools that are crucial to the design of future space vehicles. Particular focus is placed on recent parabolic flight findings from NASA's Flow Boiling and Condensation Experiment (FBCE) and plans for insertion of the FBCE into the International Space Station.

NOMENCLATURE

A area
A^+ parameter in eddy diffusivity model
$A_{f,*}$ cross-sectional area of liquid control volume
A_w area of wetting front
a acceleration; empirical coefficient
Bo Bond number
b ratio of wetting front length to wavelength
c interfacial wave speed
c_p specific heat at constant pressure
c_r real component of wave speed
D_F equivalent diameter in Froude number criterion
D_H hydraulic diameter
D_i inner diameter of condensation tube
D_o outer diameter of condensation tube
Fr Froude number
G mass velocity of FC-72
g gravity
g_e Earth gravity
g_n component of gravity normal to heated wall
G_w mass velocity of water
H height of channel's cross-section
H_1 heated wall 1
H_2 heated wall 2
h local heat transfer coefficient
H_f mean thickness of liquid layer
h_{fg} latent heat of vaporization
H_g mean thickness of vapor layer
j superficial velocity
K Von-Karman constant
k thermal conductivity; wave number ($2\pi/\lambda$)
L heated length
L_{char} characteristic length
L_d flow channel's flow development length
L_e flow channel's exit length
L_h flow channel's heated length
n empirical exponent

P pressure
P_f perimeter
Pr Prandtl number
Pr_T turbulent Prandtl number
q'' heat flux
q''_m critical heat flux (CHF)
q''_w wetting front lift-off heat flux
Re Reynolds number
T temperature
t time
ΔT_{sat} wall superheat, $T_w - T_{sat}$
$\Delta T_{sub,out}$ outlet subcooling, $T_{sat,out} - T_{b,out}$
U mean liquid inlet velocity
u axial velocity
U_f mean velocity of liquid layer
U_g mean velocity of vapor layer
$U_{g,n}$ mean vapor velocity in wetting front normal to heated wall
U_∞ bubble rise velocity
u^* friction velocity
W heated width of Flow Boiling Module (FBM); channel width of Condensation Module for Flow Visualization (CM-FV)
We Weber number
We_L Weber number based on heated length
x_e thermodynamic equilibrium quality
y distance perpendicular to the wall
y^+ dimensionless distance perpendicular to the wall
z stream-wise coordinate
z_o distance from leading edge of heated wall to location where vapor velocity just surpasses liquid velocity

GREEK SYMBOLS

Γ_{fg} condensation mass transfer rate per unit axial distance
δ mean vapor layer thickness; liquid film thickness
ε_m eddy momentum diffusivity
η interfacial perturbation
η_0 amplitude of interfacial perturbation
λ interfacial wavelength
λ_c critical wavelength
μ dynamic viscosity
ν kinematic viscosity
ρ density
ρ'' modified density
σ surface tension
τ shear stress
θ flow orientation angle

SUBSCRIPTS

b bulk liquid
c vapor core
crit critical
f saturated liquid
g saturated vapor
H horizontal flow
i interfacial
in inlet to heated wall; inlet to condensation length
out outlet from heated length; outlet of condensation length
sat saturation
tp two-phase region
w wetting front; wall; water
z axial direction

1. INTRODUCTION

1.1 Research Needs to Support Future Space Missions

Following the Apollo manned missions to the Moon in the 1960s and 1970s, interest shifted gradually to manned missions to asteroids and to Mars, which are expected to greatly increase mission scope, complexity, and duration compared to previous space endeavors. Associated with these challenges are unprecedented increases in both power requirements and heat dissipation demands [1–3].

It is presently widely acknowledged that traditional chemical propulsion systems are performance plateaued. Therefore, new energetic propulsion technologies promising very high power will be needed to achieve faster travel and greatly expanded deep space reach, while reducing specific mass (kg/kWe). Several propulsion technologies are presently under consideration, including Solar Electric Propulsion (SEP) as well as fission-based Nuclear Thermal Propulsion (NTP) and Nuclear Electric Propulsion (NEP). Nuclear fission options are expected to alleviate key shortcomings of SEP by greatly increasing power and decreasing specific mass. Present goals include developing a multimegawatt fission power system with a specific mass of 5 kg/kWe, compared to the 10 kg/kWe attainable with present liquid metal power cycles. Achieving this specific mass goal will require increasing reactor operating temperature and efficiency, as well as increasing heat rejection temperature to minimize radiator area. These goals will require detailed understanding of the influence of reduced gravity on liquid

metal two-phase fluid flow and heat transfer, supported by predictive design tools that are simply unavailable today.

Another research need that is crucial to future space missions is reducing specific mass of all space vehicle subsystems. This includes the Thermal Control System (TCS) responsible for controlling the temperature and humidity of the operating environment in vehicles (as well as planetary bases). The TCS must tackle three primary tasks: heat acquisition, heat transport, and heat rejection [4]. Heat acquisition components acquire heat from several sources and transfer it to the TCS loop, heat transport components move the heat to heat rejection components, and the latter reject the heat by radiation to deep space. Unlike current single-phase liquid TCS technologies, which rely entirely on sensible heat rise of the working fluid to remove the heat, a two-phase TCS would capitalize upon both sensible and latent heat to achieve orders of magnitude enhancement in heat transfer performance and therefore greatly decrease specific mass compared to single-phase TCS counterparts. Understanding the influence of reduced gravity on two-phase fluid physics and heat transfer is therefore crucial to the development of a two-phase TCS.

The importance of two-phase flow and heat transfer to future space missions is evident from findings of several workshops that culminated in specific recommendations concerning the need to adopt flow boiling and condensation in space propulsion, thermal control, and advanced life support systems. In a 2011 report by the National Research Council (NRC) [5], panels representing several science and engineering national academies provided an agenda for critical research needs in both physical and life sciences for future space exploration. Throughout the report, specific recommendations were made that place heavy emphasis on reduced-gravity two-phase flow and heat transfer, including the need for databases, correlations, theoretical models, and computational tools.

1.2 Influence of Reduced Gravity on Flow Boiling and Condensation

Because of large density differences between liquid and vapor, buoyancy can play a very influential role in dictating the motion of the vapor relative to the liquid and therefore in influencing heat transfer in both flow boiling and condensation [6]. High cost, hardware complexity, and sparse data that researchers are able to obtain from short-duration microgravity experiments, compounded by limited access to testing onboard the International Space Station (ISS), are all reasons behind the relatively small body of literature

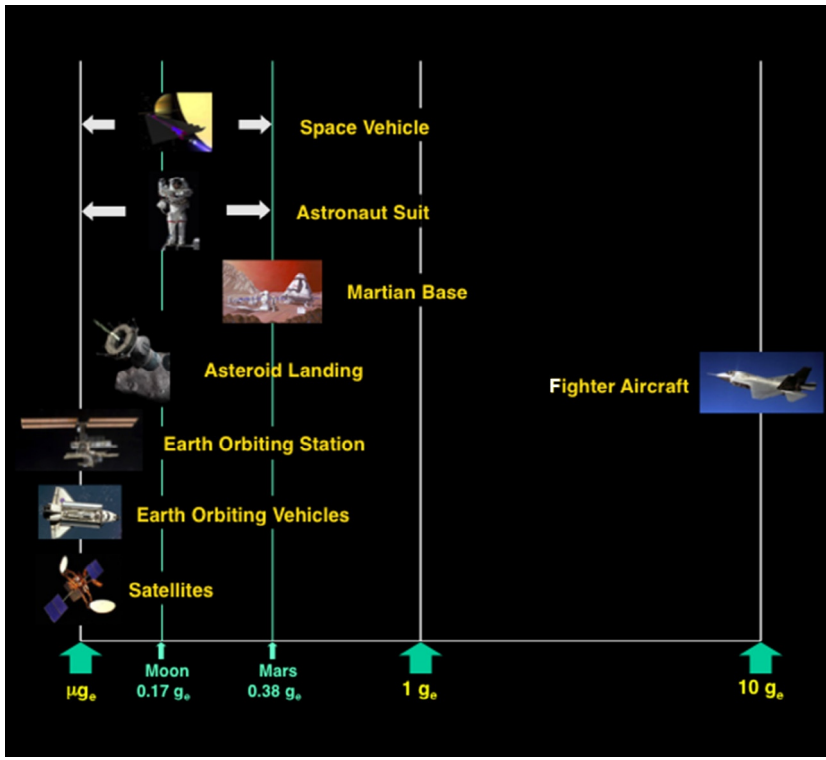

Fig. 1 Examples of systems demanding predictive models for effects of gravity on two-phase flow and heat transfer.

on two-phase transport phenomena in reduced gravity. In fact, most of the two-phase fluid flow and heat transfer know-how amassed over nearly a century of research come from experiments that have been conducted in Earth gravity. This is why it is impossible to rely on published predictive phase change correlations or models for reduced gravity conditions, especially microgravity. As shown in Fig. 1, space missions span a fairly broad range of gravities, including microgravity, for satellites and Earth-orbiting vehicles and stations, as well as Lunar and Martian gravities. Therefore, there is an urgent need to assess exiting predictive tools, or develop new ones, to tackle the complexities of operation in reduced gravity.

1.3 Microgravity Testing Platforms

Researchers have used several types of platforms to perform microgravity experiments. Among the most popular are *above ground drop tower* and *below ground drop shaft* facilities. They consist of tall vertical conduits within which

the experimental package is dropped to achieve microgravity during free fall. While these facilities offer high-quality microgravity ($<1 \times 10^{-4}\ g_e$), their key drawback is short test duration. For example, NASA Glenn Research Center's (GRC's) 24-m drop tower and 132-m drop shaft, and NASA Marshall Space Flight Center's 105-m drop tower provide microgravity durations of only 2.2, 5.2, and 4.6 s, respectively. Other examples are Germany Drop Tower Bremen's (ZARM's) 110-m, 4.72-s drop tower, and Japan Microgravity Center's (JAMIC's) 700-m, 10-s drop shaft [7]. Because of short microgravity duration, these facilities are generally used to perform preliminary experiments before more comprehensive long-duration experiments are carried out onboard the ISS.

Another option for microgravity testing is sounding rockets, suborbital carriers that provide 3–13 min of low gravity [8]. Their key drawbacks are limited amount of data available from a single launch and lack of manual interaction with the experimental package.

Parabolic flight aircraft provide a cost-effective means to performing microgravity experiments, with durations ranging from 15 to 30 s. The microgravity period is achieved several tens of times as the aircraft undergoes a series of parabolic maneuvers, with each parabola preceded and followed by short high gravity durations. One drawback of these experiments is relatively high gravity jitter ($\pm 0.01\ g_e$), and microgravity control is influenced by both pilot skills and weather conditions. Nonetheless, parabolic flight experiments provide several important advantages over drop tower and drop shafts, including longer microgravity duration, ability to accommodate larger experimental packages, and direct operator interaction during the experiment.

Since the retirement of the Space Shuttle fleet, the ISS has emerged as the ultimate microgravity testing platform, providing several crucial advantages over the afore-mentioned platforms, including long test duration, quasi-steady environment below $1 \times 10^{-4}\ g_e$, operator access to the experimental package, and both automatic and remote control capabilities [8]. But ISS experiments are very expensive and authorized only after many years of development and safety certification. These limitations have been responsible for significant delays in performing much needed microgravity experiments.

1.4 The NASA Flow Boiling and Condensation Experiment for the ISS

As discussed earlier, there is now strong conviction at NASA concerning the immense importance of developing both fundamental understanding and

predictive tools for two-phase heat transfer in microgravity. In 2002, NASA supported a research initiative at the Purdue University Boiling and Two-Phase Flow Laboratory (PU-BTPFL) to investigate the influence of reduced gravity on flow boiling critical heat flux (CHF). This was followed a decade later by NASA's launching of the Flow Boiling and Condensation Experiment (FBCE), a long-term project aimed at addressing research needs in both flow boiling and flow condensation. This project is a collaborative effort between the PU-BTPFL and the NASA-GRC. It involves initial ground and parabolic flight experiments, and development of an experimental package for insertion into the Fluid Integrated Rack (FIR) onboard the ISS in early 2019. As shown in Fig. 2, the FBCE will accommodate three separate test modules: the Flow Boiling Module (FBM), the Condensation Module for Heat Transfer Measurements (CM-HT), and the Condensation Module for Flow Visualization (CM-FV), using *n*-perfluorohexane (*n*PFH), C_6F_{14}, as working fluid.

NASA's ultimate goal for the FBCE is to serve as an integrated two-phase flow boiling and condensation facility for the ISS to meet the needs of the research community at large in obtaining microgravity two-phase flow and heat transfer data. Key objectives for the first set of experiments using the FBCE are to:

(a) obtain flow boiling pressure drop and heat transfer databases in long-duration microgravity experiments;

(b) obtain flow condensation pressure drop and heat transfer databases in long-duration microgravity experiments;

(c) develop an experimentally validated, mechanistic model for flow boiling CHF in microgravity, and dimensionless criteria to predict the minimum flow rate required to ensure gravity-independent CHF;

(d) develop an experimentally validated, mechanistic model for condensation in microgravity, and dimensionless criteria to predict the minimum flow rate required to ensure gravity-independent annular condensation, and also develop predictive methods for other condensation regimes.

1.5 Objectives of This Chapter

This chapter will review published literature concerning two-phase flow and heat transfer in reduced gravity, including mechanisms, correlations, and mechanistic models for both flow boiling and condensation. Also addressed are fundamental differences in two-phase interfacial behavior

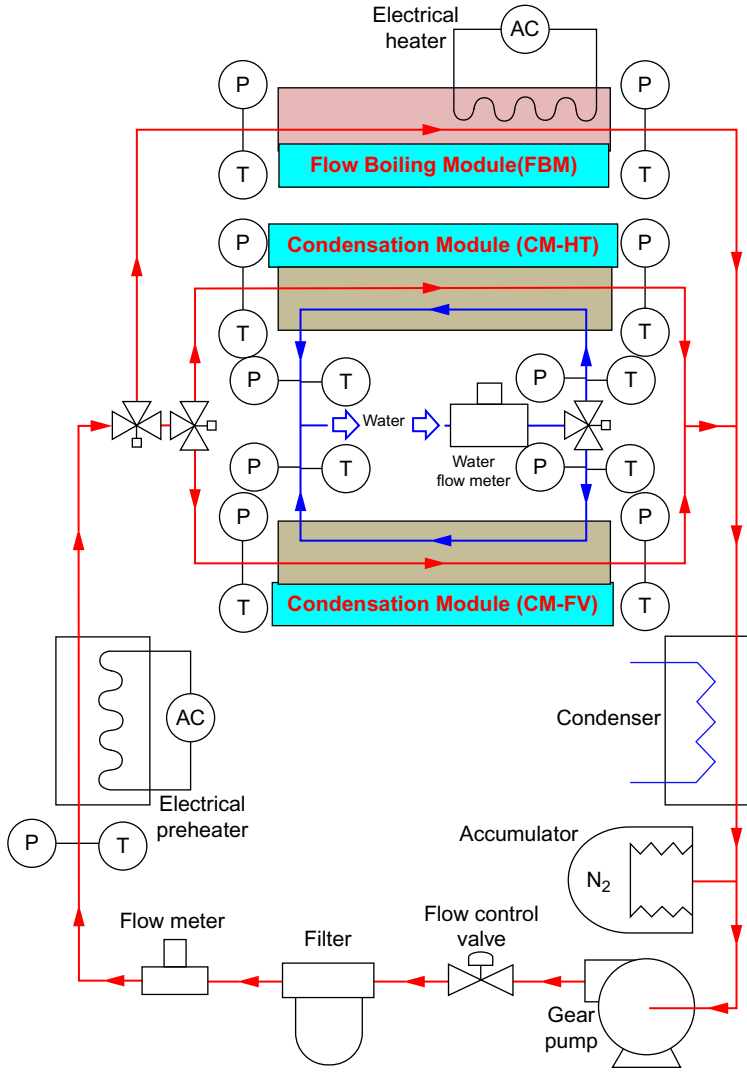

Fig. 2 Basic layout of the Flow Boiling and Condensation Experiment (FBCE) for the ISS.

between Earth gravity and microgravity for both flow boiling and condensation, which pose serious uncertainty when implementing available predictive tools for design of two-phase hardware in space systems.

As a principal investigator for the 2002 NASA flow boiling CHF study and the 2012 FBCE's science team, the author of this study will focus attention on recent findings from both projects, including (1) ground flow boiling

and condensation experiments performed at different flow orientations relative to Earth gravity, and (2) parabolic flight microgravity flow boiling and condensation experiments. These experiments have played a crucial role in developing mechanistic models for reduced gravity two-phase flow and heat transfer and served as foundation for development of the FBCE for the ISS.

2. FLOW BOILING HEAT TRANSFER AND CHF IN REDUCED GRAVITY

2.1 Optimum Flow Boiling Configuration for Space Thermal Management

As indicated earlier, heat acquisition is a key function of the TCS in a space vehicle. In a two-phase TCS, the heat is removed by boiling the working fluid in a closed flow loop. In terrestrial systems, boiling is possible using a variety of configurations summarized in a series of articles by the present author [9–11], including pool boiling [12,13], capillary [14], falling film [15], channel flow [16], microchannel [17–19], jet [20–22], and spray [23,24], as well as hybrid schemes combining the merits of microchannel flow and jet impingement [25]. As will be discussed later, in the absence of an effective means to remove vapor from the heat-dissipating surface, pool boiling is highly problematic in reduced gravity. Likewise, reliance on gravity precludes falling film cooling as a viable means for heat acquisition in reduced gravity. And, while all other boiling configurations take advantage of a mechanical pump to both circulate the coolant and combat vapor accumulation along heat-dissipating surfaces, some of these schemes pose a variety of challenges when implemented in reduced gravity. For example, microchannels, jets, and sprays can greatly increase the pressure drop across the boiling module. In addition, jets are often used in multiple arrays to ensure surface temperature uniformity, which can greatly increase the coolant flow rate and therefore pumping power. Sprays are difficult to implement because of an inability to expel the spent liquid following impact in the absence of gravity. These facts point to channel flow boiling as the most effective means for reduced gravity thermal management, providing the benefits of low pressure drop, low to moderate coolant flow rate, and ease of implementation in a boiling module. Given the high cost of performing boiling experiments in reduced gravity, most recent microgravity flow boiling experiments, including the FBCE, are based on channel flow boiling.

2.2 Models and Correlation for Flow Boiling CHF at 1 g_e

CHF is arguably the most important design parameter for a two-phase thermal management system involving heat-flux-controlled surfaces, including reduced gravity TCS. CHF occurrence is associated with appreciable reduction in the magnitude of the heat transfer coefficient resulting from interrupted liquid access to the heated surface, which culminates in unsteady escalation in the surface temperature. Depending on the prevailing two-phase flow pattern in the flow passage, CHF can be manifest in one of two forms: *Dryout* and *Departure from Nucleate Boiling (DNB)* [11]. The former is generally associated with annular flow and commences when the annular liquid film is consumed by evaporation. On the other hand, DNB is encountered mostly with subcooled inlet conditions, high mass velocities, and short channels. Occurring mostly in the bubbly flow region, DNB is the result of localized vapor blanketing of the wall, which obstructs liquid access despite the presence of adequate bulk liquid elsewhere within the channel. Overall, dryout is a relatively mild form of CHF encountered at low heat fluxes and causes slow escalation of surface temperature. On the other hand, DNB occurs at much higher heat fluxes, resulting in both large and rapid temperature excursions, and posing a higher risk of physical damage to the heated surface. It is therefore the "more dangerous" form of CHF.

Given the importance of CHF to system reliability and safety, this phenomenon has been the subject of intense study dating back to the 1940s. Three primary goals of published studies have been to: (1) investigate the trigger mechanism for CHF, (2) obtain CHF databases for flow configurations of interest, (3) recommend CHF correlations, and, in a few cases, and (4) construct theoretically based models.

Presently, thermal design engineers rely mostly on CHF correlations to set upper heat flux limits for two-phase systems. Unfortunately, most CHF correlations are based on databases for one or a few working fluids and on limited ranges of flow and geometrical parameters, which explains why extrapolation of CHF correlations to other fluids and system parameters often yields inaccurate predictions.

To avoid the limitations of empirical correlations, investigators have sought to construct mechanistic CHF models based on postulated or visually confirmed trigger mechanisms. Illustrated in Fig. 3, four distinct mechanisms have been proposed for development of flow boiling CHF models: *Boundary Layer Separation*, *Bubble Crowding*, *Sublayer Dryout*, and *Interfacial Lift-off*.

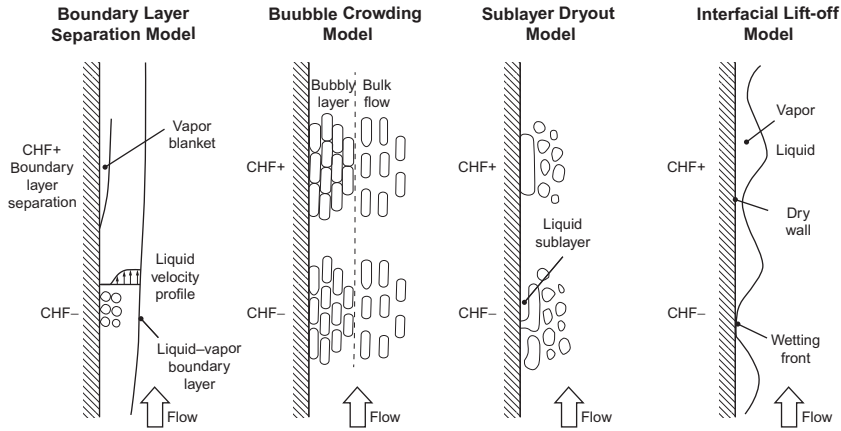

Fig. 3 Trigger mechanisms for flow boiling CHF according to different models.

The Boundary Layer Separation Model [26,27] adopts the analogy between wall liquid injection into a liquid boundary layer and vapor effusion on a heated wall in flow boiling. The premise in the former is that wall injection decreases the liquid velocity gradient adjacent to the wall, and, above an injection velocity threshold, the boundary layer begins to separate from the wall. The Boundary Layer Separation Model is based on the premise that CHF commences when the rate of vapor effusion normal to the heated wall similarly reaches a threshold value, causing appreciable reduction in the bulk liquid velocity gradient and eventually separating the liquid from the wall. Proponents of the Bubble Crowding Model [28,29] propose that CHF occurs when a dense, near-wall layer of oblong bubbles precludes the ability turbulent fluctuations in the bulk liquid to penetrate the vapor layer and replenish the wall. The Sublayer Dryout Model [30] is rooted in the observation that flow boiling CHF is often preceded by formation of oblong bubbles sliding along the heated wall, each trapping a thin liquid sublayer. The main postulate of the model is that CHF will occur when the heat supplied from the wall exceeds the enthalpy of bulk liquid capable of replenishing the sublayer. The Interfacial Lift-off Model [31–34] is based on the observation of a fairly continuous wavy vapor layer forming along the heated wall, which permits liquid access to the wall only in "wetting fronts" corresponding to the wave troughs. The model postulates that CHF is triggered when intense vapor effusion in the wetting fronts causes the interface to lift away from the wall, cutting off any further liquid supply.

Unfortunately, most CHF models are based on observations from vertical upflow and horizontal flow experiments at 1 g_e and unconfirmed for other orientations or for reduced gravity.

2.3 Terrestrial Studies on Influence of Body Force on Flow Boiling

2.3.1 Rationale and Limitations of Simulating Reduced Gravity Boiling by Tilting Heated Wall Relative to Earth Gravity

A rather inexpensive means for investigating the influence of reduced gravity on both pool boiling and flow boiling in terrestrial experiments is to tilt the heated wall relative to Earth gravity. With this arrangement, a partial component of gravity perpendicular to the heated wall is achieved whose magnitude is dependent on the inclination angle. A major drawback of this technique compared to the reduced gravity platforms discussed earlier is the inability to eliminate the component of gravity parallel to the heated wall, which undoubtedly can have a profound influence on fluid motion and therefore both the two-phase heat transfer coefficient and CHF.

Tilting the heated wall relative to Earth gravity in terrestrial studies has been widely used in pool-boiling experiments. And, while this study is focused on flow boiling in reduced gravity, observations from pool-boiling experiments provide valuable insight into the influence of components of gravity both perpendicular and parallel to the heated wall on CHF mechanism and magnitude.

Pool-boiling experiments of this type by Class *et al.* [35], Githinji and Sabersky [36], Marcus and Dropkin [37], Chen [38], Nishikawa *et al.* [39], and Kumar *et al.* [40] have shown profound differences in the CHF mechanism and magnitude for different wall orientations. In most cases, the popular model for pool-boiling CHF by Zuber *et al.* [41] has been validated only for horizontal or near-horizontal upward-facing wall orientations.

Relying on extensive photographic analysis of interfacial behavior, Mudawar *et al.* [42] and Howard and Mudawar [43] showed that wall orientations can be divided into three regions that yield drastically different CHF behavior. As depicted in Fig. 4, the first is near-horizontal upward-facing wall orientations, where buoyancy forces remove the vapor vertically off the heated wall and CHF is accurately predicted by the Zuber *et al.* model. The second region encompasses near-vertical wall orientations, where a wavy vapor layer is observed propagating along the wall while allowing liquid replenishment only in the wave troughs, precisely as predicted by the Interfacial Lift-off Model for flow boiling CHF and depicted in Fig. 3.

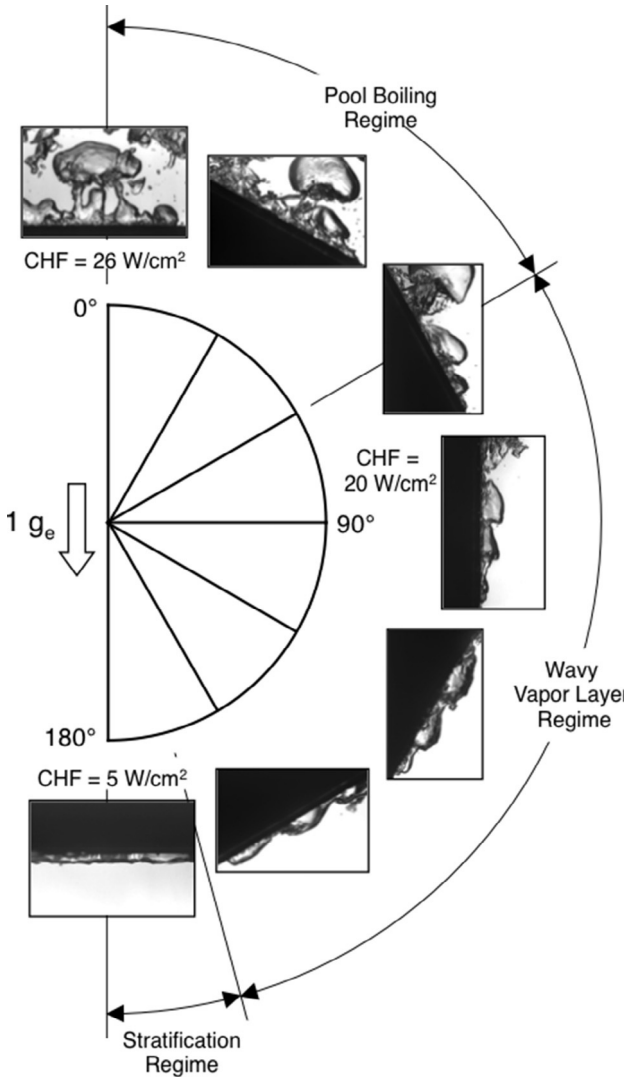

Fig. 4 CHF regimes for saturated pool boiling of PF-5052 on a 1.27×1.27 cm^2 heated wall at different orientations. *Adapted from A.H. Howard, I. Mudawar, Orientation effects on pool boiling CHF and modeling of CHF for near-vertical surfaces, Int. J. Heat Mass Transfer 42 (1999) 1665–1688.*

The third region includes downward-facing wall orientations, which stratify the vapor against the heated wall. Notice in Fig. 4 the reduction in CHF as the heated wall is tilted from the near-horizontal region to the near-vertical region and, most noticeably, the appreciable reduction for downward-facing orientations.

2.3.2 Terrestrial Studies on the Influence of Flow Orientation on Flow Boiling and CHF

Terrestrial studies addressing the influence of flow orientation on flow boiling and CHF point to orientation effects far more complex that those for pool boiling because of the added influence of bulk flow velocity. In their study of nitrogen flow boiling, Simoneau and Simon [44] found that high velocities in downflow cause the vapor and liquid to flow concurrently. On the other hand, low velocities for the same downflow orientation cause the vapor to flow in a direction opposite to that of the liquid. Overall, they measured lower CHF values for downflow compared to upflow, but these differences decreased with increasing velocity, a trend they attributed to gradual weakening of buoyancy effects relative to liquid inertia. Mishima and Nishihara [45] proposed that CHF in low velocity water downflow is caused by flooding. By increasing velocity from the flooded state, bubbles were observed to stagnate in the flow channel as the liquid drag force exerted on the vapor bubbles just balanced buoyancy force; this bubble stagnation condition culminated in CHF values even lower that those associated with flooding at lower velocities. Like Simoneau and Simon, they showed that increasing flow velocity causes the liquid and vapor to flow concurrently in downflow, as well as increase CHF. Gersey and Mudawar [46,47] also demonstrated high sensitivity of CHF for FC-72 to orientation at low velocities, and a gradual decrease in sensitivity with increasing velocity and/or subcooling.

Zhang *et al.* [48–50] performed a series of studies to investigate the influence of orientation and flow velocity for FC-72 in a 5.0×2.5 mm^2 rectangular channel that was heated along one of the two 2.5-mm walls. As shown in Fig. 5A and B, experiments were performed at different orientations in 45° increments, where $\theta = 0°$ and 180° correspond, respectively, to horizontal flow with the heated wall facing upward and downward, while $\theta = 90°$ corresponds to vertical upflow and $\theta = 270°$ to vertical downflow. Fig. 5A shows interfacial behavior just preceding CHF for near-saturated flow ($\Delta T_{sub,out} = 3°C$) at a very low velocity of $U = 0.1$ m/s. Because of weak liquid drag forces at this velocity, buoyancy had a profound influence on CHF in both mechanism and magnitude. Depicted in the same figure are four drastically different CHF regimes: (i) *Pool-Boiling Regime* for $\theta = 0°$, (ii) *Wavy Vapor Layer Regime* for $\theta = 90°$, (iii) *Stratified Regime* for $\theta = 180°$, and (iv) *Vapor Stagnation Regime* for $\theta = 270°$. Because of low flow velocity, the first three CHF regimes are very similar to those observed in pool-boiling experiments by Howard and Mudawar [42], Fig. 4, for similar wall orientations. The Pool Boiling Regime ($\theta = 0°$) is characterized by

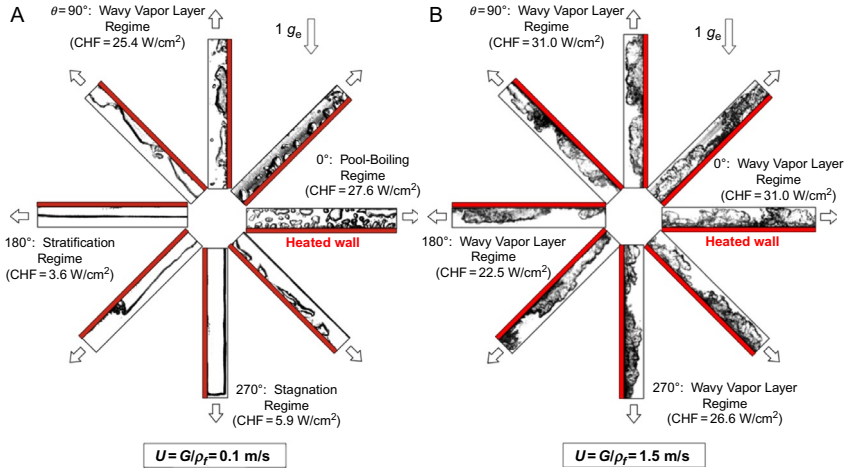

Fig. 5 Near saturated ($\Delta T_{sub,o}=3°C$) flow boiling CHF regimes for FC-72 at 1 g_e corresponding to different flow orientations for inlet liquid velocities of (A) $U=G/\rho_f=0.1$ m/s and (B) $U=G/\rho_f=1.5$ m/s. CHF regime and magnitude are highly dependent on orientation for the lower velocity and fairly independent of orientation for the higher velocity [48].

bubbles coalescing along the heated wall before being detached by buoyancy into the liquid core, but with weak tendency to flow along with the liquid. The Wavy Vapor Layer Regime ($\theta=90°$) is associated with bubble coalescence into a wavy vapor layer propagating along the wall while permitting liquid replenishment only within the wave troughs. The Stratification Regime ($\theta=180°$) is characterized by virtually complete stratification of vapor along the heated wall above the liquid. The Vapor Stagnation Regime ($\theta=270°$) is similar to that reported earlier by Mishima and Nishihara [45] and Gersey and Mudawar [46,47], with the buoyancy force just balancing the liquid drag force. Two other CHF regimes that were observed at $\theta=270°$ at low flow velocities but not shown in Fig. 5A are the *Separated Concurrent Vapor Flow Regime*, encountered at velocities slightly greater than $U=0.1$ m/s, where liquid drag exceeded buoyancy, and a *Vapor Counter Flow Regime*, detected at velocities below 0.1 m/s, where buoyancy exceeded liquid drag, causing the vapor to flow backwards. Notice in Fig. 5A the large differences in CHF magnitude among the different orientations at this low velocity.

In contrast, Fig. 5B shows interfacial behavior for near-saturated flow ($\Delta T_{sub,out}=3°C$) at a relatively high velocity of $U=1.5$ m/s. With the large

increase in liquid inertia and drag forces, buoyancy effects are much weaker for this case, evidenced by all orientations featuring the same Wavy Vapor Layer Regime and much closer CHF values.

Complementing the flow orientation studies of Zhang *et al.* [48–50], Kharangate *et al.* [51,52] recently published a comprehensive investigation of orientation effects on flow boiling CHF for FC-72 in a rectangular channel heated along one wall or two opposite walls corresponding to saturated two-phase inlet conditions. Experiments were performed in vertical upflow, vertical downflow, and horizontal flow, subject to variations in mass velocity, inlet quality, and wall heat flux. For horizontal flow, the effects of gravity were reflected in appreciable stratification across the channel at low mass velocities, and buoyancy aiding vapor removal from, and liquid replenishment of the bottom heated wall, while accumulating vapor along the top heated wall. The heat transfer coefficient showed significant variations among the different orientations at low mass velocities, but became insensitive to orientation above $G \sim 800$ kg/m^{2}s. Similarly, for both single-sided and double-sided heating, the influence of orientation on CHF decreased with increasing mass velocity, and fairly identical CHF values were achieved at high mass velocities irrespective of orientation. Further, increasing inlet quality served to decrease the mass velocity required for inertia to negate gravity effects.

2.3.3 Criteria for Negating Body Force Effects Based on Terrestrial Experiments Involving Different Flow Orientations

Determining the minimum flow rate or flow velocity that would negate the influence of body force on flow boiling CHF is crucial for development of thermal control devices in future space vehicles. While the aforementioned trends prove that high velocities produce the high liquid inertia and drag forces essential to overcoming gravity effects, using high velocities in space systems causes high-pressure drops and therefore requires appreciable pumping power. It is therefore an important design goal in negating the influence of gravity to derive criteria for the *minimum* velocity required to achieve this goal.

Zhang *et al.* [53] developed such criteria for flow boiling with $x_{e,in} \leq 0$. They proposed three criteria that must be satisfied simultaneously to negate any gravity effects: (i) negating the influence of gravity component perpendicular to the heated wall, (ii) negating the influence of gravity component opposite to the flow direction, and (iii) ensuring that the wavelength

associated with instability of the liquid–vapor interface is smaller than the length of the heated wall to facilitate liquid contact with wall.

The criterion governing influence of the gravity component perpendicular to the heated wall is based on the observation that the Wavy-Vapor Layer Regime is dominant for all orientations excepting very low velocities. The wavy layer can be described with the aid of classical instability theory and the assumption of sinusoidal vapor–liquid interface. The critical wavelength, λ_c, of the wavy interface is given by

$$\frac{2\pi}{\lambda_c}\frac{\sigma\left(\rho_f+\rho_g\right)}{\rho_f\rho_g\left(U_g-U_f\right)^2}=\frac{1}{2}\left\{1+\sqrt{1+4\frac{\left(\rho_f-\rho_g\right)\left(\rho_f+\rho_g\right)^2\sigma g_e\cos\theta}{{\rho_f}^2{\rho_g}^2\left(U_g-U_f\right)^4}}\right\}. \quad (1)$$

where U_g and U_f are mean velocities of the vapor and liquid layers, respectively, and $g_e\cos\theta$ is the component of gravity perpendicular to the heated wall. Eq. (1) shows that interfacial instability is governed by the relative magnitudes of three components: inertia, surface tension, and component of gravity perpendicular to the heated wall. The influence of gravity is negligible when

$$\left|\frac{\left(\rho_f-\rho_g\right)\left(\rho_f+\rho_g\right)^2\sigma g_e\cos\theta}{\rho_f^2\rho_g^2\left(U_g-U_f\right)^4}\right|\ll\frac{1}{4}, \quad (2)$$

which simplifies Eq. (1) to

$$\lambda_c=\frac{2\pi\sigma\left(\rho_f+\rho_g\right)}{\rho_f\rho_g\left(U_g-U_f\right)^2}. \quad (3)$$

Eq. (3) can also be presented in terms of the Bond and Weber numbers,

$$\left|\frac{Bo}{We^2}\right|=\left|\frac{\left(\rho_f-\rho_g\right)\left(\rho_f+\rho_g\right)^2\sigma g_e\cos\theta}{\rho_f^2\rho_g^2\left(U_g-U_f\right)^4}\right|\ll\frac{1}{4}, \quad (4)$$

where

$$Bo=\frac{\left(\rho_f-\rho_g\right)g_e\cos\theta L^2}{\sigma} \quad (5)$$

and

$$We = \frac{\rho_f \rho_g \left(U_g - U_f\right)^2 L}{\left(\rho_f + \rho_g\right)\sigma}. \tag{6}$$

This criterion is derived by substituting the difference between the vapor and liquid velocities by the mean inlet liquid velocity, U, and the gravity component perpendicular to the heated wall by it maximum value, g. The magnitude of Bo/We^2 corresponding to $U = 1.5$ m/s was used in this criterion, since higher velocities yielded little CHF dependence on orientation,

$$\frac{Bo}{We^2} = \frac{\left(\rho_f - \rho_g\right)\left(\rho_f + \rho_g\right)^2 \sigma g}{\rho_f^2 \rho_g^2 U^4} \ll 0.09. \tag{7}$$

The second criterion for negating the influence of gravity parallel to the heated wall and opposite the flow direction relies on an expression for rise velocity of a large coalescent slug flow bubble relative to liquid [54],

$$U_\infty = 0.35 \frac{\left[\left(\rho_f - \rho_g\right) g_e |\sin\theta| D_H\right]^{1/2}}{\rho_f^{1/2}}, \tag{8}$$

where D_H is the flow channel's hydraulic diameter. Notice that when $U_\infty > U$ the vapor would flow backward relative to the liquid and induce flooding, and vapor stagnation occurs when $U_\infty = U$. A sufficient criterion for preventing flooding was derived by setting $U_\infty \ll U$ (to completely eliminate the likelihood of flooding) and $\sin\theta = 1$ (corresponding to strongest orientation influence). Based on the observation by Zhang *et al.* that flooding is avoided for $U \geq 0.5$ m/s, the criterion for negating flooding effects was presented in terms of the Froude number,

$$\frac{1}{Fr} = \frac{\left(\rho_f - \rho_g\right) g D_H}{\rho_f U^2} \leq 0.13. \tag{9}$$

The third criterion is based on the premise that the interfacial wavelength must be smaller than the length of the heated wall, i.e., $\lambda_c \leq L$. Introducing the relation for λ_c from Eq. (3), this criterion can be expressed in terms of the Weber number,

$$We = \frac{\rho_f \rho_g \left(U_g - U_f\right)^2 L}{\left(\rho_f + \rho_g\right)\sigma} \geq 2\pi. \tag{10}$$

Notice that the three minimum velocity criteria for negating gravity influences must be satisfied simultaneously. Fig. 6 illustrates how these criteria can be used to determine the minimum velocity for a given fluid and operating pressure. The relations for the three criteria are plotted together against g/g_e, the ratio of prevailing gravity to Earth gravity. Avoiding any body force effects requires that U exceeds the value predicted by each of the three criteria. Fig. 6 shows that the flooding criterion is dominant only for large gravities with $g/g_e > 75$. Below this gravity value, and spanning Earth, Lunar, and Martian gravities, instability effects associated with the gravity component perpendicular to the wall become dominant. The heater length criterion is dominant only for very low gravities, and the value of g/g_e associated with transition between the instability-dominated and heater-length-dominated regions is a function of L; shorter heaters require higher velocities to ensure $\lambda_c \leq L$.

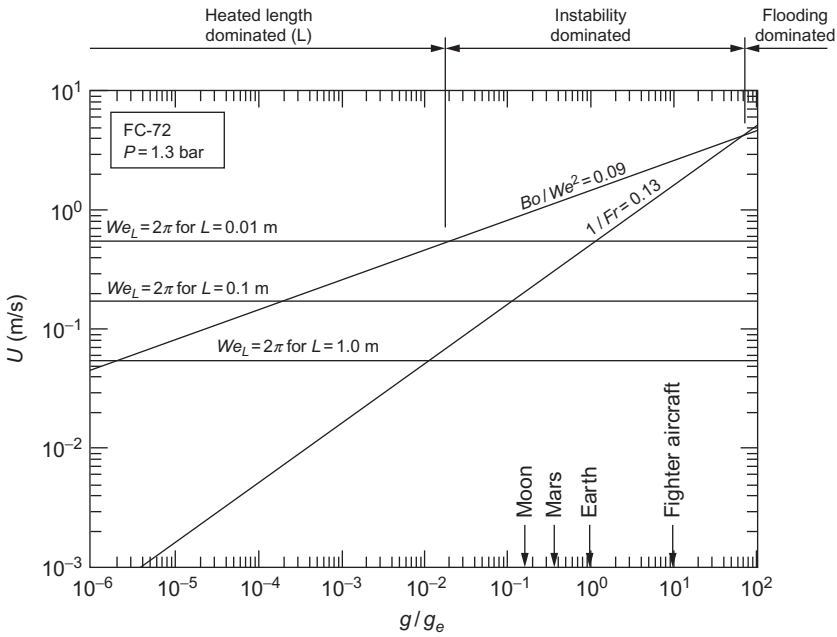

Fig. 6 Determination of minimum flow velocity required to satisfy all criteria for negating gravity effects on flow boiling CHF.

The three criteria just discussed are based on the data of Zhang *et al.* corresponding to $x_{e,in} \leq 0$. In a more recent study, Konishi *et al.* [55] extended the three criteria to two-phase inlet conditions, $x_{e,in} \geq 0$. Since increasing $x_{e,in}$ also increases flow velocities, two-phase inlet conditions strengthen inertial effects, therefore requiring lower inlet velocities to negate gravity effects than predicted by the above criteria.

2.4 Pool Boiling in Reduced Gravity

For decades, studies on boiling in reduced gravity have been focused almost entirely on pool boiling. These studies addressed several fundamental processes such as bubble nucleation, growth, and coalescence in the absence of gravity, and the impact of these processes on both nucleate boiling heat transfer and CHF.

Oka and coworkers performed pool-boiling experiments with *n*-pentane, R-113, and water in parabolic flight [56], and R-113 and water in a drop shaft [57]. In both platforms, surface tension and latent heat of vaporization had a significant impact on bubble nucleation, growth, and coalescence, and therefore on heat transfer performance. At moderate subcoolings, bubbles in low surface tension and low heat of vaporization fluids, *n*-pentane and R-113, rarely detached from the heated wall. At low heat fluxes, initially isolated bubbles slid slowly across the wall and coalesced with neighboring bubbles, and this sliding motion promoted liquid replenishment of wall dryout regions originally occupied by the bubbles. High heat fluxes and near-saturated conditions caused isolated bubbles to grow significantly larger and coalesce with other bubbles with greater frequency, culminating in the formation of a single large bubble covering most of the heated wall. CHF was detected by unsteady rise in wall temperature resulting from dryout under the large bubble. Fig. 7A shows that nucleate boiling heat transfer and CHF for R-113 are both highly compromised in microgravity than in Earth gravity. Oka *et al.* reported distinctly different behavior in microgravity with water, which possesses significantly higher surface tension and heat of vaporization than those for *n*-pentane and R-113. Instead of sliding across the wall, isolated bubbles quickly detached from the wall. At moderate subcoolings, condensation caused the detached bubbles to collapse in the bulk liquid. But at saturated or near-saturated conditions, the detached bubbles remained in the vicinity of the heated wall, where they coalesced with one another into a single large vapor bubble that grew further in size by capturing newly formed bubbles. A key advantage of the high latent heat of

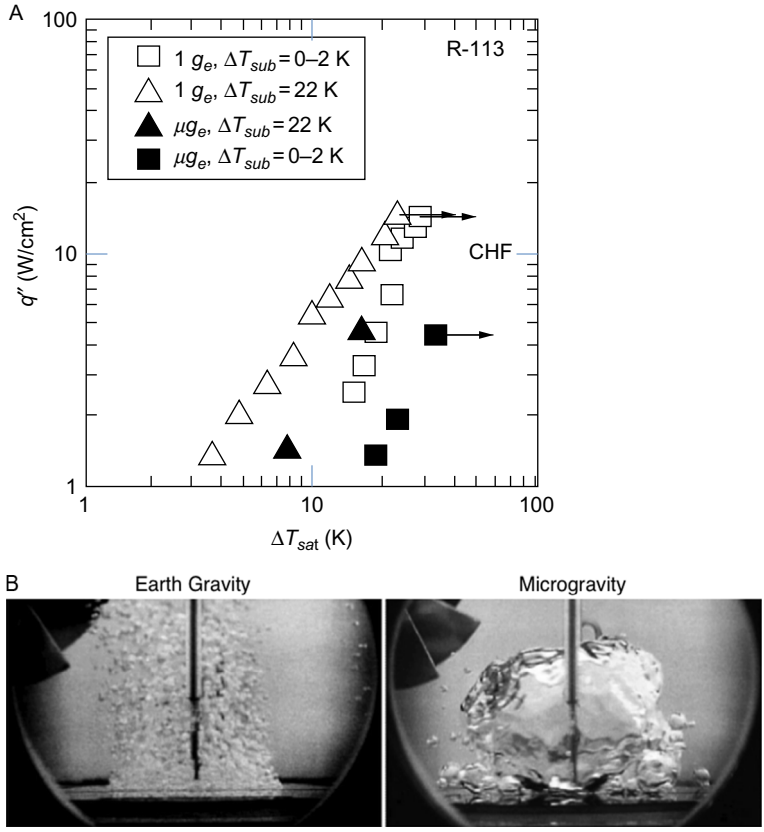

Fig. 7 (A) Pool-boiling curves for R-113 in microgravity and Earth gravity at two levels of subcooling [57]. (B) Photos of pool boiling of R-113 in Earth gravity and microgravity (courtesy NASA). *Adapted from C. Konishi, I. Mudawar, Review of flow boiling and critical heat flux in microgravity, Int. J. Heat Mass Transfer 80 (2015) 469–493.*

vaporization of water was delayed evaporation of the thin liquid film beneath the large bubble, evidenced by formation of a secondary bubble within the large bubble and absence of wall temperature excursions.

While thermocapillary (or Marangoni) convection is dwarfed by buoyancy in terrestrial conditions, this phenomenon has been reported to have a significant impact on bubble dynamics in microgravity. This convection effect is induced by surface tension gradients causing fluid motion along the vapor–liquid interface and away from the heated wall and is manifest by formation of jet streams around nucleating bubbles. Straub [58] confirmed these effects in microgravity pool-boiling experiments conducted in Spacelab mission IML-2 using R-11 as working fluid on a hemispherical

heater. In a follow-up study [59], he reported an increase in the strength of thermocapillary jets with increasing heat flux that showed nonmonotonic dependence on subcooling. The jet velocity was zero for saturated conditions and increased appreciably in response to a slight increase in subcooling. But after reaching maximum value, jet velocity decreased back to zero at high subcooling. In general, observation of a large bubble engulfing the heated wall in microgravity has been attributed to unusually large values of *Capillary* (or *Laplace*) *Length*, which governs the bubble size for a given combination of surface tension and gravity.

Merte [60,61] conducted a series of microgravity pool-boiling experiments with R-113 onboard NASA's Space Shuttles. Their tests encompassed subcoolings of $\Delta T_{sub} = 0.3$–22.2K and heat fluxes of $q'' = 0.5$–8 W/cm^2. For moderate subcoolings and low heat fluxes, a large vapor bubble formed and was observed to hover in the vicinity of the heated wall with smaller bubbles nucleating underneath. Excepting the highest subcooling condition, the highest heat flux caused the large bubble to engulf the entire heated wall, with the ensuing partial or complete dryout leading to unsteady rise in the wall temperature. Fig. 7B contrasts the bubble behavior captured by Merte in Earth gravity compared to that in microgravity, with the former yielding many small discrete bubbles that are pulled away from the wall by buoyancy, compared to a single large bubble in microgravity engulfing the entire heated wall.

Kim and coworkers conducted a series of microgravity pool-boiling experiments in both parabolic flight and onboard the ISS. They developed a unique heater surface comprised of several arrays of platinum resistance heaters that were controlled by a bank of feedback circuitry to maintain constant surface temperature, while allowing high-speed video imaging from behind the surface. Their KC-135 parabolic flight experiments employed FC-72 and three different heater sizes, 0.65, 2.62, and 7.29 mm^2 [62,63]. In microgravity, surface tension had a profound influence on bubble dynamics, and, like prior investigators, they reported the formation of a single large bubble regardless of heater size. On the other hand, heater size had a noticeable influence on bubble dynamics in hyper-G (1.7 g_e) depending the magnitude of capillary length. With a size close to the capillary length, the smallest heater produced a single primary bubble, while the largest heater produced a primary bubble surrounded by multiple satellite bubbles. Kim's team also performed long-duration microgravity tests onboard the ISS using *n*PFH as working fluid [64]. These experiments culminated in a series of observations concerning pool boiling in microgravity. The onset of nucleate

boiling (ONB) occurred at lower wall superheat in microgravity compared to Earth gravity, and increasing the system pressure decreases the superheat at ONB. Overall, heat transfer was enhanced with increased subcooling and degraded with decreased subcooling; the latter led to the formation of a large bubble that engulfed the entire heater surface. And, with decreasing heater size, nucleate boiling heat transfer was enhanced at high subcooling and degraded at low subcooling.

Dhir and coworkers [65] also conducted nucleate boiling experiments onboard the ISS with *n*PFH using an aluminum wafer equipped with an array of strain gauge heaters and thermistors, and containing five 10-μm diameter artificial cavities. Like previous investigators, they observed the formation of a large primary bubble on the heater surface from lateral merging of small bubbles. At high superheats, the large bubble lifted away from, but hovered in the vicinity of the surface, growing in size by capturing additional smaller bubbles generated on the surface. They compared single and multiple bubble dynamics and heat transfer data with predictions based on numerical simulation tools developed earlier by Son *et al.* [66]. For single-bubble nucleation, they were able to predict bubble shape and size with remarkable accuracy.

Overall, the vast majority of microgravity boiling research conducted to date has been focused on pool boiling. The stated intent of pool-boiling studies has been to develop fundamental mechanistic understanding of the influence of microgravity on boiling dynamics (incipience, nucleation, growth, and coalescence), nucleate boiling heat transfer, and CHF. Most of these studies clearly point to the highly problematic formation of an unusually large bubble in the absence of an effective means to remove this bubble from the heated wall. This phenomenon is also largely responsible for unusually low CHF values. These complications provide ample evidence against the viability of pool boiling for thermal management in space systems and explain the recent urgent calls to shift the focus of microgravity phase change research from pool boiling to flow boiling [3,5]. To compensate for the absence of body force, flow boiling is highly effective at utilizing bulk liquid motion to flush vapor bubbles away from and promote liquid replenishment of the wall, thereby enhancing both nucleate boiling heat transfer and CHF. Despite these well-established merits, very few microgravity flow boiling experiments have been performed to date. Two main reasons for the lack of flow boiling studies are high complexity (many flow components, far more extensive instrumentation, larger size, and high-power requirements) and much higher cost compared to pool-boiling experiments.

2.5 Adiabatic Two-Phase Flow in Microgravity

For several decades, researchers have been aware of appreciable differences in adiabatic two-phase behavior between terrestrial and reduced gravity environments. According to Zhao and Rezkallah [67] and depicted in Fig. 8A, only three of the classical two-phase flow patterns are achieved in reduced gravity: bubbly, slug, and annular, with another frothy slug-annular pattern observed less frequently, depending on combinations of superficial velocities of vapor and liquid, j_g and j_f, respectively.

Choi *et al.* [68] compared two-phase flow patterns for air–water in a 10-mm diameter tube in microgravity (μg_e), hypergravity (2 g_e), and Earth gravity (1 g_e). They reported strong differences in flow behavior between low and high velocities. As shown in Fig. 8B, low velocities produced bubbly flow in μg_e, whereas 1 g_e and 2 g_e produced stratified and plug flows, respectively. However, high velocities enabled flow inertia to overcome the effects of both surface tension and body force, evidenced by similar flow patterns for all three gravity levels.

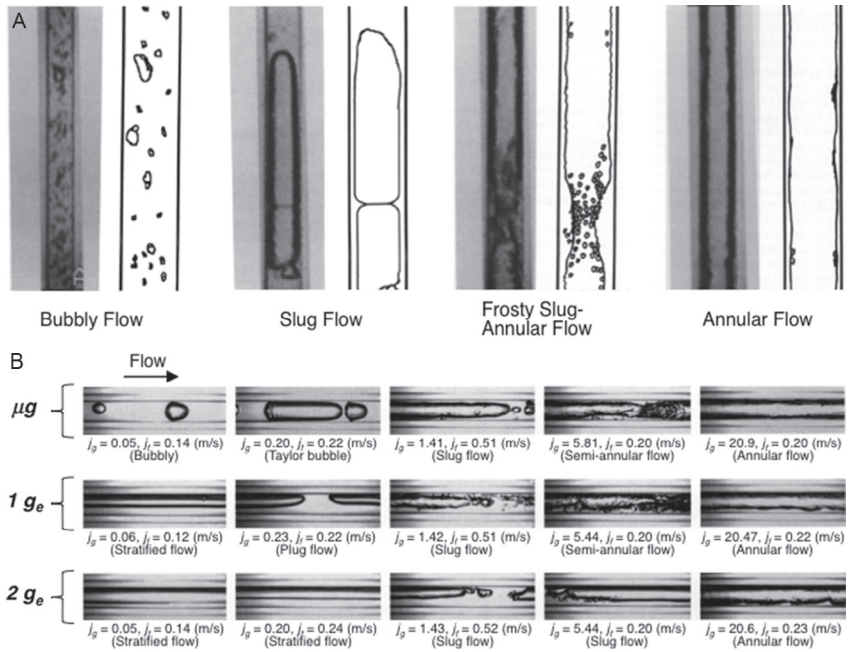

Fig. 8 (A) Air–water two-phase flow patterns in microgravity [67]. (B) Air–water flow patterns along a 10-mm diameter tube in microgravity (μg_e), terrestrial gravity (1 g_e), and hypergravity (2 g_e) [68]. *Adapted from C. Konishi, I. Mudawar, Review of flow boiling and critical heat flux in microgravity, Int. J. Heat Mass Transfer 80 (2015) 469–493.*

Dukler *et al.* [69] performed adiabatic air–water flow parabolic flight and drop tower experiments using a 9.52-mm diameter, 0.475-m long horizontal tube. They observed three of the classical flow patterns: bubbly, slug, and annular, and derived Drift-Flux relations for transitions between patterns based on superficial velocities and void fraction averaged over the cross-sectional area of the tube. Bousman *et al.* [70–72] extended the work of Dukler *et al.* by conducting adiabatic parabolic flight experiments using horizontal tubes having two different diameters, 12.7 and 25.4 mm. They also explored the effects of surface tension by using three different fluid mixtures: air–water, air-50–50 wt% water/glycerin, and air–water/Zonyl FSP. They reported turbulent oscillations were more pronounced and promoted bubble coalescence in the larger tube, which caused a significant shift in the void fraction corresponding to bubbly–slug transition, and recommended different relations for bubbly–slug transition corresponding to the different fluid combinations. They also used the formulation proposed by Dukler *et al.* to derive an alternative Drift-Flux relation for slug–annular transition.

Colin *et al.* [73] compared flow patterns for adiabatic air–water flow in a 40-mm diameter, 3.14-m long tube in parabolic flight with those in vertical upflow in Earth gravity. By comparing results with those of Dukler *et al.* [69] and Bousman *et al.* [72], they showed a dependence of flow-pattern transitions on tube diameter. For example, in microgravity, bubbles in the 40-mm tube were concentrated more toward the central region of the tube, while they were more uniformly distributed in the smaller tubes of Dukler *et al.* and Bousman *et al.* This behavior was attributed to increased bubble coalescence in the larger tube due to increased turbulence. Later, Colin *et al.* [74] proposed alternative relations for flow-pattern transitions that accounted, in addition to superficial velocities and void fraction, for the influence of tube diameter and fluid properties.

Lee [75,76] also developed flow-pattern transition models, which were originally intended for flow condensation in microgravity but later adopted by several investigators in conjunction with adiabatic two-phase flow. These transition relations were derived by examining dominant forces for each flow pattern, including surface tension, gravity, inertia, and friction, in addition to turbulent fluctuations.

Reinarts [77] conducted two-phase flow experiments with R-12 in two horizontal tubes having 4.7 and 10.5 mm diameters in parabolic flight to simulate microgravity as well as Lunar and Martian gravities and compared the flight data with those in Earth gravity. While only bubbly, slug, and annular patterns were observed in microgravity, body force effects in Lunar

and Martian gravities were also reflected in the form of stratified and plug flow patterns.

Another key focus of adiabatic microgravity studies is two-phase pressure drop. The total pressure drop in two-phase flow is comprised of frictional, accelerational, and gravitational components. With zero accelerational and gravitational components in adiabatic flow and in microgravity, respectively, adiabatic two-phase flow experiments in microgravity are intended for measurement of the frictional component alone.

Colin *et al.* [73] showed that, because of concentration of bubbles along the center of large diameter tubes, with almost pure liquid flowing near the wall, microgravity wall friction data agreed well with predictions of the Blasius correlation for single-phase turbulent flow. On the other hand, Colin *et al.* [74,78] reported an increase in wall friction for lower Reynolds number flows in small tubes compared to predictions of single-phase relations, which they attributed to closer proximity of bubbles to the wall. A similar trend was also reported by Zhao and Rezkallah [79].

Bousman [70] found that neither the Homogeneous Equilibrium Model nor the Separated Flow Model could accurately predict their microgravity pressure drop data corresponding to bubbly and slug flows. However, fairly good predictions of annular flow data were achieved using the Lockhart–Martinelli correlation [80].

Both Chen *et al.* [81] and Choi *et al.* [68] reported significantly higher pressure drops in microgravity compared to Earth gravity, and Zhao *et al.* [82] showed that 1-g_e empirical correlations generally yield poor predictions of microgravity pressure drop data. The fundamental differences in two-phase behavior between microgravity and Earth gravity, and failure of Earth gravity correlations meant new or modified correlations must be developed specifically to microgravity.

2.6 Two-Phase Flow Boiling Patterns and Transitions in Microgravity

Very few microgravity flow boiling studies have been undertaken since the pioneering works of Siegel and Usiskin [83] in the late 1950s. Misawa [84] performed both drop tower and parabolic flight experiments using R-113. They employed a film heated square channel having a cross-sectional area of 5×5 mm^2 and 500-mm heated length, and two electrically coiled tubes of similar length with diameters of 4.0 and 12.8 mm. They reported earlier flow-pattern transitions in microgravity compared to 1 g_e, but differences diminished with increasing inlet vapor quality. They captured bubbly, slug,

slug–frothy, annular, and annular–frothy patterns and showed that pattern transitions were well predicted by the microgravity adiabatic two-phase pattern maps of Dukler *et al.* [69] and Colin *et al.* [73].

Saito *et al.* [85] performed parabolic flight water flow boiling experiments in a 25×25 mm^2 and 600-mm long square channel that was fitted along its axis with an electrically heated 8-mm diameter and 200-mm long rod. Fig. 9A shows strong body force effects at 1 g_e and low flow rates, which are reflected by bubbles generated on the heated rod detaching and stratifying in the upper region of the flow channel. On the other hand, absence of buoyancy in microgravity is reflected by better symmetry about the axis and bubbles propagating along the heated wall and growing axially by coalescence and capture of bubbles generated downstream.

Ohta *et al.* [86] conducted parabolic flight flow boiling experiments with R-113 using 8-mm diameter pyrex tubes with heated lengths of 70 and 255 mm. Experimental data for subcooled and saturated inlet conditions were obtained in microgravity and in 2 g_e and compared to those in 1 g_e vertical upflow. As shown in Fig. 9B, they observed bubbly flow in all gravities for subcooled inlet conditions and a relatively low mass velocity of $G = 150$ kg/m^{2}s, with bubbles in microgravity being significantly larger than in 1 g_e or 2 g_e. However, their highest mass velocity of $G = 600$ kg/m^{2}s produced similar interfacial behavior and equal bubble detachment diameters for all gravities. This similarity was attributed to increased inertia negating any body force effects. Fig. 9B shows that body force effects were also suppressed at high inlet quality and higher heat flux, evidenced by similar annular flow behavior for all gravity levels.

Luciani *et al.* [87,88] performed parabolic flight subcooled flow boiling experiments with HFE-7100 in three narrow rectangular channels with flow areas of 6.0×0.254, 6.0×0.454, and 6.0×0.654 mm^2, and equal heated length of 50 mm. Data were measured in microgravity and 1.8 g_e and compared with those for vertical upflow in 1 g_e. They reported upstream heat transfer enhancement in microgravity, but similar interfacial behavior in 1 g_e and 1.8 g_e.

2.7 Two-Phase Heat Transfer and Pressure Drop in Microgravity

Misawa [84] reported that turbulent activity in flow boiling within the bubbly regime is reduced in microgravity, which leads to deterioration in the two-phase heat transfer coefficient in microgravity compared to Earth gravity.

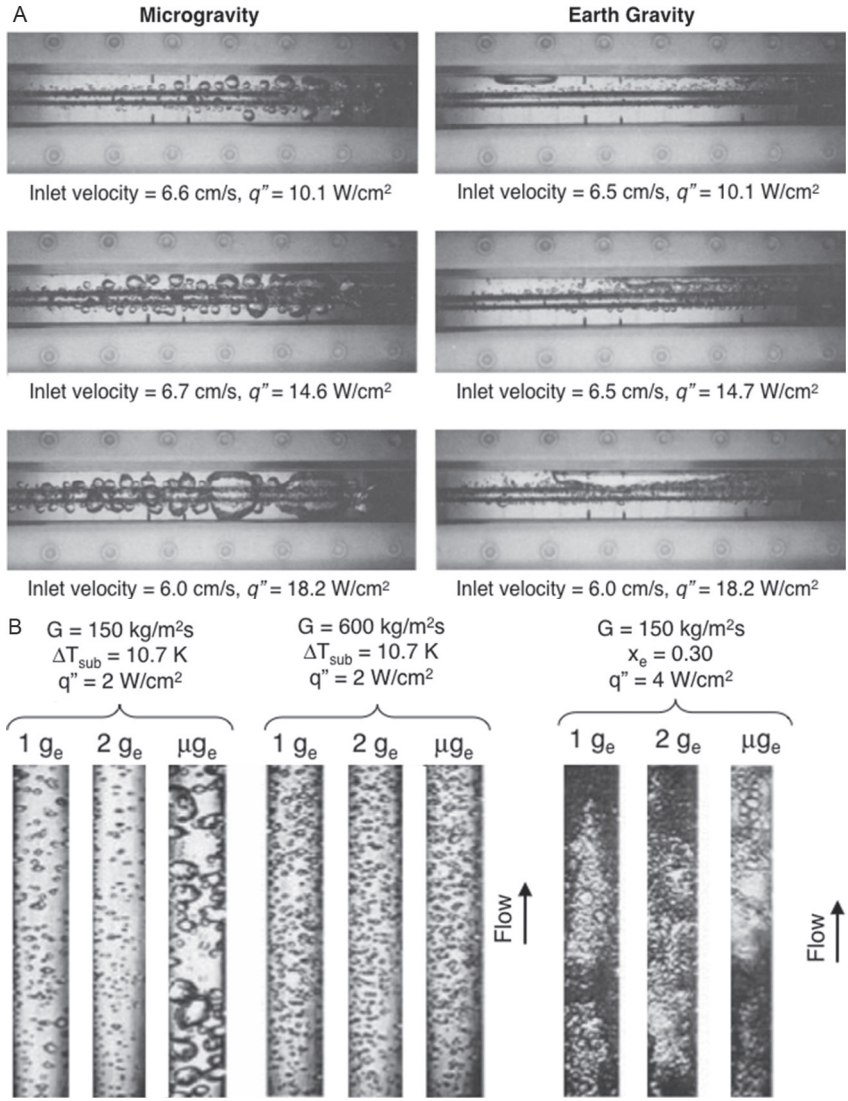

Fig. 9 (A) Comparison of water flow boiling behavior in microgravity and Earth gravity along a square channel fitted with a central cylindrical heating rod [85]. (B) Comparison of flow boiling of R-113 in vertical upflow in 1 g_e, 2 g_e, and μg_e for subcooled inlet conditions at low and high mass velocities, and for low mass velocity and high inlet quality [86]. *Adapted from C. Konishi, I. Mudawar, Review of flow boiling and critical heat flux in microgravity, Int. J. Heat Mass Transfer 80 (2015) 469–493.*

Ohta *et al.* [86] performed parabolic flight experiments to simulate flow boiling in microgravity and in 2 g_e and compared results to those for vertical upflow in Earth gravity. In the bubbly flow regime, transitioning from microgravity to hypergravity during a flight parabola had minimal influence on heat transfer. They suggested that the absence of gravity effects is the result of a bubbly flow regime dominated by a nucleate boiling heat transfer mechanism that is both local and confined to the heated wall. However, the annular flow regime, corresponding to moderate inlet qualities, showed behavior dominated by two-phase forced convection that was strongly gravity dependent, with heat transfer clearly compromised in low compared to high gravity. The influence of gravity in the annular regime was manifest in several ways, depending on heat flux and inlet quality. First, waves in the annular liquid film caused film thickness to decrease in high vs low gravity. And, despite the dominance of forced convection for most operating conditions, high heat fluxes triggered nucleate boiling within the annular liquid film, which helped maintain similar heat transfer coefficients during the varying gravity event. The influence of gravity in the annular regime also decreased at high inlet quality as high vapor core velocity increased the shear force exerted upon the annular film's interface, dwarfing gravity effects.

Celeta *et al.* [89] and Baltis *et al.* [90] explored wall temperature fluctuations in a 6.0-mm tube in response to gravity variations during parabolic maneuvers. At low mass velocities and low exit vapor qualities, hypergravity produced bubbly flow with small bubbles detaching from the wall. Within the microgravity period of the parabola, heat transfer was enhanced significantly in the inlet and compromised in the outlet. The upstream enhancement was attributed to larger bubbles in microgravity intensifying mixing and turbulence. The influence of gravity on heat transfer was weakened with increasing mass velocity. Heat transfer in the intermittent/annular pattern at low mass velocity and high exit quality showed slight dependence on gravity.

Luciani *et al.* [87,88] reported up to 30% heat transfer enhancement in microgravity compared to Earth gravity. For all gravities, large heat transfer coefficients were measured near the inlet, but dropped sharply to fairly constant values from about the channel's middle to the exit. Later, Brutin *et al.* [91] examined the influence of gravity on void fraction and two-phase frictional pressure drop. Increasing gravity was observed to increase the fraction of cross-sectional area occupied by liquid, which, in turn, increased the frictional pressure drop.

Overall, these findings prove that the influence of body force on two-phase heat transfer is highly dependent on mass velocity, inlet quality, and heat flux, as these parameters also dictate which flow pattern is dominant for a given gravity.

2.8 Flow Boiling CHF in Microgravity

2.8.1 CHF for Subcooled Inlet Conditions

As discussed earlier, flow boiling CHF is arguably the most important design and safety parameter for heat-flux-controlled thermal control systems. This concern is heightened by previous microgravity pool-boiling studies, which demonstrated appreciable decline in CHF in microgravity compared to Earth gravity. As discussed earlier, this decline is attributed to formation of an unusually large bubble in microgravity that engulfs the entire heated wall, in the absence of an effective body force to remove smaller bubbles before they have the opportunity to coalesce into a single large bubble.

Flow boiling provides an effective means to compensate for the lack of body force in two-phase space systems by relying on bulk liquid motion to flush bubbles away from the wall and preclude the formation of a massive vapor bubble. Yet, despite this crucial benefit, very few studies have been devoted exclusively to flow boiling CHF in microgravity.

Ma and Chung [92] investigated subcooled flow boiling of FC-72 across a heated 0.254-mm platinum wire in a 2.1-s drop tower. Their data showed a significant reduction in CHF in microgravity compared to Earth gravity, but differences in both heat transfer rate and CHF decreased with increasing flow rate.

In a study that paved the way for the joint Purdue-NASA FBCE for the ISS, Zhang *et al.* [93] conducted a series of parabolic flight subcooled flow boiling CHF experiments using FC-72 as working fluid. Using the flight rig depicted in Fig. 10A, these experiments yielded CHF data for microgravity, Lunar gravity ($0.17\ g_e$), and Martian gravity ($0.38\ g_e$), which were later compared with CHF data measured in Earth gravity. Their study featured a mostly transparent rectangular flow channel having a $2.5 \times 5.0\ \text{mm}^2$ cross section, Fig. 10B, that was heated along one of its two 2.5-mm sides with a 101.6-mm long copper plate by a series of thick film resistors as shown in Fig. 10C. Fig. 11 shows, for $U = G/\rho_f = 0.15$ m/s and $\Delta T_{sub,out} = 3.0°\text{C}$, variations of boiling data and corresponding interfacial behavior with increasing heat flux in microgravity. In the absence of buoyancy

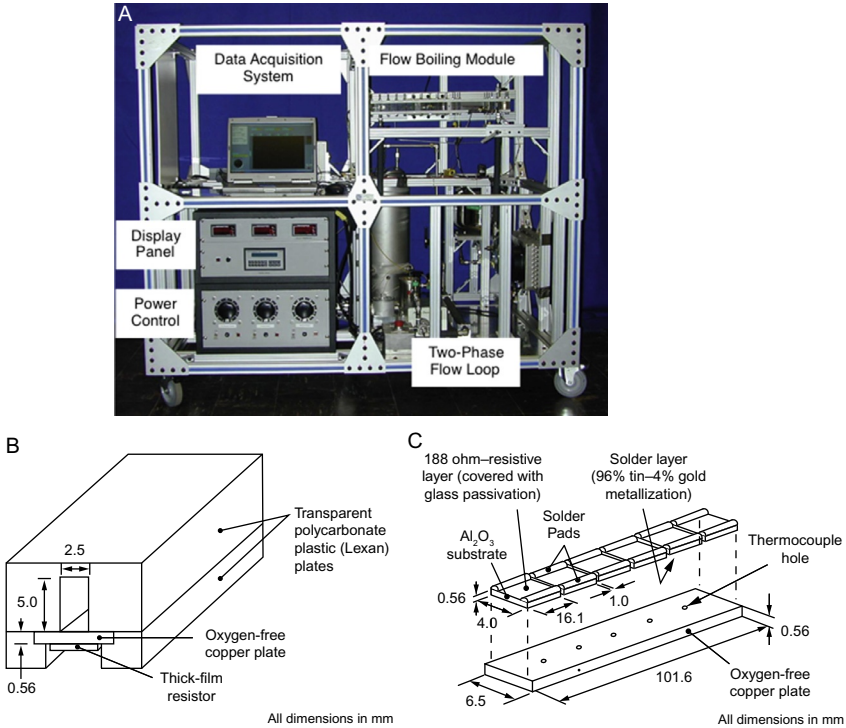

Fig. 10 (A) Photo of test rig, and schematics of (B) flow channel assembly, and (C) heated wall construction for parabolic flight flow boiling apparatus.

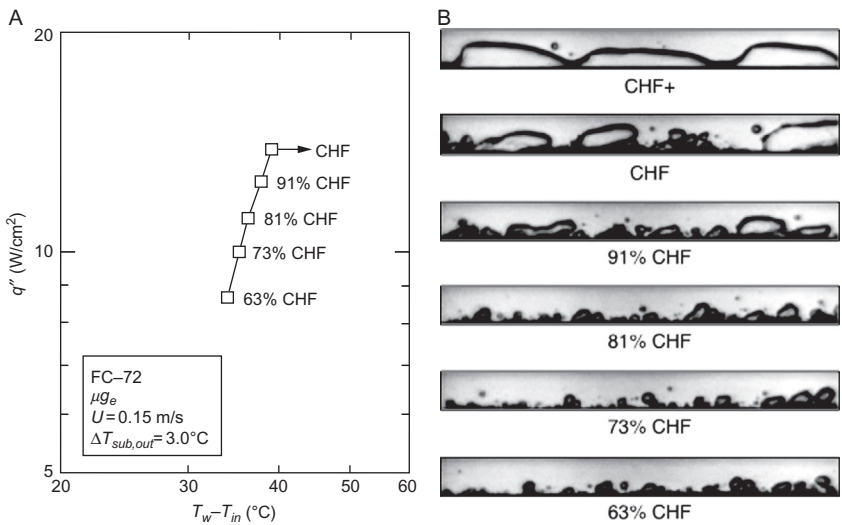

Fig. 11 (A) Boiling curve and (B) interfacial behavior at different heat fluxes in microgravity for $U = 0.15$ m/s and $\Delta T_{sub,out} = 3.0$°C. *Adapted from H. Zhang, I. Mudawar, M.M. Hasan, Flow boiling CHF in microgravity, Int. J. Heat Mass Transfer 48 (2005) 3107–3118.*

perpendicular to the heated wall, vapor masses are shown simply sliding along the wall with no tendency to depart to the bulk flow region. At 63% and 73% of CHF, small bubbles can be seen coalescing along the wall into larger bubbles, and, at 81% of CHF, the size of the coalescent bubbles increasing considerably. At 91% of CHF, most of the vapor amasses into long vapor patches that propagate along the heated wall. Just prior to CHF, the patches increase appreciably in size and begin to mimic a wavy vapor layer, confining liquid access to small troughs—wetting fronts—between the vapor patches. Eventually, the liquid–vapor interface begins to separate from the wall by intense momentum of vapor generated in the troughs. To better identify the trigger mechanism for CHF in microgravity, the interfacial behavior was also recorded during the CHF transient. Fig. 12A shows sequential video images captured just before, during, and just after CHF for a low velocity of $U = G/\rho_f = 0.15$ m/s and $\Delta T_{sub,out} = 3.0°C$. At CHF−, a series of long vapor patches are shown propagating along the wall, and most of the heat appears to be released to liquid in the wetting fronts between the vapor patches. At CHF, the initially discrete vapor patches merge together to form a fairly continuous vapor layer. Notice in the middle images captured at

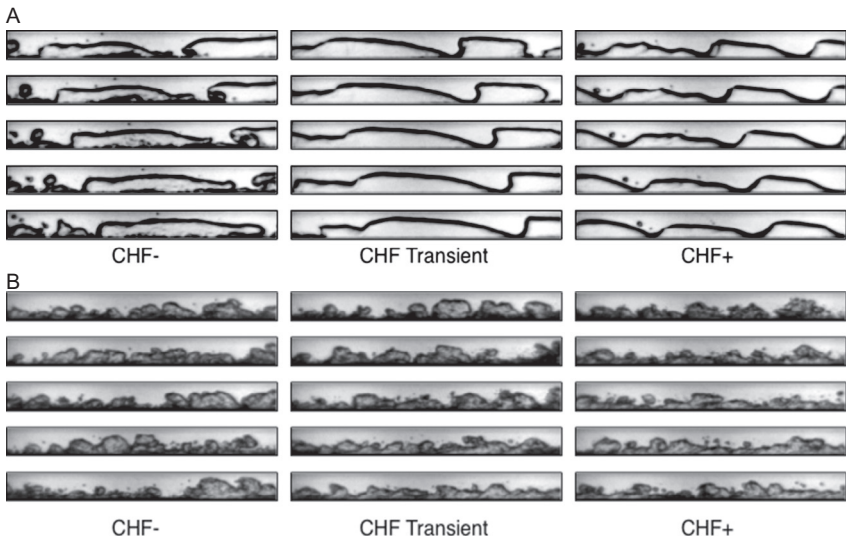

Fig. 12 CHF transient in microgravity for FC-72 at (A) $U = 0.15$ m/s and $\Delta T_{sub,out} = 3.0°C$, and (B) $U = 1.5$ m/s and $\Delta T_{sub,out} = 3.8°C$. *Adapted from H. Zhang, I. Mudawar, M.M. Hasan, Flow boiling CHF in microgravity, Int. J. Heat Mass Transfer 48 (2005) 3107–3118.*

CHF the downstream wetting front still maintaining contact with the wall. The last sequence of images shows two wetting fronts in the process of lifting away from the wall, which is the moment when wall temperatures began to escalate at a fast rate. Fig. 12B depicts sequential images of the CHF transient for a relatively high velocity of $U = G/\rho_f = 1.5$ m/s and $\Delta T_{sub,out} = 3.8°C$. Here too, vapor patches appear to propagate along the wall separated by liquid wetting fronts, but the patches are far shorter and their interface more perturbed than at 0.15 m/s.

The interfacial behavior depicted in Fig. 12A and B follows very closely the Interfacial Lift-off mechanism for flow boiling CHF proposed originally by Galloway and Mudawar [31, 32] for vertical upflow along a short heated wall.

As discussed earlier in conjunction with Fig. 5A and B, experiments by Zhang *et al.* [48] involving flow boiling in Earth gravity showed that, at low velocities, the CHF mechanism changes drastically with flow orientation because of differences in the magnitude of body force component perpendicular to the heated wall. However, experiments conducted at high velocity yielded the same wavy vapor layer behavior regardless of orientation, as high inertia negated the effects of body force. Unlike these terrestrial trends, Fig. 12A and B shows that CHF in microgravity is associated with the wavy vapor layer behavior and triggered by the same Interfacial Lift-off mechanism for both low and high velocities. This renders the Interfacial Lift-off Model especially effective at predicting flow boiling CHF in microgravity.

2.8.2 Interfacial Lift-off Model for Flow Boiling CHF

The Interfacial Lift-off Model is rooted in depiction of the wavy vapor layer behavior preceding CHF occurrence using hydrodynamic instability theory. As shown in Fig. 13A, a wavy interface separates a liquid layer of mean velocity U_f and mean thickness H_f from a vapor layer of mean velocity U_g and mean thickness H_g. Wetting front formation requires that the interfacial wavelength exceeds the critical wavelength, λ_c, given by

$$k_c = \frac{2\pi}{\lambda_c} = \frac{\rho_f'' \rho_g'' \left(U_g - U_f\right)^2}{2\sigma\left(\rho_f'' + \rho_g''\right)} + \sqrt{\left[\frac{\rho_f'' \rho_g'' \left(U_g - U_f\right)^2}{2\sigma\left(\rho_f'' + \rho_g''\right)}\right]^2 + \frac{\left(\rho_f - \rho_g\right) g_n}{\sigma}}, \quad (11)$$

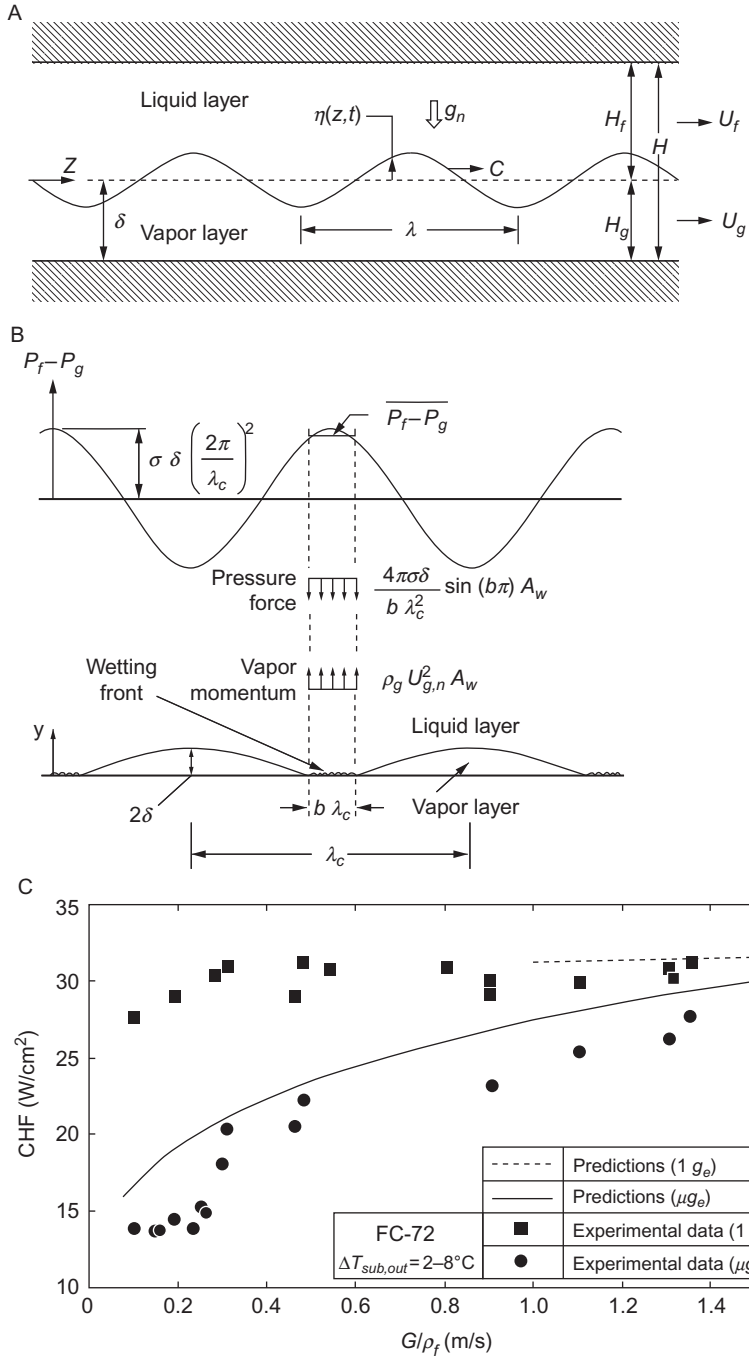

Fig. 13 (A) Wavy interface between liquid and vapor layers. (B) Interfacial Lift-off of wetting front at CHF. (C) Comparison of CHF data and Interfacial Lift-off Model predictions for microgravity and horizontal 1 g_e flow boiling. *Adapted from H. Zhang, I. Mudawar, M.M. Hasan, Flow boiling CHF in microgravity, Int. J. Heat Mass Transfer 48 (2005) 3107–3118.*

where $\rho_f'' = \rho_f \coth(kH_f)$ and $\rho_g'' = \rho_g \coth(kH_g)$ are "modified density" terms, and g_n is the component of gravity perpendicular to the heated wall. The instability theory indicates that large velocity differences tend to destabilize the interface, surface tension helps preserve interfacial stability, and normal gravity can be stabilizing or destabilizing.

The second component of the Interfacial Lift-off Model addresses the separation of wetting fronts from the wall, which is the trigger mechanism for CHF. Because of the interfacial curvature, a pressure force is produced that promotes interfacial contact with the wall, a necessary condition for sustaining the liquid replenishment. The Interfacial Lift-off Model is based on the premise that CHF will occur when the normal momentum of the vapor generated in the wetting front just exceeds the pressure force. For an interfacial wave of the form $\eta(z,t) = \eta_0 e^{ik(z-ct)}$, the pressure difference perpendicular to the wall is given by

$$P_f - P_g = -\left[\rho_f''(c-U_f)^2 + \rho_g''(c-U_g)^2 + \left(\rho_f - \rho_g\right)\frac{g_n}{k}\right] k\eta_0 e^{ik(z-ct)}. \quad (12)$$

Assuming that the wetting front occupies a fixed fraction b of the critical wavelength, the average pressure difference for the wetting front is determined by averaging over $b\lambda_c$

$$\overline{P_f - P_g} = \frac{4\pi\sigma\delta}{b\lambda^2}\sin(b\pi), \quad (13)$$

where δ is the mean vapor layer thickness. Key components of the lift-off process are depicted in Fig. 13B, where the pressure force is shown opposing the normal momentum, $\rho_g U_{g,n}^2$, of vapor emanating from the wetting front.

Using video analysis, Sturgis and Mudawar [33,34] showed that $b = 0.2$ over a broad range of flow conditions. They also detected a continuous upstream wetting region of length z^*, defined as $z^* = z_o + \lambda_c(z^*)$, where z_o is the distance from the leading edge of the heated wall to the location where U_g just surpasses U_f. They concluded that the wavy interface is first generated at z^* before propagating downstream.

To account for inlet subcooling, the heat concentrated in a wetting front is given by $q_w'' A_w = \rho_g U_{g,n} A_w (c_{p,f}\Delta T_{sub,in} + h_{fg})$, where A_w is the wetting front area. The heat flux required to lift the interface away from the wall is determined by equating the vapor momentum, $\rho_g U_{g,n}^2$, to the average pressure force given by Eq. (13):

$$q''_w = \rho_g\left(c_{p,f}\Delta T_{sub,in} + h_{fg}\right)\left(\frac{\overline{P_f - P_g}}{\rho_g}\right)^{1/2}$$
$$= \rho_g\left(c_{p,f}\Delta T_{sub,in} + h_{fg}\right)\left(\frac{4\pi\sigma}{\rho_g}\frac{\sin(b\pi)}{b}\right)^{1/2}\left.\frac{\delta^{1/2}}{\lambda_c}\right|_{z^*}. \quad (14)$$

The critical heat flux, q''_m, is the average heat flux over the entire heated area and is related to the wetting front heat flux by the relation $q''_m = bq''_w$. This yields the following analytical expression for CHF corresponding to subcooled inlet conditions:

$$q''_m = \rho_g\left(c_{p,f}\Delta T_{sub,in} + h_{fg}\right)\left(\frac{4\pi\sigma b\sin(b\pi)}{\rho_g}\right)^{1/2}\left.\frac{\delta^{1/2}}{\lambda_c}\right|_{z^*}. \quad (15)$$

It is important to note that δ and λ_c in Eq. (15) are calculated at z^* using a separated flow model that provides axial variations of U_f, U_g, and δ. Detailed relations for the separated flow model are provided in Ref. [49].

Fig. 13C shows variations of flow boiling CHF data obtained in microgravity by Zhang *et al.* vs $U(= G/\rho_f)$ in microgravity and in Earth gravity. In microgravity, CHF is shown increasing appreciably with increasing velocity, compared to a much milder increase in Earth gravity. Notice how microgravity CHF at the lowest velocity is only 50% of that at 1 g_e. Increasing velocity is shown reducing CHF differences between the two gravities, culminating in near convergence around 1.5 m/s. Fig. 13C also shows CHF predictions based on the Interfacial Lift-off Model. Notice that, while the model predictions for microgravity are provided for the entire velocity range tested, predictions for 1 g_e are only shown for relatively high velocities. Absence of predictions for lower velocities at 1 g_e is based on the observation that flow boiling CHF in horizontal flow at these velocities is dominated by the *Pool-Boiling Regime*, Fig. 5A, whereas the Interfacial Lift-off Model, as discussed earlier, is valid for all velocities in microgravity, but only a subset of velocities and orientations in Earth gravity. Fig. 13C also demonstrates the accuracy of the model predictions for the relevant velocity ranges in both gravities. The convergence of CHF data above 1.5 m/s has important practical implications concerning the design of two-phase thermal hardware in space systems. It proves that, above this velocity threshold, the flow becomes inertia-dominated, allowing high-velocity 1 g_e data, correlations, and models to be safely implemented in the design of space systems.

2.8.3 Pre-ISS Parabolic Flight Flow Boiling CHF Experiments Using the FBCE's FBM

Recently, collaborative efforts between Purdue University and NASA-GRC have been focused on assessing the design integrity and instrumentation of the FBM prior to insertion of the FBCE into the FIR onboard the ISS [94,95]. This effort is also intended to obtain preliminary data and video records for flow boiling CHF in reduced gravity. Unlike the earlier experiments by Zhang *et al.* [93], which utilized a flow channel that was heated along only one side, the FBM featured heating on two opposite sides of the rectangular flow channel.

The experiments were performed in microgravity in a series of parabolic maneuvers onboard a modified Boeing 727 aircraft. The entire flight facility, including the flow loop hardware, data acquisition system, power and instrumentation cabinets, and high-speed camera, was mounted onto a rigid aluminum frame shown in Fig. 14A. Fig. 14B shows a schematic of the two-phase flow loop that was configured to deliver FC-72 to the FBM at desired operating conditions.

Design of the FBM enabled simultaneous heat transfer measurements and high-speed video motion analysis of interfacial features. Depicted in Fig. 15A and B, the FBM consists of three transparent polycarbonate plastic (Lexan) plates that are bolted together between two aluminum support plates. The rectangular flow channel has a cross-sectional area of 5.0×2.5 mm^2, which is identical to the channel dimensions adopted in earlier studies by Zhang *et al.* [93]. The top and bottom plastic plates are milled out to insert 15.5-mm wide, 114.6-mm long, and 1.04-mm thick copper slabs that serve as heating walls along the two opposite 2.5-mm sides of the flow channel, with each copper slab heated by a series of thick-film resistors. Fig. 15C shows key dimensions of the channel, including a flow development length of 327.9 mm, a heated length of 114.6 mm, and an exit length 60.9 mm.

Fig. 16 shows sequential images captured in microgravity before (CHF−, corresponding to $95 \pm 1\%$ of CHF), during the CHF transient, and just after CHF (CHF+) for $U = 0.1$, 0.9, and 1.9 m/s. For $U = 0.1$ m/s, CHF− is associated with the development of wavy vapor layers starting at the leading edge of the channel's heated region. Notice the appreciable meshing between the two wavy vapor layers from the opposite heated walls upstream, as compared to merging of the vapor layers downstream. Despite the merging of the vapor layers, the heated walls appear to be replenished in the downstream region by liquid ligaments that are entrained in the

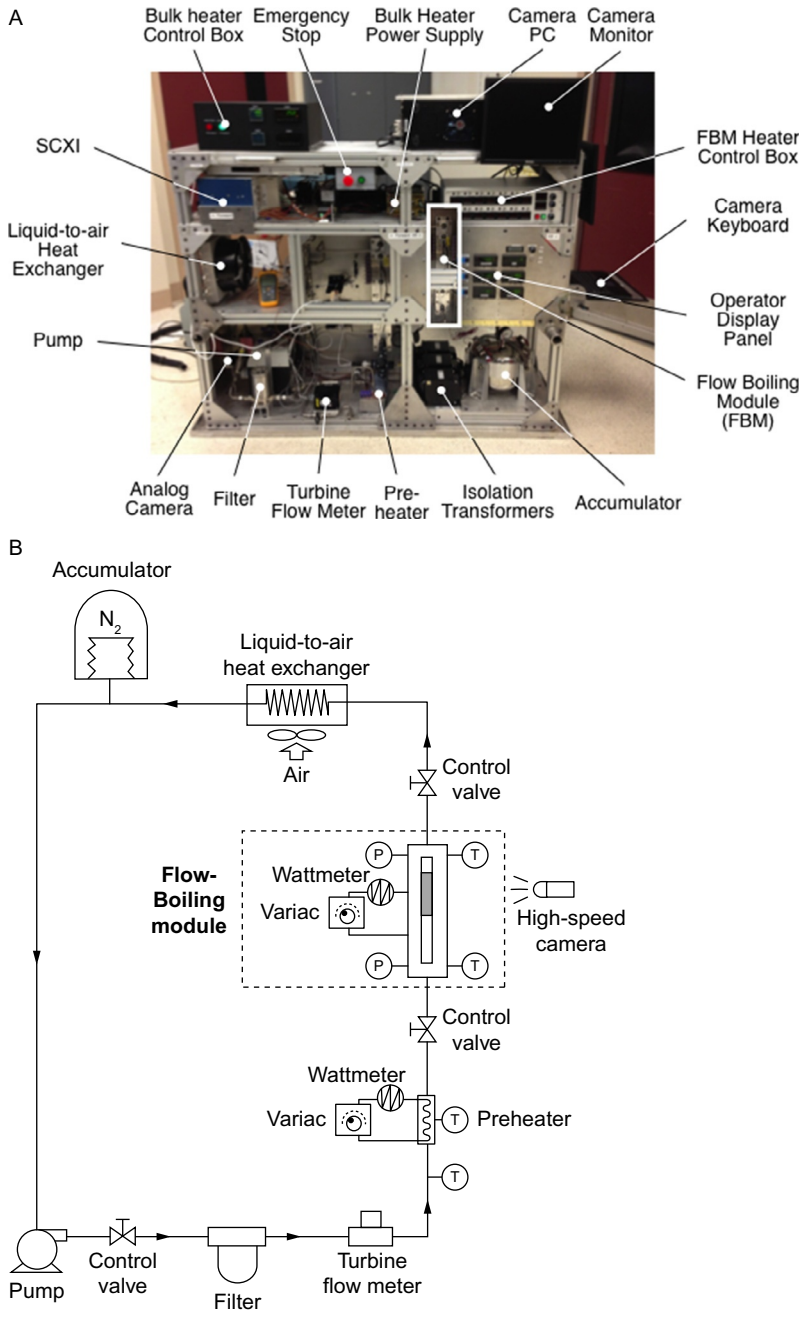

Fig. 14 (A) Image of Flow Boiling Module (FBM) parabolic flight facility. (B) Schematic diagram of flow loop.

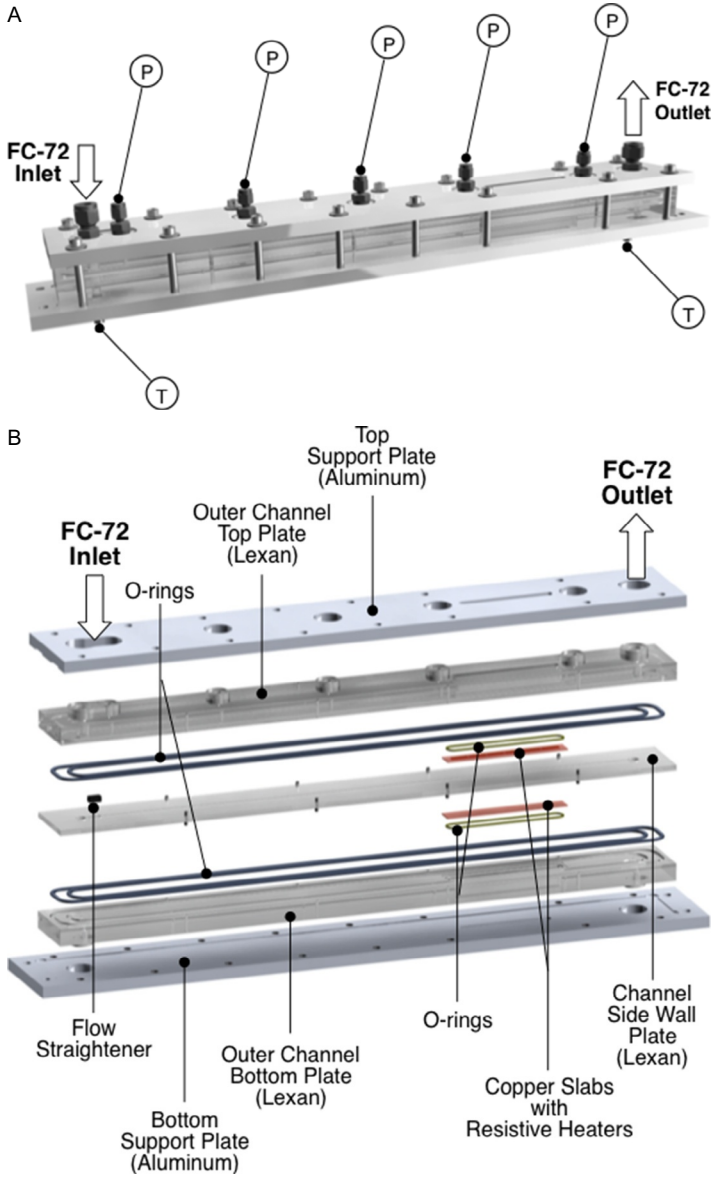

Fig. 15 Construction of FBM: (A) assembly view, (B) exploded view, and (C) key dimensions of flow channel.

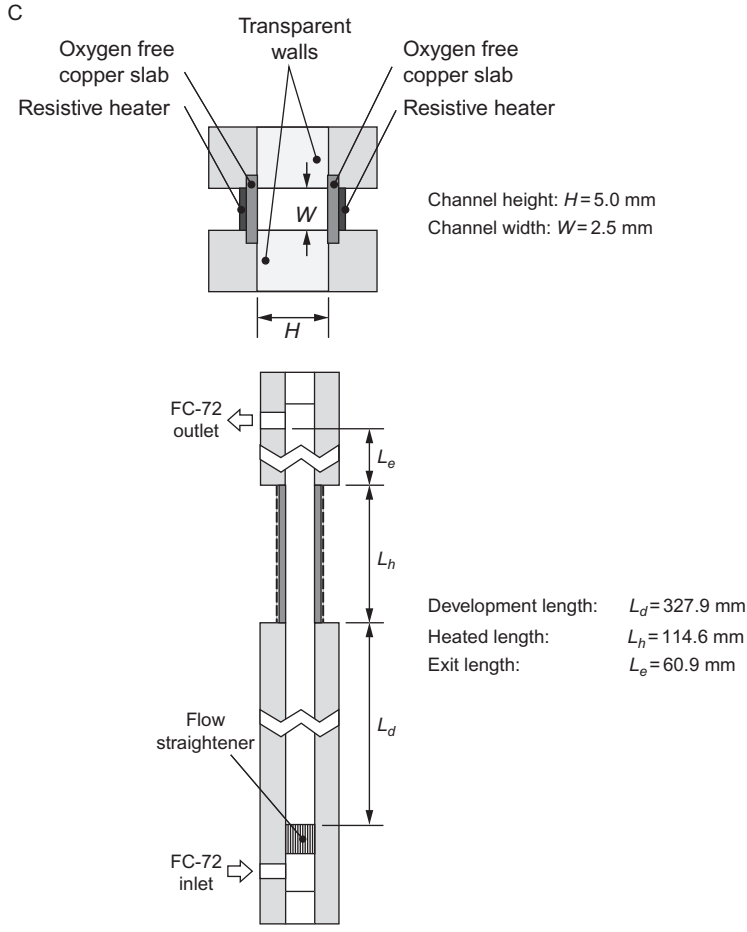

Fig. 15—Cont'd

coalescent vapor flow. During the CHF transient, the downstream region is occupied almost entirely by vapor, and residual cooling appears to be concentrated in a few upstream wetting fronts. At CHF+, the upstream wetting fronts are extinguished, depriving the heated walls from any further access to the core liquid. At $U=0.9$ m/s, the wavy vapor layers at CHF− are much thinner than at $U=0.1$ m/s, which causes a shift in both the meshing and merging of the vapor layers downstream. Notice also the substantial increase in the number of wetting fronts caused by smaller interfacial wavelength. During the CHF transient, the downstream regions begin to dry out, while CHF+ is accompanied by extinguishing of wetting fronts both upstream

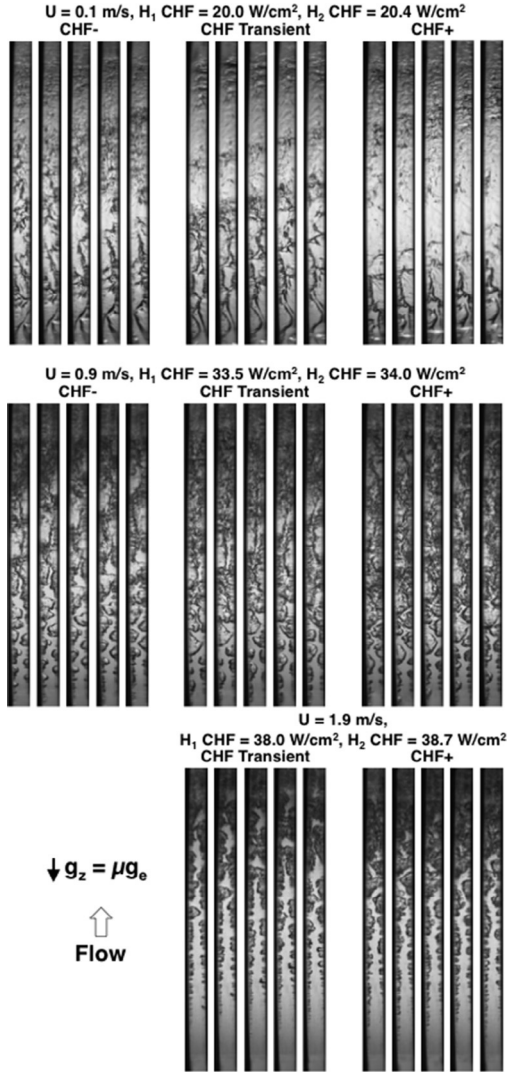

Fig. 16 Sequential high-speed video images from FBM for different inlet velocities obtained at CHF−, during CHF transient, and at CHF+. *Adapted from C. Konishi, H. Lee, I. Mudawar, M.M. Hasan, H.K. Nahra, N.R. Hall, J.D. Wagner, R.L. May, J.R. Mackaey, Flow boiling in microgravity: part 2—critical heat flux interfacial behavior, experimental data, and model, Int. J. Heat Mass Transfer 81 (2015) 721–736.*

and in the middle of the heated region. At the highest inlet velocity of $U = 1.9$ m/s, it was not possible to capture CHF− conditions with video, but images during the CHF transient capture a further decrease in thicknesses of the opposite vapor layers, a shift in the meshing between the vapor layers

farther downstream, and an increase in the number of wetting fronts. At CHF+, wall dryout appears to result from downstream merging between the two vapor layers as well as loss of wetting fronts.

With the video analysis confirming the crucial role of wetting fronts in flow boiling CHF, it is interesting to reassess the validity of the Interfacial Lift-off Model to double-sided heating and operating parameters of the FBM in both microgravity and Earth gravity. Fig. 17A and B shows instability representations of flow boiling at CHF− in Earth gravity and microgravity, respectively. The vapor–liquid interfaces are assumed to acquire simple sinusoidal waveforms as proposed in the original Interfacial Lift-off Model. As discussed earlier, while flow boiling experiments conducted at different orientations in Earth gravity have been widely used to simulate reduced gravity effects, such experiments suffer important limitations that are clearly apparent when comparing Fig. 17A and B. Aside from the magnitude of body force, there are fundamental differences between double-sided heating in microgravity and at different orientations in Earth gravity. In the latter, the components of gravity perpendicular to the heated walls yield different instability behaviors for the two vapor layers. As shown in Fig. 17A, the gravitational component normal to the upward-facing heated wall and the downward-facing heated wall are expressed, respectively, as

$$g_{n,1} = g_e \cos\theta \tag{16a}$$

and

$$g_{n,2} = g_e \cos(\theta + \pi) = -g_e \cos\theta. \tag{16b}$$

Notice that the gravitational body force tends to destabilize the interface adjacent to the upward-facing heated wall and stabilize the interface along the downward-facing heated wall. This implies that the interface along the downward-facing wall can be either stable or unstable, and, when unstable, acquire a critical wavelength larger than that of the upward-facing wall. For an unstable interface along the downward-facing wall, interfacial curvature in the wetting fronts is weaker, which produces a lower CHF for the downward-facing wall compared to the upward facing. Notably, those CHF differences are more pronounced at low velocities, where body force effects are most pronounced. On the other hand, CHF differences between the two walls decrease monotonically with increasing velocity. It is also important to note that strictly equal CHF values for the two opposite walls are achieved in Earth gravity only in vertical upflow because of zero gravitational body force normal to the walls for this orientation.

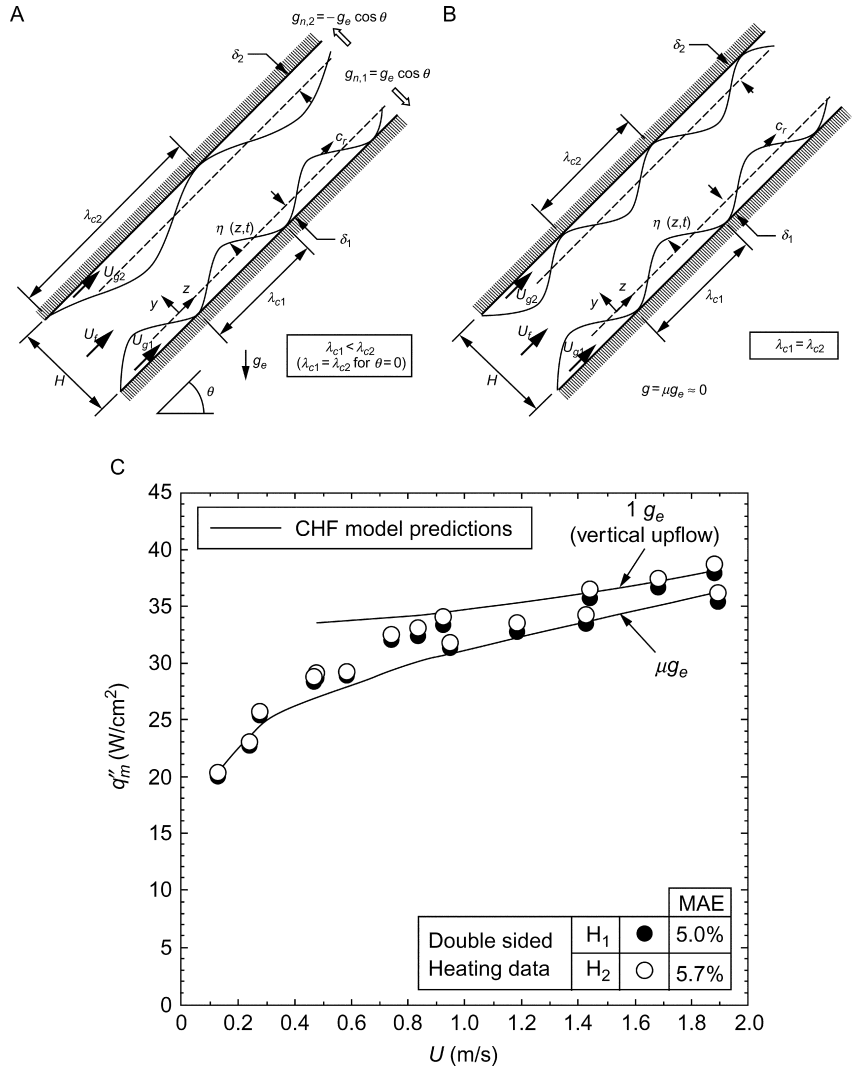

Fig. 17 Hydrodynamic instability of wavy vapor layers along heated walls of FBM at CHF – (A) for inclined channel at 1 g_e and (B) for microgravity. (C) Comparison of CHF data measured in the FBM vs inlet velocity for microgravity, along with predictions for both microgravity and vertical upflow in Earth gravity based on the Interfacial Lift-off Model. *Adapted from C. Konishi, H. Lee, I. Mudawar, M.M. Hasan, H.K. Nahra, N.R. Hall, J.D. Wagner, R.L. May, J.R. Mackaey, Flow boiling in microgravity: part 2—critical heat flux interfacial behavior, experimental data, and model, Int. J. Heat Mass Transfer 81 (2015) 721–736.*

Fig. 17C shows microgravity CHF data measured in the FBM vs inlet velocity, along with predictions for both microgravity and vertical upflow in Earth gravity based on the Interfacial Lift-off Model. Like the earlier one-sided wall heating data of Zhang *et al.* [93], double-sided microgravity CHF is quite small at low velocities and increases monotonically with increasing velocity. The Interfacial Lift-off Model shows excellent predictive accuracy, evidenced by very low mean absolute errors for both heated walls H_1 and H_2. Fig. 17C also shows predicted CHF values for the two gravitational environments tending to converge above $U \sim 1$ m/s. Notice that this velocity value is lower than that obtained by Zhang *et al.* (1.5 m/s) for convergence of microgravity and Earth gravity CHF data. This can be explained by growth of vapor layers on two opposite walls in double-sided heating yielding higher acceleration along the channel and therefore greater inertia than single-sided heating for the same inlet velocity.

These findings confirm the single-sided microgravity results of Zhang *et al.* in terms of low CHF values at low velocities, monotonic increase in CHF with increasing velocity, and convergence of microgravity and Earth gravity CHF values at high velocities. These double-sided heating results also confirm key premises of the Interfacial Lift-off Model, most notably the formation of a wavy vapor layer and wetting fronts along the heated walls at CHF−, and loss of wetting fronts as a trigger mechanism for CHF.

3. FLOW CONDENSATION IN REDUCED GRAVITY

3.1 Fundamental Challenges to Accurate Prediction of Pressure Drop and Heat Transfer Coefficient in Flow Condensation in Earth Gravity

Condensers are thermal devices found in numerous industries, including power generation, food, pharmaceutical, and space. They also constitute one of the primary components of any refrigeration or air conditioning system. Condensers are available in a wide variety of designs, with some relying on gravity to move the condensate liquid, while the flow in most is shear driven by the vapor flow. Regardless of the condenser design, formation of the condensate film has a strong bearing on the condenser's heat transfer performance. In fact, the high condensation heat transfer coefficients commonly achieved in condensers are a direct result of the film's transport behavior. For very thin films, heat transfer across the film is dominated by conduction, while thicker films also take advantage of flow turbulence.

For condensation in tubes, which is the configuration best suited for space applications, the flow is introduced in mostly vapor state. By maintaining wall temperature below the vapor's saturation temperature, heat is transferred to the wall by gradual conversion of vapor into liquid. A succession of flow regimes is possible, Fig. 18A, starting with the annular flow regime, where a thin liquid film begins to sheathe the inner walls of the tube, driven mostly by the shear forces exerted by the vapor core. The film grows gradually in thickness and waves begin to form along the film's interface. Eventually, wave peaks from opposite sides of the tube begin to merge, signaling transition to slug flow. This regime is comprised of a series of oblong bubbles separated by liquid slugs. Further condensation along the tube gradually decreased the length of bubbles until a bubbly flow regime is established. Finally, all remaining vapor is converted into liquid.

Annular flow regime is arguably the most important condensation regime, given that it contributes the highest heat transfer coefficients as well as tends to occupy a significant fraction of the tube length in most practical applications. This explains that the emphasis investigators have placed on modeling this regime compared to all other regimes combined.

The vast majority of published studies concerning the prediction of pressure drop and heat transfer coefficient in terrestrial condensing flows is based on the separated flow semiempirical Lockhart–Martinelli formulation [80] and empirical correlations [96–103]. Like all correlations, validity of predictions is limited to fluids and operating conditions of the databases used to derive the correlations. More recently, two other types of predictive tools have been proposed: theoretical control-volume-based models and universal correlations. The former employ mass, momentum, and energy conservation relations to control volumes encompassing the liquid and vapor portions of the flow separately, along with appropriate interfacial boundary conditions [104]. The universal correlations are derived using a consolidated database amassed from available published databases and involve numerous fluids, and broad ranges of inlet pressure, inlet quality, mass velocity, and tube diameter and tube length [105,106].

Despite the recent successes in predicting pressure drop and heat transfer coefficient in terrestrial condensation applications, several fundamental challenges remain when attempting to develop accurate models. As shown in Fig. 18, they include (a) flow-pattern transition along the condensation length, (b) damping of turbulence along the annular film interface, (c) circumferential asymmetry of the annular film due to transverse body force for inclined channels, and (d) interfacial waves.

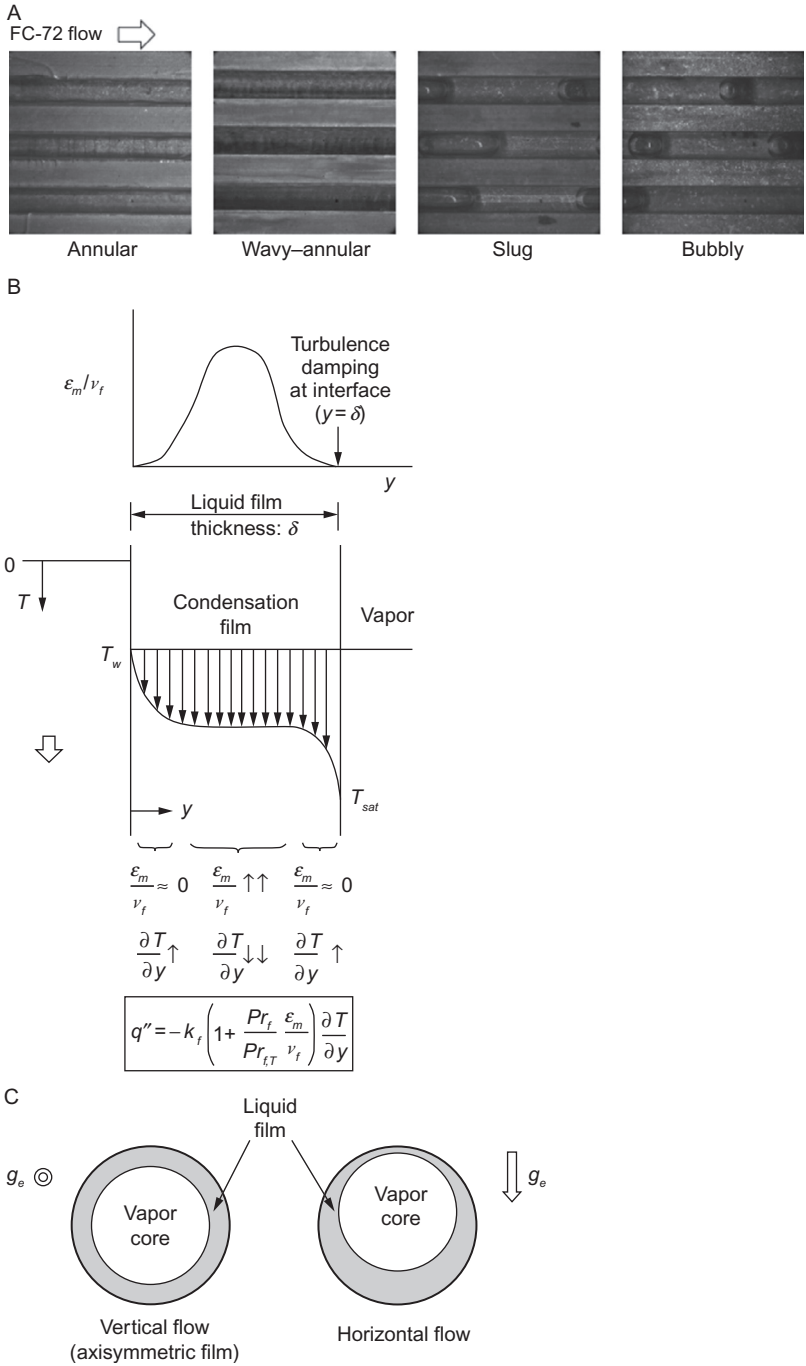

Fig. 18 Challenges in modeling flow condensation: (A) accurate assessment of dominant flow pattern, (B) damping of turbulence along annular film interface, (C) circumferential asymmetry of annular film due to transverse body force, and (D) interfacial waves.

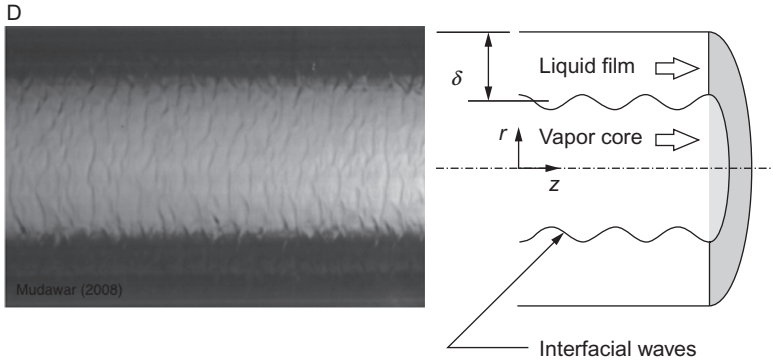

Fig. 18—Cont'd

A major challenge in modeling annular flows is accurate determination of turbulent or eddy diffusivity across the annular liquid film. Studies by Hubbard *et al.* [107], Ueda *et al.* [108], and Mudawar and El-Masri [109] have shown that classical turbulence models fail to capture eddy behavior near the liquid–vapor interface. As discussed by Mudawar and El-Masri, surface tension forces along the interface cause significant damping of turbulent eddies, resulting in appreciable resistance to heat transfer near the interface. They also showed that ignoring this effect results in appreciable error in predicting the film's heat transfer coefficient. Interestingly, this behavior is also found in falling liquid films subjected to wall heating [110–113].

Flow orientation relative to Earth gravity can have a profound influence on the condensation heat transfer. This influence is reflected in asymmetry of the liquid film distribution along the tube's inner perimeter. Orientation effects are especially important at low mass velocities, where weak vapor shear heightens the influence of gravity on the film's motion. As will be discussed later, high mass velocities can be used to negate the film's asymmetry.

Another source of difficulty in modeling annular flow is interfacial waves [110–114]. These are highly complex phenomena and no effective method is presently available to account for their effects. One category of waves is ripples, featuring both small amplitude and small wavelength. Another category is large waves, where the perturbed liquid film is replaced by lumps of liquid (wave peaks) separated by thin layers of liquid. With appreciable penetration of the wave peaks into the vapor flow, the motion of the liquid lumps can be dominated by vapor drag forces rather than by interfacial vapor shear. Two phenomena that are closely related to interfacial waviness are droplet entrainment and droplet deposition. The former refers to liquid

droplet breakoff from the wave crests and entrainment into the vapor core, while deposition refers to droplets from the vapor core falling back upon the annular film.

3.2 Terrestrial Studies on the Influence of Body Force on Flow Condensation

3.2.1 Flow Orientation Effects on Flow Condensation at 1 g_e

Condensation pressure drop and heat transfer characteristics are highly flow regime dependent. While the topic of condensation flow regime determination is widely available in the literature, the vast majority of published works have been focused on horizontal flow [115–122]. But, as discussed earlier, flow orientation can have a profound influence on the distribution of liquid and vapor inside the tube, and therefore flow regime, pressure drop, and heat transfer coefficient [123]. It is therefore crucial to develop a detailed understanding of the influence of gravity on interfacial behavior, especially for the annular flow regime which provides the highest heat transfer coefficients and prevails over the largest fraction of the condensation length compared to all other flow regimes combined.

By far, the simplest and most cost-effective method to understanding these body force effects is to perform condensation experiments at different flow orientations in Earth gravity. Aside from quantifying the influence of body force, these experiments can identify the operating conditions (especially mass velocity) required to negate body force effects. Investigators have also relied on adiabatic air–water experiments to develop flow regime maps for different orientations [124] and to explore variations in pressure drop [125] and void fraction for different orientations [126]. However, there is insufficient proof that findings from adiabatic experiments are applicable to condensing flows.

As indicated by Lips and Meyer [123], studies addressing flow condensation for different orientations are quite sparse. Chato [127] concluded that the heat transfer coefficient for condensation in tubes with a slight downward inclination increases with increasing inclination angle because of decreased depth of liquid in the tube. Wang and Du [128] explored laminar condensation in inclined tubes both experimentally and theoretically and reported that the condensation heat transfer coefficient can be increased or decreased depending on inclination angle, tube diameter, vapor quality, and mass velocity. They constructed an analytical model relating the influence of gravity to liquid film thickness, which showed good predictions of both the shape of the liquid–vapor interface and heat transfer coefficient for

stratified flow. Akhavan-Behabadi *et al.* [129] experimentally investigated the effects of flow orientation on condensation of R-134a inside a microfin tube and showed that heat transfer coefficients for downflow are higher than those for upflow. Nitheanandan and Soliman [130] explored experimentally the influence of small inclination angles on flow regime boundaries for steam condensation. Overall, they found that this influence was insignificant for annular flow, while even small variations in inclination angle had profound influence on wavy and slug flow regime boundaries. In a follow-up study, Nitheanandan and Soliman [131] proposed a mechanistic model for transition between stratified and nonstratified flows. Lips and Meyer [132] investigated experimentally the condensation of R-134a over the full range of tube orientations between vertical downflow and vertical upflow. They observed that the heat transfer coefficient is dependent on flow regime, which in turn is governed by the relative magnitude of body force, interfacial shear, and surface tension. A key finding from their study is that the flow regime variations with orientation angle are strongly dependent on mass velocity, with low mass velocities at low vapor qualities yielding high sensitivity to orientation, and high mass velocities culminating in annular flow regardless of orientation angle.

With the recent increased interest in both high-flux and compact thermal management hardware, emphasis in condensation research has shifted from macro to mini/microchannel flows. Wang and Rose [133] developed an analytical model addressing the influence of orientation on local liquid film thickness and mean heat transfer coefficient for condensation of R-134a in square microchannels corresponding to orientations ranging from vertical upflow to vertical downflow. Because of the small hydraulic diameter and low flow rates considered, the model accounted for surface tension and interfacial curvature but neglected inertia and convection effects. Saffari and Naziri [134] conducted a theoretical and numerical investigation of stratified condensation of R-141b, R-11, and R-134a. They concluded that condensation is strongly influenced by the tube's inclination angle, with 30–50° above horizontal yielding the best heat transfer performance. Da Riva and Del Col [135] numerically simulated condensation of R-134a in a circular minichannel for horizontal flow and vertical downflow in Earth's gravity as well as in zero gravity. They concluded that gravity has a dominant influence at low mass velocities, with horizontal flow yielding higher heat transfer coefficients than vertical downflow. However, the influence of gravity gradually diminished with increasing mass velocity.

3.2.2 Recent Assessment of Condensation Flow Regimes for Different Orientations Relative to Earth Gravity

As a prelude to development of the FBCE for the ISS, extensive experiments were performed at the PU-BTPFL in pursuit of detailed understanding of the variations of interfacial behavior and heat transfer coefficient for condensation at different orientations relative to Earth gravity [136,137]. Fig. 19A shows a photo of the experimental facility that was constructed for this purpose. The main component of the facility is the condensation module, along which FC-72 vapor is gradually condensed to liquid by rejecting heat to a counter flow of cooling water.

Two separate condensation modules were tested in this facility, one dedicated to flow visualization and the other to heat transfer measurements. The two modules have fairly similar dimensions but are constructed from different materials to facilitate video capture in the first and heat transfer measurement in the second. Illustrated in Fig. 19B, the condensation module for flow visualization features transparent tube-in-tube construction, with FC-72 condensing along the inner tube and water flowing in counterflow through the annulus between the inner and outer tubes. The inner tube is fabricated from borosilicate glass and is 1219-mm long with 10.16-mm i.d. and wall thickness of 1.8 mm. The outer tube is constructed from polycarbonate plastic (Lexan) and has an i.d. of 19.05 mm and an outer diameter of 24.4 mm. An effective condensation length of 1143 mm is achieved between short rubber sleeves that are secured between the inner and outer tubes at both the inlet and outlet of the condensation module. The flow visualization experiments were performed with the aid of a high-speed Photron Fastcam Ultima APX video camera system at the inlet, middle, and outlet regions of the condensation length centered, respectively, at 190, 571, and 952 mm from the FC-72 inlet for three orientations: vertical downflow, vertical upflow, and horizontal flow.

Fig. 19C illustrates the construction of the condensation module for heat transfer measurements, which features inner and outer tubers made from 304 stainless steel and a condensation length of 1259.8 mm. The inner tube has an i.d. of 11.89 mm and 0.41-mm wall thickness, and the outer tube 22.48-mm i.d. and 3.05-mm wall thickness. Aside from temperature and pressure instrumentation at the inlets and outlets for both FC-72 and water, this module contains 28 thermocouples that are installed in 14 diametrically opposite pairs on the outer surface of the inner tube, and 14 thermocouples inserted into the annulus to measure water temperatures at the same axial locations as the wall thermocouples.

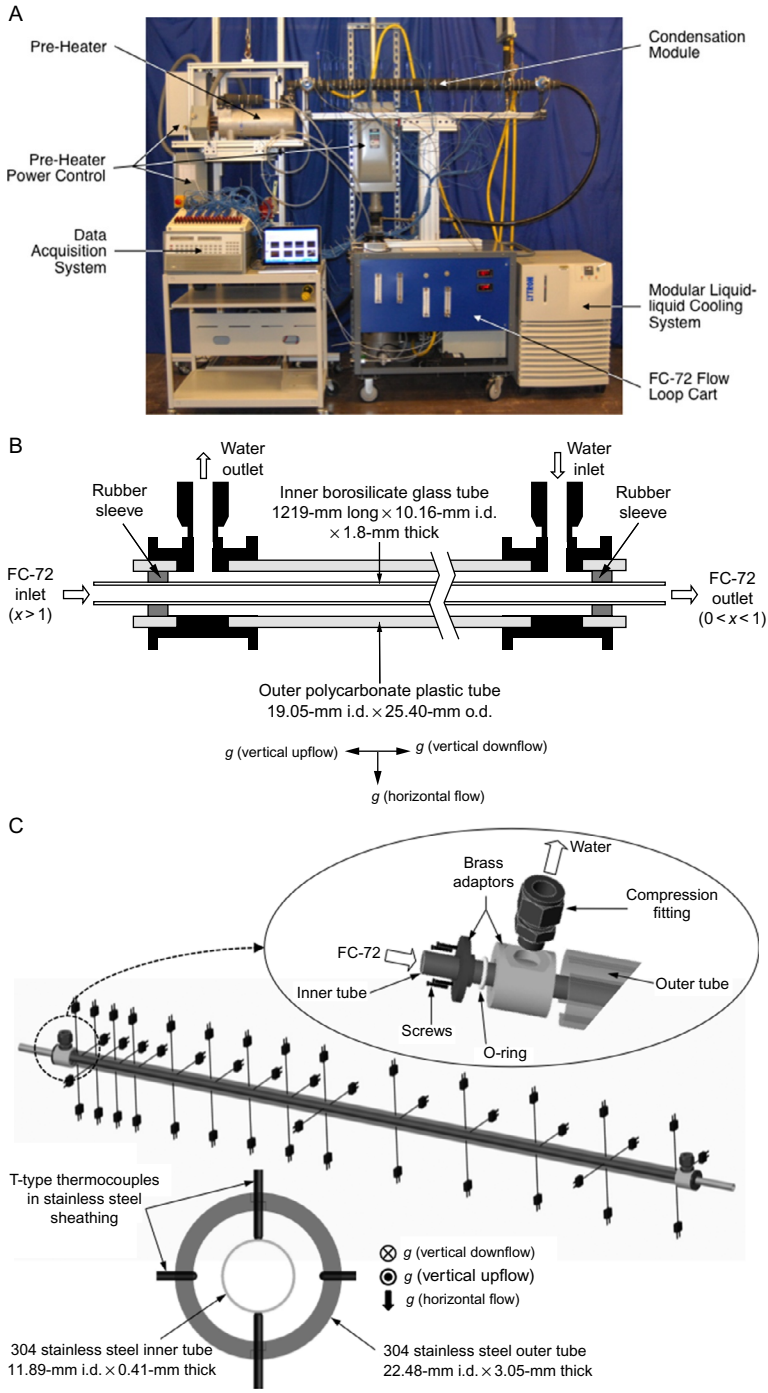

Fig. 19 (A) Photo of ground condensation orientation facility. (B) Flow visualization condensation module. (C) Heat transfer condensation module.

Using both condensation modules, experiments were performed with different FC-72 and water mass velocities for different flow orientations, with the inlet thermodynamic equilibrium quality of FC-72 maintained slightly above unity.

Fig. 20 shows, for relatively low FC-72 mass velocities and all three flow orientations, sequential images of the condensing film along the inner wall of the glass tube in the flow visualization module, captured in the middle region centered at 571 mm from the FC-72 inlet. Fig. 20A shows images for horizontal flow with mass velocities for FC-72 and water of $G = 39.94$ kg/m^{2}s and $G_w = 45.83$ kg/m^{2}s, respectively. The film is clearly stratified, which demonstrates the strong influence of gravity at low FC-72 mass velocities, and marred by interfacial waves brought about by large velocity differences between the vapor and liquid. However, the amplitude of the waves is too small to enable any liquid contact with the top of the tube. Fig. 20B shows images of the film in vertical downflow condensation, again for a relatively low FC-72 mass velocity of $G = 38.48$ kg/m^{2}s with $G_w = 41.98$ kg/m^{2}s. The film in this case appears relatively smooth and laminar, with few ripples propagating along the interface. Notice also the circumferential symmetry in film thickness caused by the gravity acting in the same direction as the FC-72 flow. Fig. 20C shows the film in vertical upflow condensation for $G = 39.96$ kg/m^{2}s and $G_w = 45.85$ kg/m^{2}s. Here, the liquid film exhibits *falling film* behavior, moving downward opposite to the vapor flow, which is the result of low flow inertia causing the liquid motion to be dominated by gravity. The flow appears to undergo transient variations associated with appreciable changes in interfacial behavior. For a brief period, the liquid forms an annular film, but with liquid ligaments and droplets being shattered from the film, entrained upward in the vapor core, or deposited back onto the liquid film. This complex interfacial behavior produces brief periods of well-mixed two-phase flow, which is quickly replaced by the previous annular film flow, and the flow sequence is then repeated in a cyclical manner. For vertical upflow, motion of the liquid film is governed by the relative magnitude of the shear stress created by the upward moving vapor core and the gravitational force acting in the opposite direction; breakdown of the flow into brief periods of well mixed two-phase flow is indicative of weak vapor shear. Comparing Fig. 20A–C reveals profound differences in the liquid film flow behavior for the different orientations, which is brought about by the relatively strong influence of gravity at low FC-72 mass velocities.

Fig. 21 shows, for relatively high FC-72 mass velocities and all three flow orientations, sequential images of the condensing film captured in the inlet

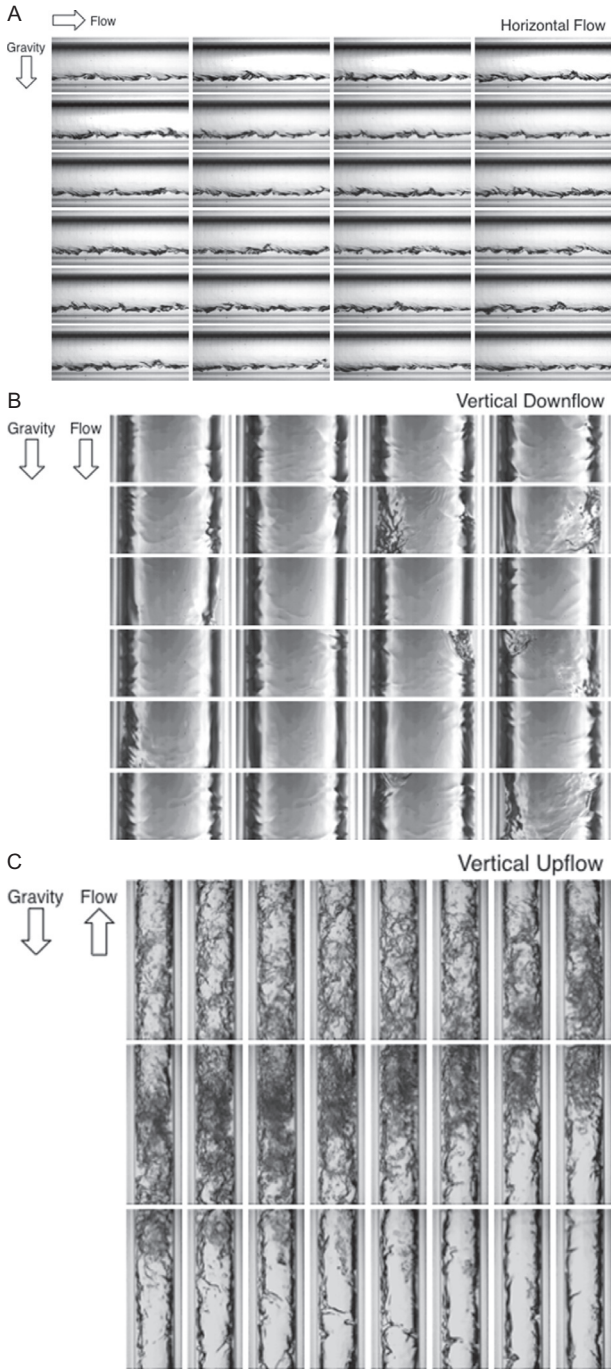

Fig. 20 Sequential images of condensing flow in Earth gravity for relatively low FC-72 mass velocities of (A) $G = 39.94$ kg/m^{2}s with $G_w = 45.83$ kg/m^{2}s in horizontal flow, (B) $G = 38.48$ kg/m^{2}s with $G_w = 41.98$ kg/m^{2}s in vertical downflow, and (C) $G = 39.96$ kg/m^{2}s with $G_w = 45.85$ kg/m^{2}s in vertical upflow. The total duration of each sequence is 0.3 s, with individual images separated by 0.0125 s. *Adapted from I. Park, L.E. O'Neill, I. Mudawar, Assessment of body force effects in flow condensation, part I: Experimental investigation of liquid film behavior for different orientations, Int. J. Heat Mass Transfer 106 (2017) 295–312.*

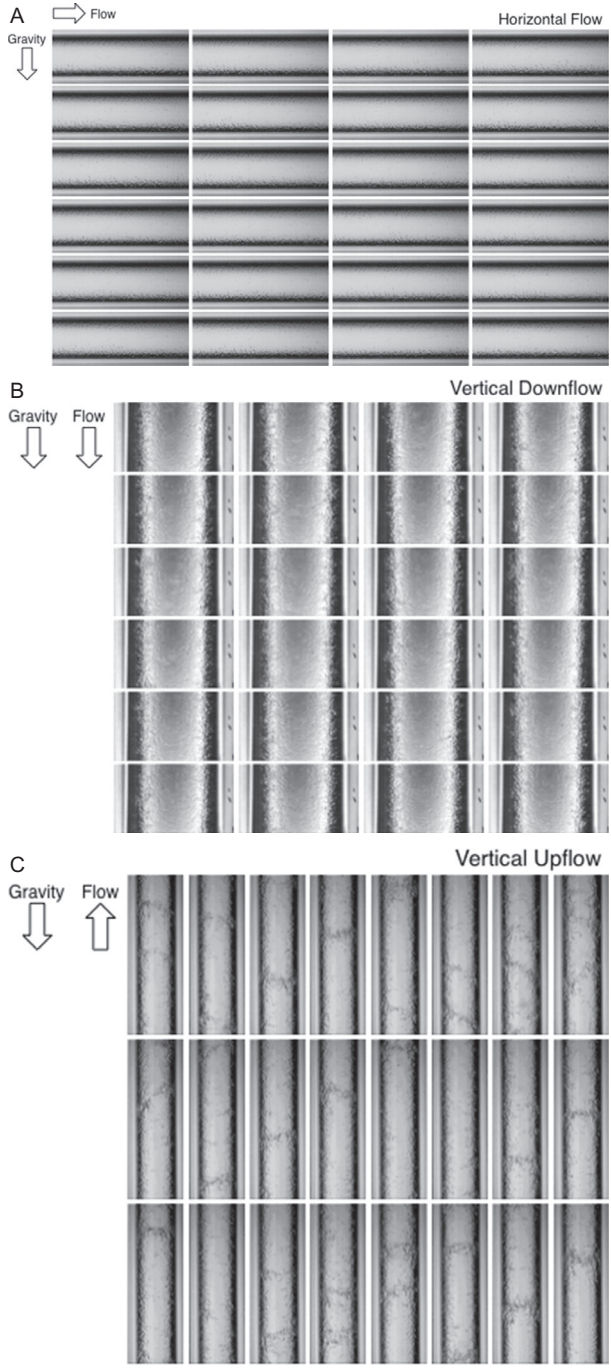

Fig. 21 Sequential images of condensing flow in Earth gravity for relatively high FC-72 mass velocities of (A) $G = 132.95\ \text{kg/m}^2\text{s}$ with $G_w = 122.21\ \text{kg/m}^2\text{s}$ in horizontal flow, (B) $G = 136.51\ \text{kg/m}^2\text{s}$ with $G_w = 125.93\ \text{kg/m}^2\text{s}$ in vertical downflow, and (C) $G = 132.97\ \text{kg/m}^2\text{s}$ with $G_w = 122.21\ \text{kg/m}^2\text{s}$ in vertical upflow. The total duration of each sequence is 0.3 s, with individual images separated by 0.0125 s. *Adapted from I. Park, L.E. O'Neill, I. Mudawar, Assessment of body force effects in flow condensation, part I: Experimental investigation of liquid film behavior for different orientations, Int. J. Heat Mass Transfer 106 (2017) 295–312.*

region, centered at 190 mm from the FC-72 inlet. High FC-72 velocities are associated with high vapor core velocities and therefore high interfacial shear, which tends to negate the influence of gravity. This is quite evident in the horizontal flow images in Fig. 21A corresponding to $G = 132.95$ kg/m^{2}s and $G_w = 122.21$ kg/m^{2}s. Notice how the film is spread rather uniformly along the inner perimeter, indicating that the film's motion is dominated by vapor shear. Further evidence of the shear-driven film motion is captured in Fig. 21B and C for vertical downflow with $G = 136.51$ kg/m^{2}s and $G_w = 125.93$ kg/m^{2}s, and vertical upflow with $G = 132.97$ kg/m^{2}s and $G_w = 122.21$ kg/m^{2}s, respectively, which show film behavior similar to that for horizontal flow. Comparing Fig. 21A–C proves that the high vapor shear achieved at high mass velocities can negate altogether any gravity influence.

While these images were obtained using the flow visualization module, heat transfer coefficient data were obtained separately using the condensation module for heat transfer measurements. Aside from amassing heat transfer data for different mass velocities and different orientations, one of the primary goals of the heat transfer measurements was to determine the combination of operating conditions that render condensation heat transfer independent of gravity. Fig. 22 compares the average heat transfer coefficient vs FC-72 mass velocity for the three flow orientations. At low mass velocities, the average heat transfer coefficient is highest for vertical downflow and lowest for vertical upflow, with values for horizontal flow falling in between. As discussed earlier, these differences are the result of strong body force effects at low mass velocities aiding liquid film motion for vertical downflow and opposing it for vertical upflow, while causing appreciable stratification for horizontal flow. Increasing the mass velocity is shown causing gradual convergence of average heat transfer coefficients for the three orientations, calumniating is virtually equal values at the highest mass velocities tested. Fig. 22B provides an alternative representation of the influence of mass velocity by showing the average heat transfer coefficients for vertical upflow and downflow normalized by those for horizontal flow vs G/ρ_f. Fig. 22A and B show average heat transfer coefficients for the three orientations converging at a critical mass velocity of $G_{crit} = 424$ kg/m^{2}s.

3.2.3 Criteria for Negating Body Force Effects Based on Terrestrial Experiments Involving Different Flow Orientations at 1 g_e

O'Neill *et al.* [137] recently developed mechanistic criteria for negating the influence of gravity on flow condensation. Recognizing that the influence of

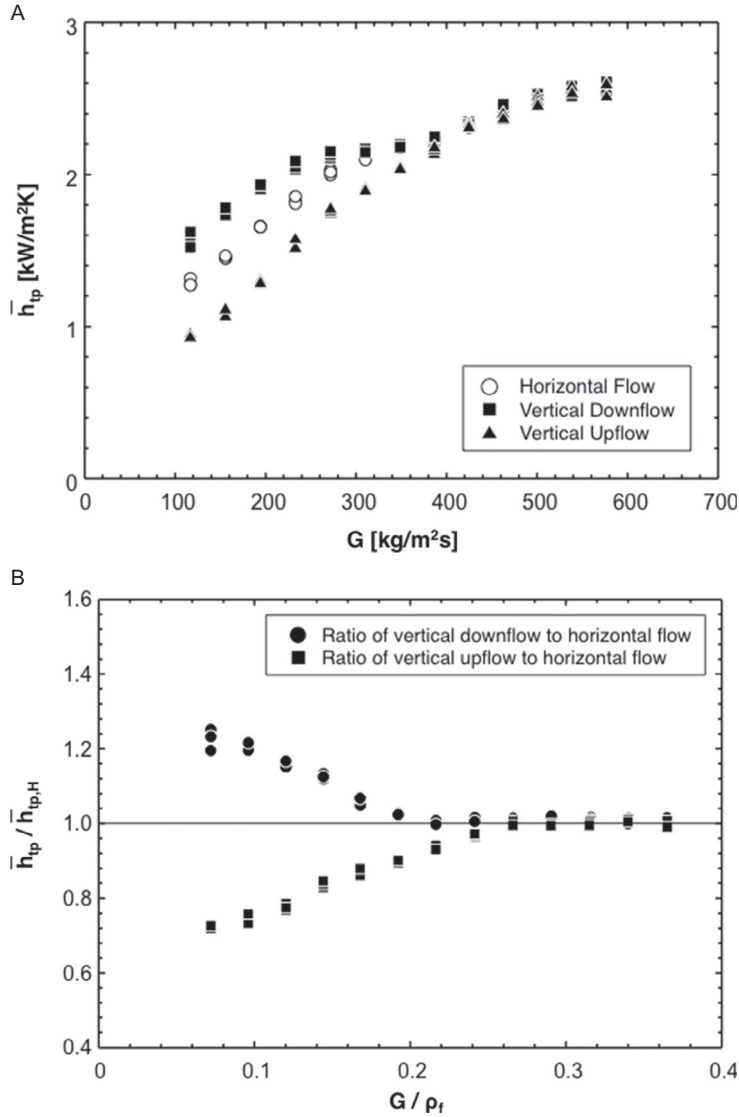

Fig. 22 (A) Comparison of experimentally determined Earth gravity condensation heat transfer coefficients averaged over two-phase region with FC-72 mass velocity for three flow orientations. (B) Variations of heat transfer coefficient averaged over two-phase region with G/ρ_f, with heat transfer coefficients for vertical upflow and vertical downflow normalized relative to those for horizontal flow. *Adapted from L.E. O'Neill, I. Park, C.R. Kharangate, V.S. Devahdhanush, V. Ganesan, I. Mudawar, Assessment of body force effects in flow condensation, part II: criteria for negating influence of gravity, Int. J. Heat Mass Transfer 106 (2017) 313–328.*

body force is reflected in two components, one parallel to or opposite the flow direction, and another perpendicular to the flow direction, negating gravity effects was tackled using two separate criteria. The first criterion addresses vertical downflow and vertical upflow, with gravity acting parallel to and opposite the flow direction, respectively. They developed a force balance on the liquid film for the case of vertical upflow corresponding to the *onset of flooding*, where the film is nearly stationary. This criterion was based on the Froude number, *Fr*, and vapor core Reynolds number, Re_c, which were defined, respectively, as

$$Fr = \frac{\rho_g \left(\overline{u}_g - u_i\right)^2}{\rho_f \, g \sin\theta D_F} \tag{17}$$

and

$$Re_c = \frac{\rho_g \left(\overline{u}_g - u_i\right)\left(D_H - 2\delta\right)}{\mu_g}, \tag{18}$$

where

$$D_F = \frac{D_H^2 - \left(D_H - 2\delta\right)^2}{\left(D_H - 2\delta\right)}, \tag{19}$$

and $\overline{u}_g$, u_i, and δ are, respectively, the mean vapor core velocity, film's interfacial velocity, and film thickness (all three are obtained using an annular flow control-volume-based model), D_H is the hydraulic diameter, and θ the orientation angle. The parallel flow gravity negation criterion was presented as

$$|Fr| > \frac{0.235}{aRe_c^{\,n}}, \tag{20}$$

where $a = 16$ and $n = -1$ for $0 < Re_c < 2000$, $a = 0.079$ and $n = -0.25$ for $2000 < Re_c < 20{,}000$, and $a = 0.046$ and $n = -0.20$ for $Re_c > 20{,}000$.

Unlike the component of body force parallel to or opposite the flow direction, which influences both film thickness and film velocity, the component of body force acting perpendicular to the interface influences mostly circumferential uniformity of the film thickness, especially for horizontal and near-horizontal orientations. For horizontal flow condensation at low mass velocities, weak inertia exasperates the influence of gravity, causing the liquid to pool at the bottom of the channel. On the other hand, the film

becomes more uniform at high mass velocities as increased interfacial vapor shear coupled with surface tension acts to support a liquid layer above the vapor core. O'Neill *et al.* employed classic instability theory [138,139] to develop a mechanistic criterion capable of determining the flow conditions at which horizontal flow condensation is able to establish circumferentially uniform annular flow. Using a relation for critical interfacial wavelength, λ_c, similar to that employed in the Interfacial Lift-off CHF Model, Eq. (1), they concluded that the flow becomes independent of gravity when the gravity term in the λ_c relation approaches zero. The second criterion was presented in terms of the Bond number, *Bo*, and Weber number, *We*,

$$\frac{|Bo|}{We^2} < 5.12 \times 10^{-5}, \tag{21}$$

where

$$Bo = \frac{\left(\rho_f - \rho_g\right) g \cos\theta L_{char}^2}{\sigma}, \tag{22}$$

$$We = \frac{\left(\rho_f'' \rho_g''\right)\left(\overline{u}_g - \overline{u}_f\right)^2 L_{char}}{\left(\rho_f'' + \rho_g''\right)\sigma}, \tag{23}$$

and $\overline{u}_g$, $\overline{u}_f$, and L_{char} are, respectively, the mean vapor velocity, mean liquid velocity, and characteristic length; the latter cancels out in the second criterion.

Fig. 23A–C shows the FC-72 mass velocity required to ensure gravity independence vs local acceleration for exit qualities of $x_{e,out} = 0.5$, 0.15, and 0.85,respectively, and a constant outlet pressure of 130 kPa based on the above two criteria. Fig. 23A shows that, for the intermediate exit quality of $x_{e,out} = 0.5$, gravity independence is governed by the component of body force perpendicular to the flow direction (instability criterion) for accelerations ranging from 0 to about 20 m/s^2, which encompasses Lunar, Martian, and Earth gravities. Above 20 m/s^2, gravity independence is dictated by the component of body force parallel to the flow direction. For a lower exit quality of $x_{e,out} = 0.15$ (indicating a higher percentage of the vapor mass is converted to liquid along the condensation length), Fig. 23B shows that gravity independence is dictated by the component of body force parallel to the flow direction (flooding criterion) over a much broader range of accelerations, including Lunar, Martian, and Earth gravities, compared to $x_{e,out} = 0.5$ (Fig. 23A). This trend can be explained by the strong dependence

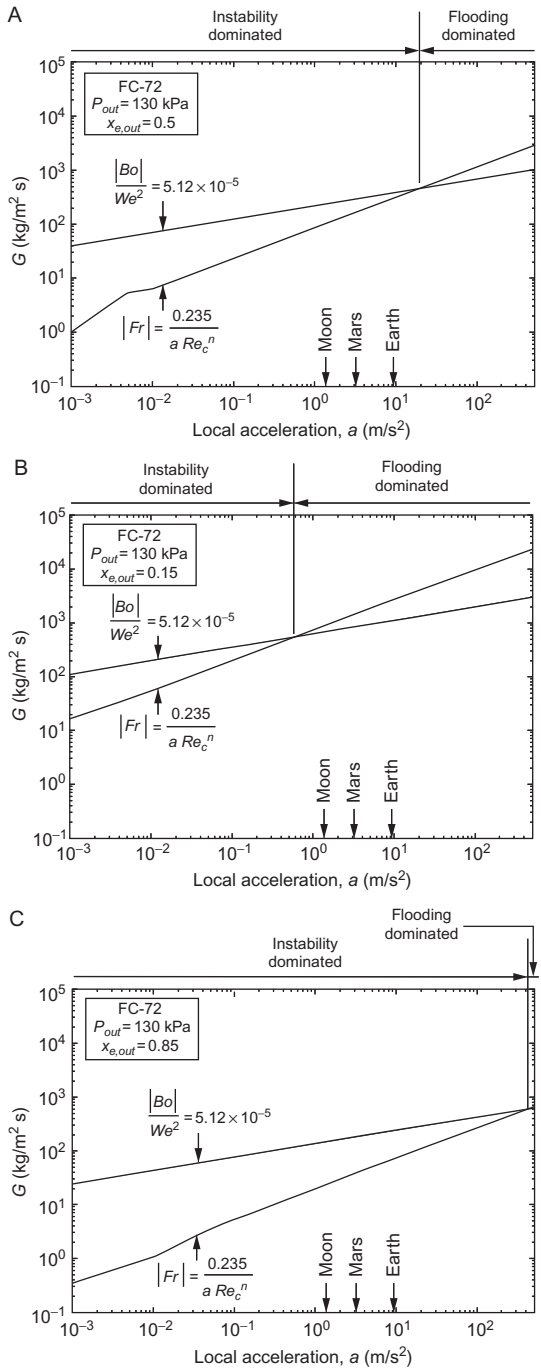

Fig. 23 Mass velocity required to achieve gravity independence vs local acceleration for (A) $x_{e,out} = 0.5$, (B) $x_{e,out} = 0.15$, and (C) $x_{e,out} = 0.85$. *Adapted from L.E. O'Neill, I. Park, C.R. Kharangate, V.S. Devahdhanush, V. Ganesan, I. Mudawar, Assessment of body force effects in flow condensation, part II: Criteria for negating influence of gravity, Int. J. Heat Mass Transfer 106 (2017) 313–328.*

of flooding on liquid mass. Conversely, Fig. 23C shows, for a relatively high exit quality of $x_{e,out} = 0.85$ (indicating a lower percentage of the vapor mass is converted to liquid along the condensation length), that gravity independence is governed by the component of body force perpendicular to the interface (instability criterion) for most gravities of interest, while the component of body force parallel to the flow direction (flooding criterion) becomes the limiting factor only for extremely high accelerations.

3.3 Flow Condensation in Reduced Gravity

3.3.1 Parabolic Flight Hardware

As indicated earlier, a primary objective of this chapter is to discuss findings from NASA's long-term FBCE, which was initiated in 2012 as a collaborative effort between the PU-BTPFL and NASA-GRC. This joint effort involves initial ground and parabolic flight experiments, and development of an experimental package for insertion into the FIR onboard the ISS in early 2019. The ultimate ISS FBCE will accommodate three separate test modules: the FBM, the CM-HT, and the CM-FV. Following are the descriptions of preliminary designs of the CM-HT and CM-FV that were tested both in parabolic flight and in Earth gravity [140]. Also presented is the layout of the parabolic flight test facility.

The experimental condensation facility used in the parabolic flight experiments was configured to facilitate both heat transfer measurements, using CM-HT, and high-speed video capture of the condensing film, using CM-FV. CM-HT was designed for acquisition of heat transfer data for FC-72 along a metallic tube that was cooled by a counterflow of water through an annulus between the tube and an external channel. This simple configuration of condensation along a circular tube was intended as an ideal geometry for comparison with predictions of theoretical or computational condensation models. However, this design precludes optical access to the condensing film. Therefore, CM-VT was designed to capture the film's behavior by flowing FC-72 through the annulus in a transparent outer channel, with the water flowing in the opposite direction through an inner metallic tube.

Fig. 24A shows the condensation parabolic flight facility consists of three separate parts: a main FC-72 condensation rig, a water conditioning rig, and a deaeration rig; the latter is used only prior to the parabolic flight. Fig. 24B shows a CAD diagram of the condensation rig, which includes components of the FC-72 subloop, both the CM-HT and CM-FV, and all controls, video cameras, lighting, and data acquisition hardware. Fig. 24C shows a

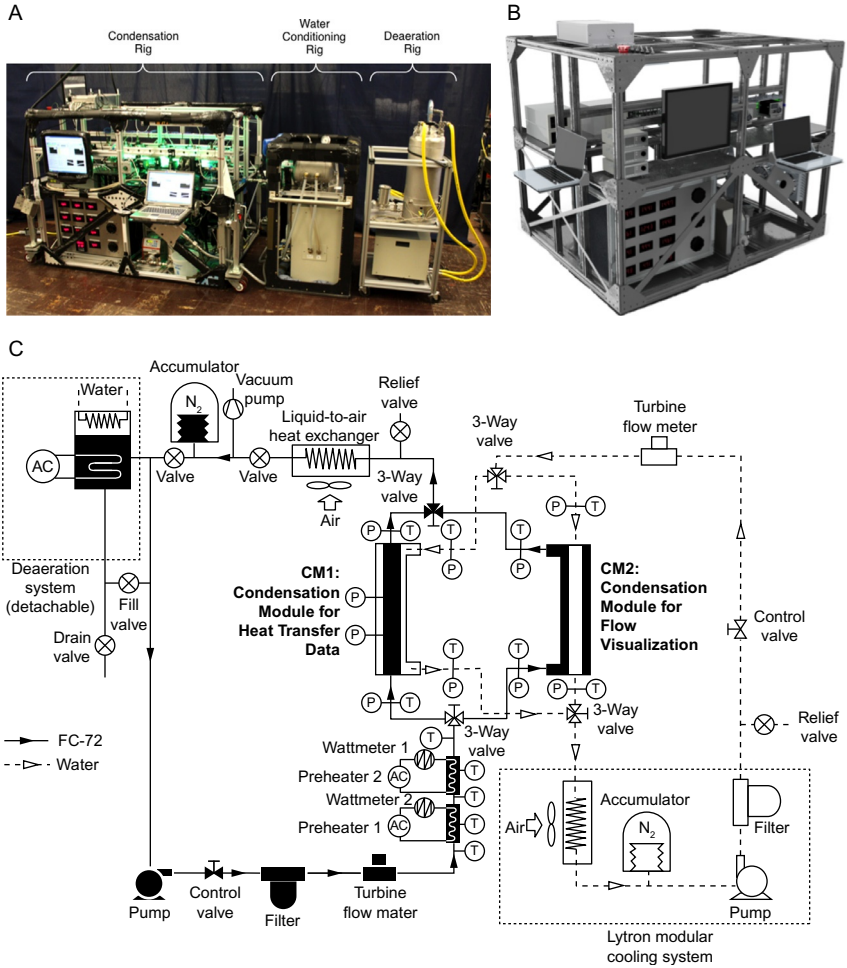

Fig. 24 (A) Photo of flow condensation parabolic flight facility. (B) CAD diagram of condensation rig. (C) Schematic of flow loop.

schematic diagram of the flow loop. The FC-72 is circulated with the aid of a gear pump, followed by a flow control valve, filter, and flow meter. The FC-72 liquid is then brought to the desired quality using two inline electrical preheaters before entering either the CM-HT or the CM-FV. The two-phase FC-72 mixture exiting the test module is passed through a liquid-to-air heat exchanger, which returns the mixture to liquid state. The FC-72 subloop also contains an accumulator containing metallic bellows to accommodate thermal expansion or contraction of the fluid and helps maintain desired system pressure. The primary purpose of the water subloop

is to reject the heat from the FC-72 vapor. The water is supplied to either the CM-HT or the CM-FV using a cooling system containing a reservoir pump, fan-cooled heat exchanger, accumulator, and a turbine flow meter.

Fig. 25A shows a photo of the CM-HT mounted within the condensation rig. Fig. 25B shows an exploded CAD diagram illustrating the module

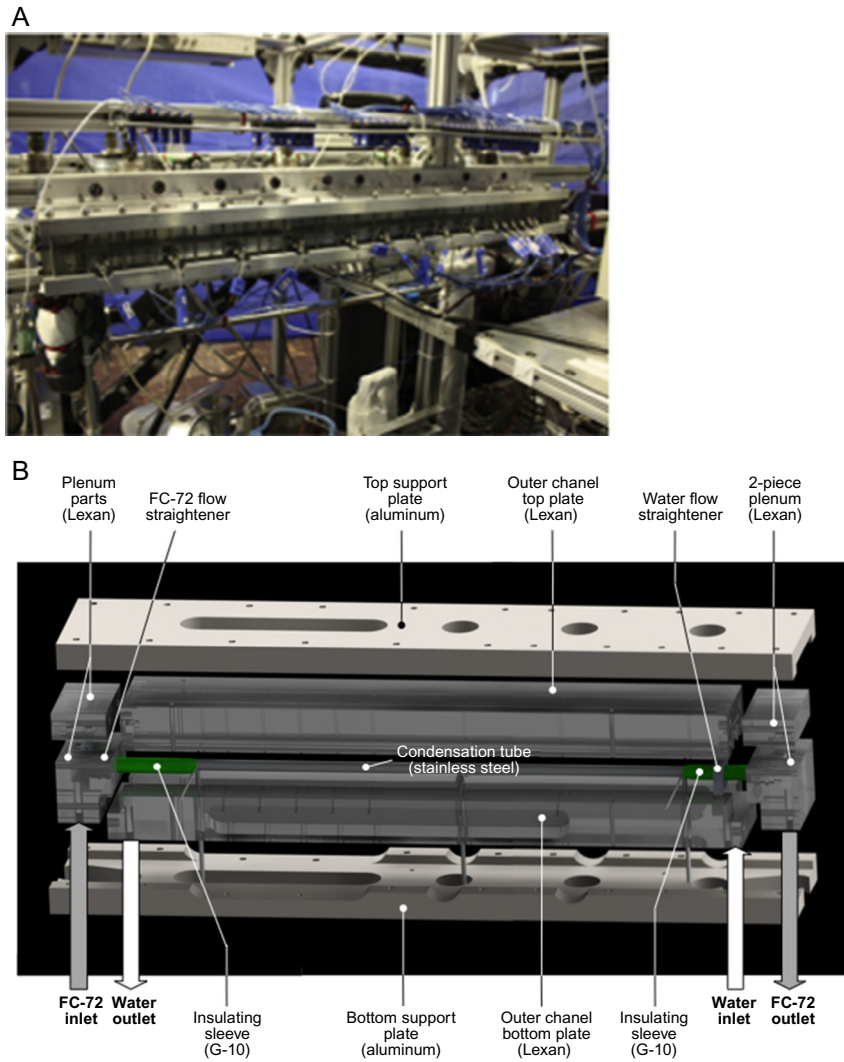

Fig. 25 Construction of condensation module CM-HT for heat transfer measurements in parabolic flight rig: (A) photo of module, (B) CAD model, (C) cross-sectional diagram, and (D) longitudinal sectional diagram.

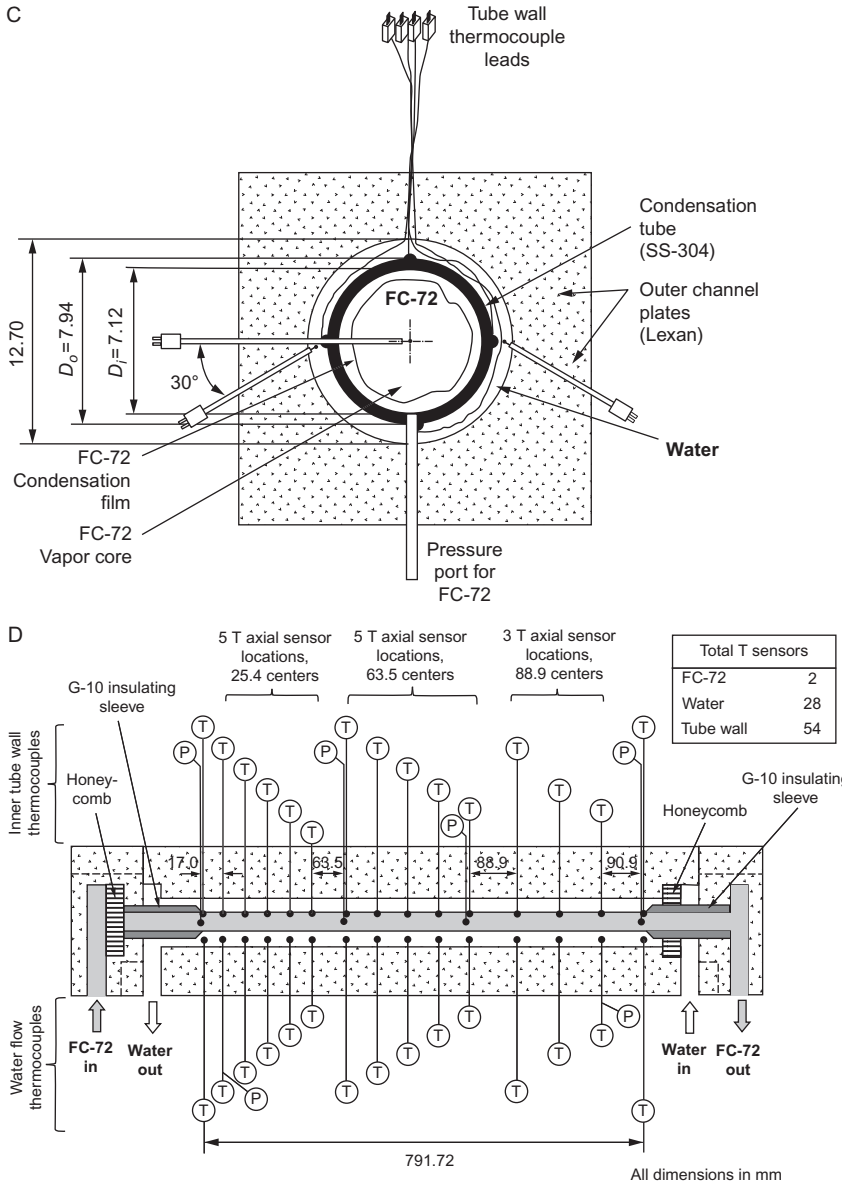

Fig. 25—Cont'd

assembly. As shown in Fig. 25C, this module is designed to facilitate FC-72 vapor flow through a central stainless steel tube having a 7.12-mm i.d. and 0.41-mm wall thickness, with the water flowing in the opposite direction through an annulus having a diameter of 12.70 mm. Fig. 25D shows that

the FC-72 vapor is introduced from the left inlet and the water from the right. The central tube is fitted on both ends with short insulating sleeves; the effective condensation length between the two sleeves is 791.72 mm. The CM-HT is fitted with a large array of thermocouples that are inserted in the inlets and outlets of both fluids, as well as along the stainless tube wall and in the water flow at 15 axial locations. Pressures in the CM-HT are measured at four axial locations for FC-72 and two for water.

As mentioned earlier, the primary difference in the design of the CM-HT compared to the CM-FV is FC-72 flow through the annulus and water within the inner tube for the latter. Fig. 26A shows a photo of the CM-FV mounted within the condensation rig. Fig. 26B shows an exploded CAD diagram illustrating the module assembly. Fig. 26C shows that the inner water tube of the CM-FV has a 5.99-mm o.d., while the outer square FC-72 annulus is 12.2-mm wide. Use of flat, transparent outer walls is intended to facilitate undistorted optical access to the FC-72 film. Fig. 26D shows locations of temperature and pressure measurements in the CM-FV. The effective condensation length of the CM-FV is 777.24 mm. Three video cameras are used to capture the FC-72 condensate film in the inlet, middle, and outlet of the condensation length in the CM-FV.

3.3.2 Interfacial Behavior of Annular Condensation Film in Microgravity

Fig. 27 compares video images of the condensation film in microgravity, Lunar gravity (0.17 g_e), and Martian gravity (0.377 g_e) captured using the CM-VF in the inlet region for two sets of operating conditions. At the lower FC-72 mass velocity, the film in microgravity appears smooth laminar, with waves commencing toward the downstream edge of the image. For about the same FC-72 mass velocity, the film in Lunar and Martian gravities also appears wavy laminar but with thinning above the tube and thickening beneath; the film's asymmetry is more pronounced in the Martian gravity. It is important to note that the asymmetry under Lunar and Martian gravities is associated with appreciable circumferential variations in the condensation heat flux.

At the higher FC-72 mass velocity, Fig. 27 shows that the film becomes visibly turbulent and very wavy for all three gravities. Even more important is the lack of asymmetry in the Lunar and Martian gravities. This behavior may be explained by the appreciable increase in vapor shear at high FC-72 mass velocities rendering inconsequential any body force effects. This fact has an important practical implication to space missions involving gravity variations: it is possible to negate the influence of gravity altogether by a sufficient increase in the flow rate.

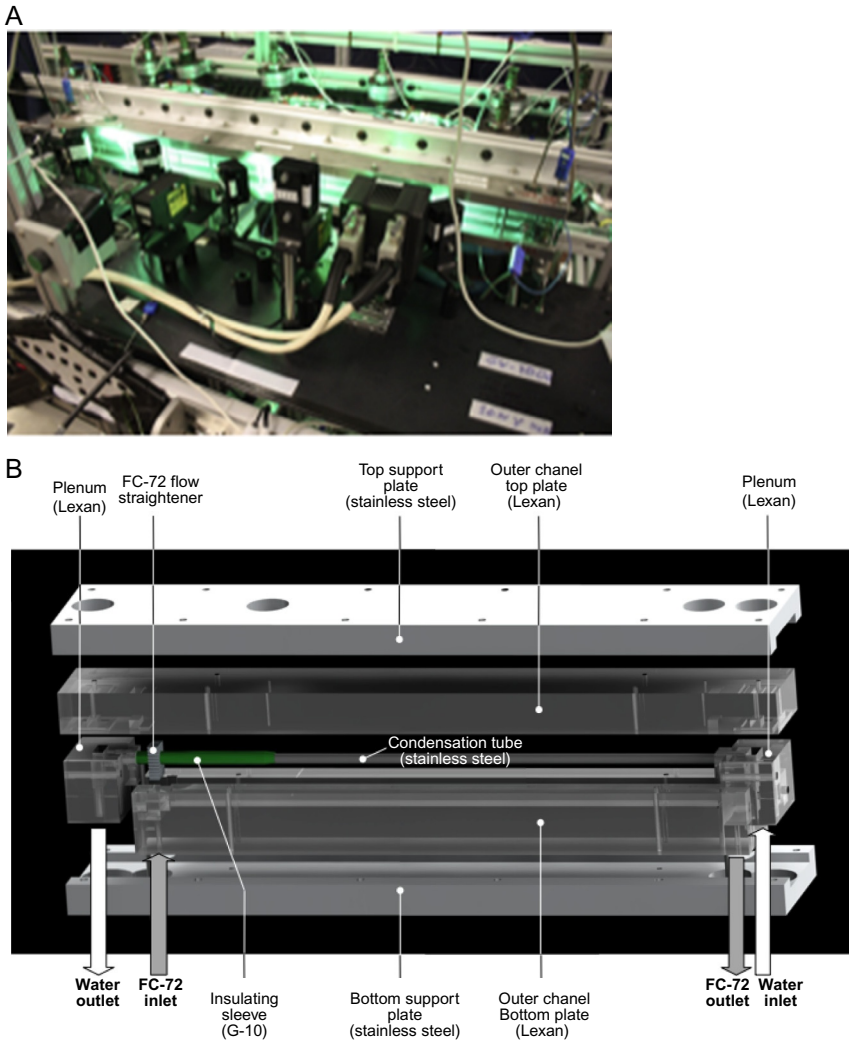

Fig. 26 Construction of condensation module CM-FV for flow visualization in a parabolic flight rig: (A) photo of module, (B) CAD model, (C) cross-sectional diagram, and (D) longitudinal sectional diagram.

3.3.3 Condensation Heat Transfer Microgravity Data

Fig. 28 shows variations of the local condensation heat transfer coefficient, $h(z)$, along the condensation length determined from temperature measurements using the CM-HT for four FC-72 mass velocities and a narrow ranges

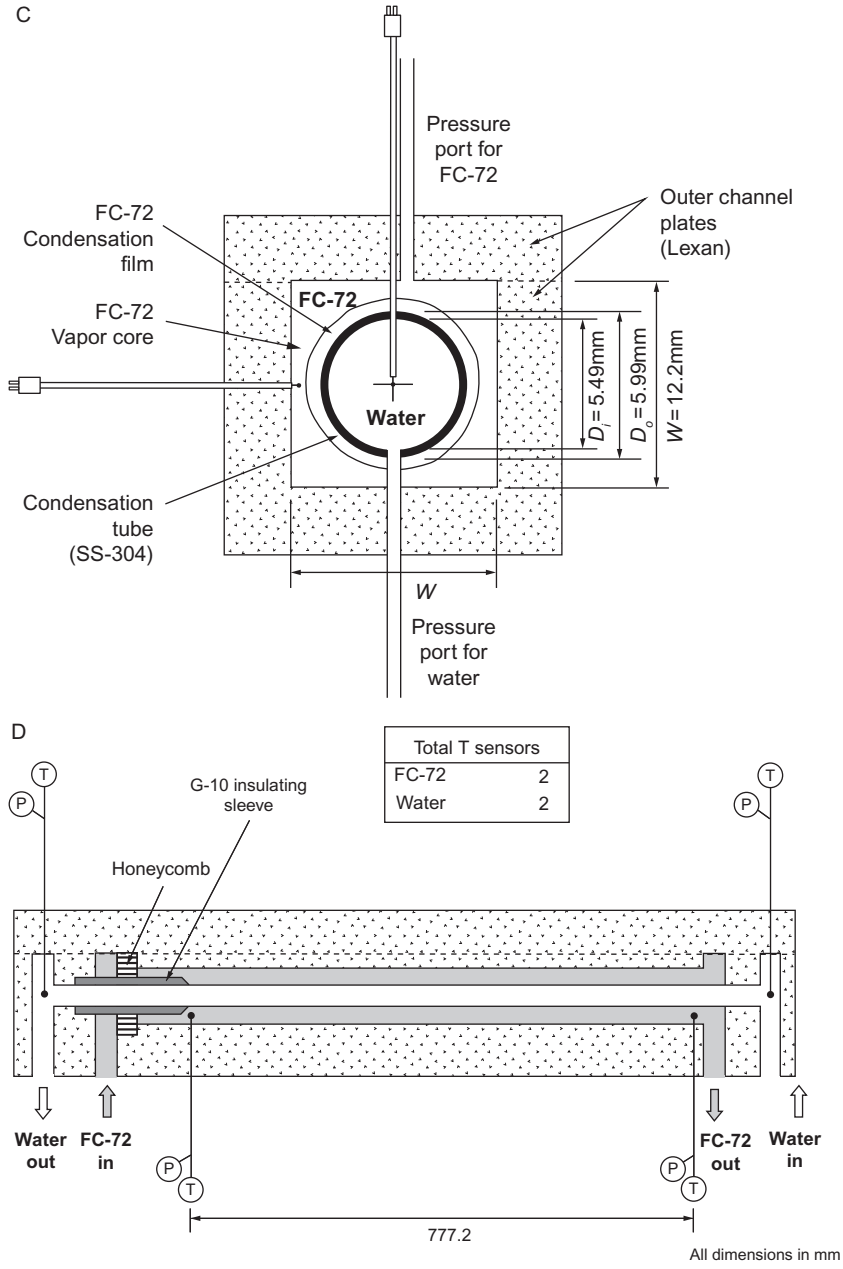
C
Pressure port for FC-72
Outer channel plates (Lexan)
FC-72 Condensation film
FC-72 Vapor core
FC-72
Water
D_i = 5.49mm
D_o = 5.99mm
W = 12.2mm
Condensation tube (SS-304)
W
Pressure port for water
D
Total T sensors
FC-72 2
Water 2
G-10 insulating sleeve
Honeycomb
Water out
FC-72 in
FC-72 out
Water in
777.2
All dimensions in mm

Fig. 26—Cont'd

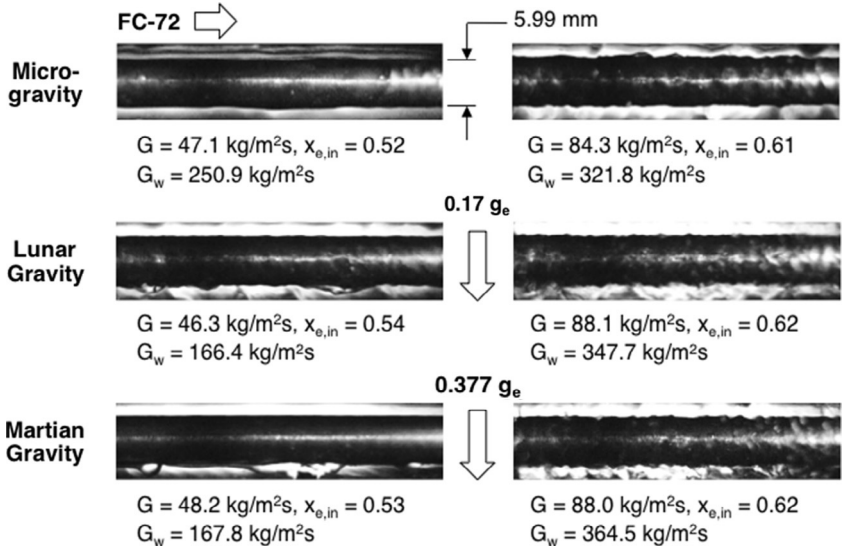

Fig. 27 Comparison of images of condensation film in microgravity, Lunar gravity, and Martian gravity for two sets of operating conditions. The images are centered at 5.8 cm from the inlet of condensation length. *Adapted from H. Lee, I. Mudawar, M.M. Hasan, Experimental and theoretical investigation of annular flow condensation in microgravity, Int. J. Heat Mass Transfer 61 (2013) 293–309.*

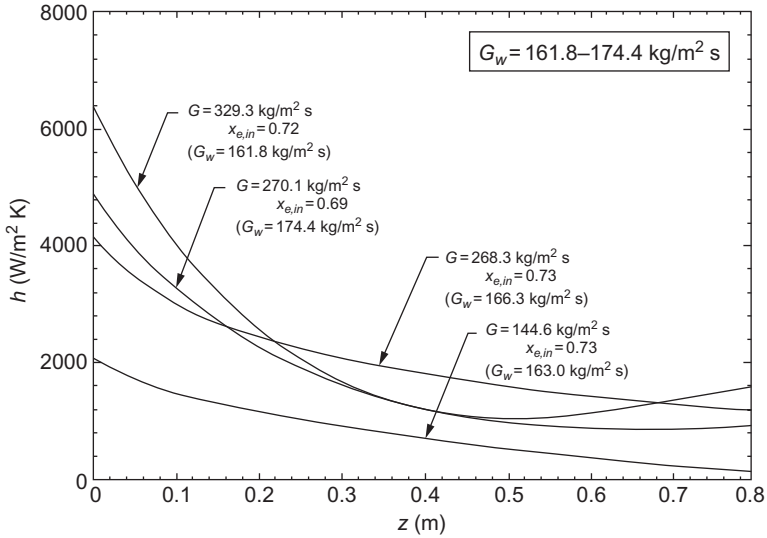

Fig. 28 Variations of experimentally-determined condensation heat transfer coefficient with axial distance in microgravity for different FC-72 mass velocities at water mass velocities of $G_w = 161.8–174.4$ kg/m^2 s. *Adapted from H. Lee, I. Mudawar, M.M. Hasan, Experimental and theoretical investigation of annular flow condensation in microgravity, Int. J. Heat Mass Transfer 61 (2013) 293–309.*

of water mass velocities of $G_w = 161.8–174.4$ kg/m^{2}s and inlet qualities of $x_{e,in} = 0.69–0.73$. Increasing the FC-72 mass velocity is shown generally enhancing condensation heat transfer, which is the result of film thinning brought about by higher vapor shear. For all FC-72 mass velocities, the heat transfer coefficient is highest at the inlet and, because of the axially increasing thickness, decreases along the condensation length. While this trend is monotonic for the three lower G values, presumably because of the relatively stronger dependence of heat transfer on conduction across the film, $h(z)$ for the highest FC-72 mass velocity of $G = 329.3$ kg/m^{2}s acquires a minimum around the middle of the condensation length before increasing again downstream. The downstream increase can be explained by increased turbulence intensity coupled with increased interfacial waviness.

3.3.4 Theoretical Model for Annular Flow Condensation in Microgravity

Recently, Kim and Mudawar [104] constructed a control volume model for annular flow condensation, which was also adopted by Lee *et al.* [140] for microgravity conditions. The model is based on the assumptions that the flow is annular and steady, and pressure is uniform across the flow area. Additionally, both the film thickness and the heat transfer coefficient are assumed circumferentially uniform.

The model involves discretizing the condensation length into small axial elements of length Δz, and applying mass, momentum, and energy conservation to control volumes encompassing the annular film and vapor core separately. Fig. 29A shows momentum and force interactions for the liquid film's control volume, the former neglecting the film's axial momentum changes. Combined with film's mass transfer rate, these control volumes are used to derive an expression for velocity profile across the film, $u_f(y)$, from which the interfacial velocity, u_i, is determined by setting $y = \delta$. The relations for $u_f(y)$ and u_i are then used to derive a relation for pressure gradient across the film. Determining the pressure gradient requires an expression for the interfacial shear stress, τ_i, using momentum conservation for the vapor core as shown in Fig. 29B. The interfacial shear stress accounts for both interfacial friction, according to Shah and London [141], and interfacial mass transfer, as proposed by Wallis [54].

The local heat flux across the liquid film is given by

$$q'' = -k_f \left[1 + \frac{Pr_f}{Pr_{f,T}} \frac{\varepsilon_m}{\nu_f}\right] \frac{dT}{dy}, \tag{24}$$

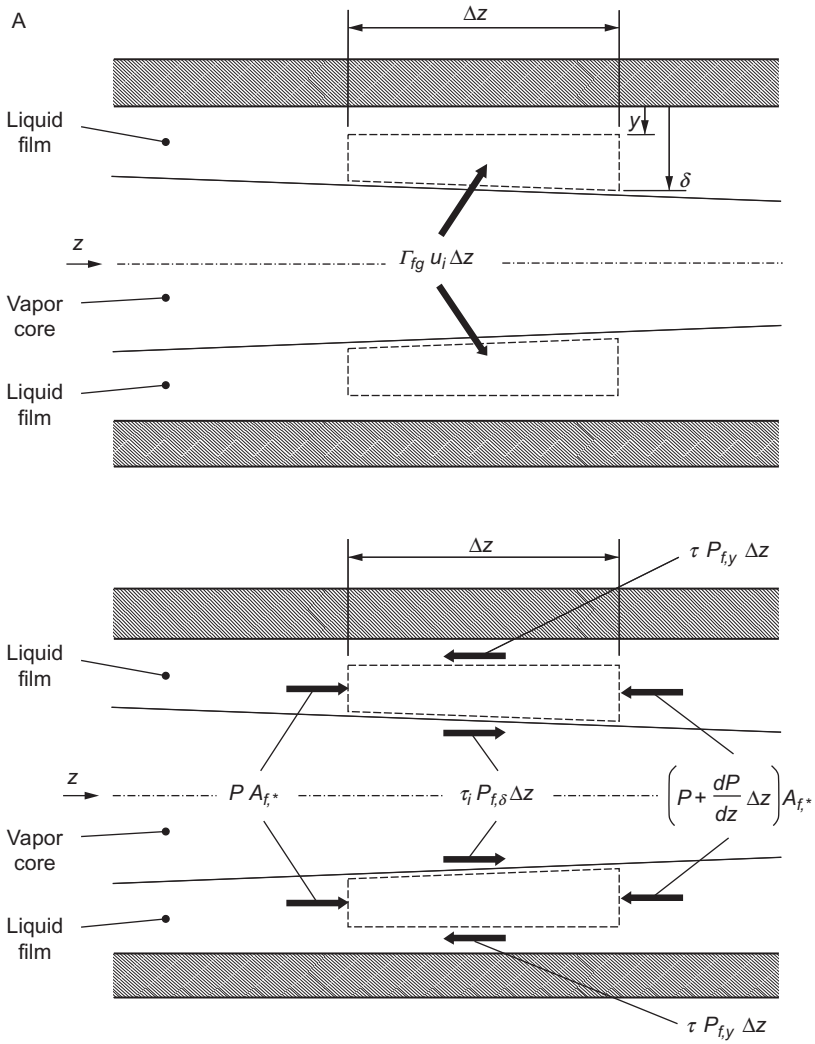

Fig. 29 Momentum and force interactions for condensation in microgravity for (A) liquid film and (B) vapor core control volumes. *Adapted from S.M. Kim, I. Mudawar, Theoretical model for annular flow condensation in rectangular micro-channels, Int. J. Heat Mass Transfer 55 (2012) 958–970.*

where $Pr_{f,T}$ is the turbulent Prandtl number, and ε_m the liquid film's eddy momentum diffusivity. The local condensation heat transfer coefficient is determined by integrating Eq. (24) between the interface, where $T = T_{sat}$, and the wall, where $T = T_w$,

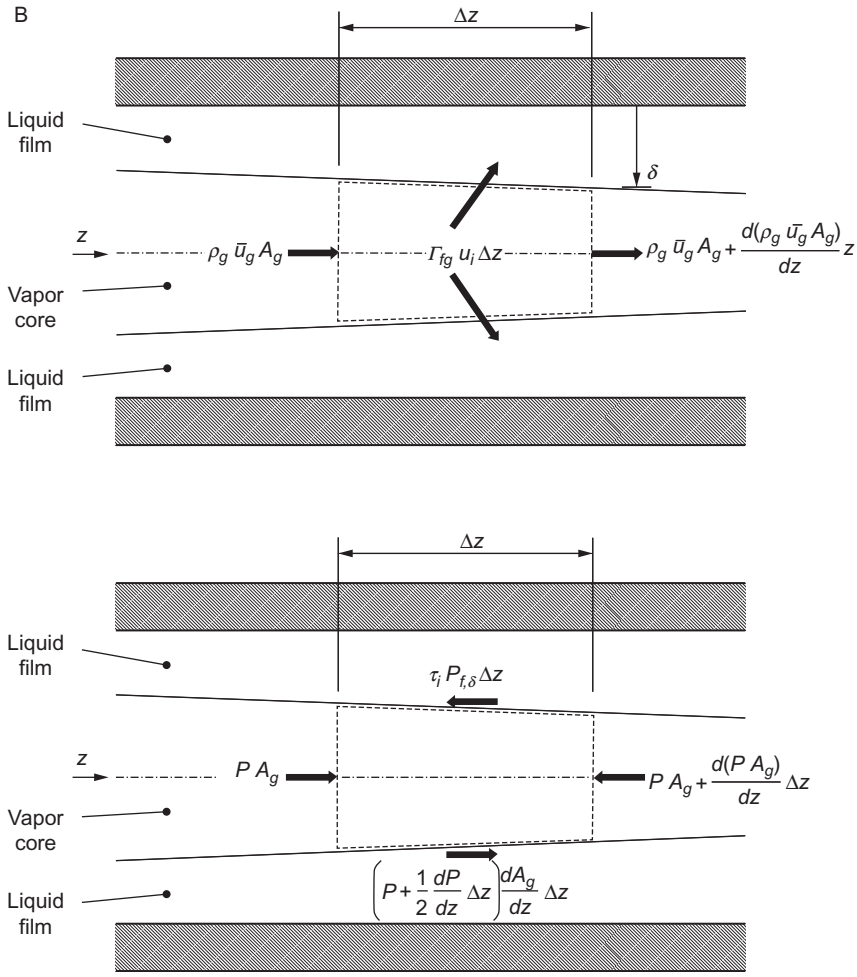

Fig. 29—Cont'd

$$h = \frac{-q''}{T_{sat} - T_w} = \frac{\delta / k_f}{\left[\int_0^1 \left(1 + \frac{Pr_f}{Pr_{f,T}} \frac{\varepsilon_m}{\nu_f}\right)^{-1} d\left(\frac{\gamma}{\delta}\right)\right]}. \quad (25)$$

The liquid film's eddy momentum diffusivity, ε_m, is determined using a turbulent mixing length relation originally proposed by Van Driest [142] and later modified by Kays [143,144]. Kim and Mudawar [104] proposed the following relation for ε_m that also accounts for interfacial damping of turbulent fluctuations due to surface tension,

$$\frac{\varepsilon_m}{\nu_f} = -\frac{1}{2} + \frac{1}{2}\sqrt{1 + 4K^2 y^{+2}\left[1 - \exp\left(-\sqrt{\frac{\tau}{\tau_w}}\frac{y^+}{A^+}\right)\right]^2 \frac{\tau}{\tau_w}\left(1 - \frac{y^+}{\delta^+}\right)^{0.1}}, \quad (26)$$

where $y^+ = yu^*/\nu_f$, $\delta^+ = \delta u^*/\nu_f$, $u^* = \sqrt{\tau_w/\rho_f}$, $A^+ = 26[1 + 30.18\mu_f\rho_f^{-0.5}\tau_{wall}^{-1.5}(dP/dz)]^{-1}$, and the Von-Karman constant is given by $K = 0.4$. The turbulent Prandtl number is obtained from a relation derived earlier by Mudawar and El-Masri [109],

$$Pr_{f,T} = 1.4\exp\left(-15\frac{y^+}{\delta^+}\right) + 0.66. \quad (27)$$

Fig. 30 shows the variation of eddy momentum diffusivity for condensation of FC-72 along a $1 \times 1\ mm^2$ channel at $G = 367\ kg/m^2s$ [104]. Notice how, without the turbulence damping term, the eddy diffusivity increases monotonically with distance from the wall, while, with the damping term, the eddy diffusivity is reduced to zero at the film interface because of surface tension effects.

Fig. 31A–D compares axial variations of the condensation heat transfer coefficient obtained from parabolic flight experiments with the model

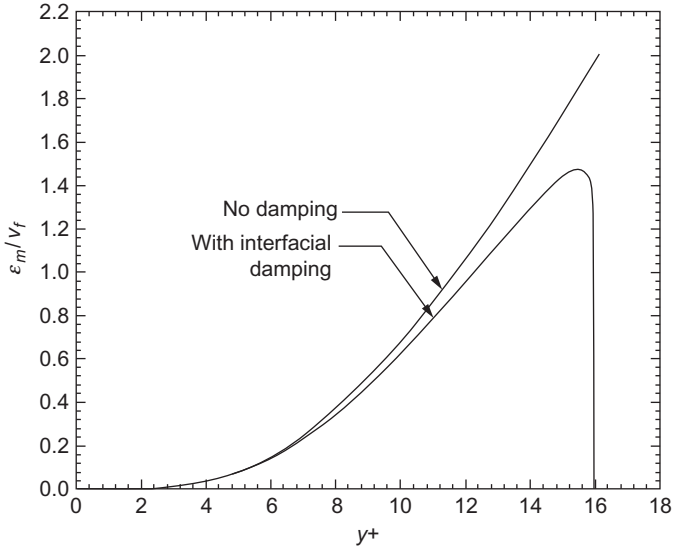

Fig. 30 Effects of interfacial damping term on eddy momentum diffusivity for condensation of FC-72 along a $1 \times 1\ mm^2$ channel at $G = 367\ kg/m^2s$. *Adapted from S.M. Kim, I. Mudawar, Theoretical model for annular flow condensation in rectangular microchannels, Int. J. Heat Mass Transfer 55 (2012) 958–970.*

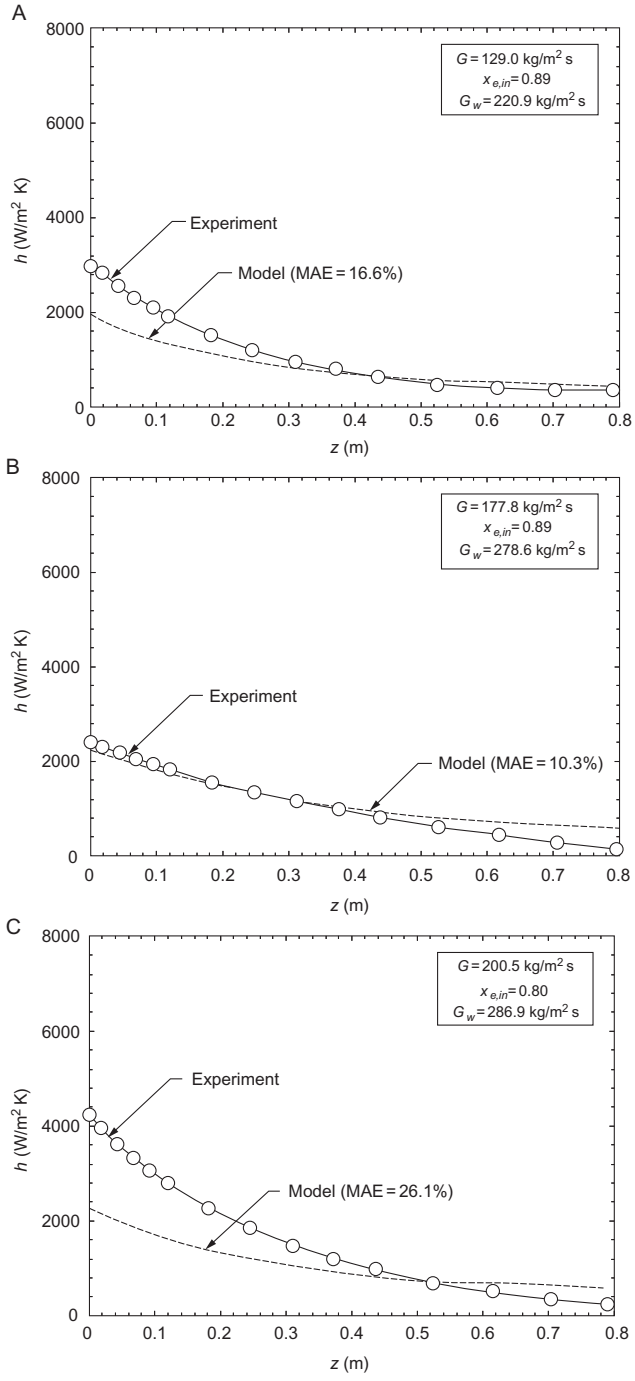

Fig. 31 See figure legend on next page.

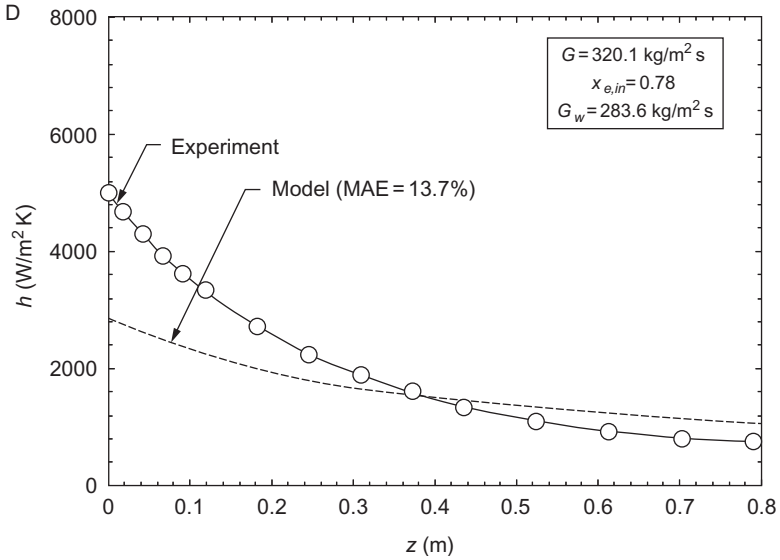

Fig. 31—Cont'd Comparison of experimentally determined axial variations of microgravity condensation heat transfer coefficient with control volume model predictions for (A) $G=$ 129.0 kg/m^2 s, $x_{e,in}=0.89$, and $G_w=220.9$ kg/m^2 s; (B) $G=177.8$ kg/m^2 s, $x_{e,in}=0.89$, and $G_w=278.6$ kg/m^2 s; (C) $G=200.5$ kg/m^2 s, $x_{e,in}=0.80$, and $G_w=286.9$ kg/m^2 s; and (D) $G=320.1$ kg/m^2 s, $x_{e,in}=0.78$, and $G_w=283.6$ kg/m^2 s. *Adapted from H. Lee, I. Mudawar, M.M. Hasan, Experimental and theoretical investigation of annular flow condensation in microgravity, Int. J. Heat Mass Transfer 61 (2013) 293–309.*

predictions for four different sets of operating conditions. The model correctly predicts the axially decreasing heat transfer coefficient with mean absolute errors ranging from 10.3% to 26.1%. Much of the error is concentrated in the upstream region, especially for high FC-72 mass velocities. This error is attributed to inlet quality values below unity, implying that some of the liquid at the inlet may have shattered away from the condensation tube. The shattered liquid decreases the inlet flow rate of the liquid film, which in turn decreases the film thickness and increases the heat transfer coefficient measured in the inlet region.

4. CONCLUDING REMARKS

This chapter reviewed published literature concerning reduced gravity flow boiling and flow condensation mechanisms and predictive tools that are crucial to the design of future space vehicles. Other topics that were

addressed include adiabatic two-phase flow, pool boiling, and flow boiling pressure drop. Key findings from the review are as follows:

(1) Different testing platforms have been used in past studies to explore the influence of reduced gravity on two-phase flow and heat transfer, including mostly drop tower and drop shaft, sounding rocket, and parabolic flight experiments. However, these experiments have failed to yield reliable, long-duration, steady state data, and flow visualization records for microgravity flow boiling and flow condensation.

(2) Much of the available technical knowhow concerning gravity effects comes from two-phase flow and heat transfer experiments conducted at different flow orientations in Earth gravity to produce a partial component of gravity perpendicular to the heated or cooled wall. Despite their important contribution to fundamental understanding of gravity effects, these experiments fail to simulate precise reduced gravity conditions because of the inability to eliminate the influence of gravity component parallel to or opposite the flow direction.

(3) Despite several decades of emphasis on pool boiling in previous microgravity experiments, there is now a realization that pool boiling is not a viable candidate for thermal management in space applications, given the unusually large bubble size and low CHF compared to pool boiling in Earth gravity. It is also doubtful that fundamental knowledge gained from these pool-boiling experiments will aid in the development of useful predictive tools for flow boiling in microgravity.

(4) For flow boiling, key topics of importance to space vehicle design are two-phase flow patterns, pressure drop, heat transfer coefficient, and CHF. And key topics for flow condensation are flow patterns, pressure drop, and heat transfer coefficient. Other important design tools for both flow boiling and flow condensation are criteria for minimum flow rate required to achieve gravity-independent performance. While recent parabolic flight experiments have culminated in useful mechanistic understanding for both, developing reliable design tools will require acquisition of long duration, steady-state heat transfer measurements, and video records onboard the ISS. This chapter provided initial findings from the Purdue-NASA FBCE, and plans for insertion into the ISS to achieve these important goals.

ACKNOWLEDGMENT

The author is grateful for the support of the National Aeronautics and Space Administration (NASA) under Grant NNX13AB01G.

REFERENCES

[1] G.B. Ganapathi, G. Birur, G. Tsuyuki, R. Krylo, Mars Exploration Rover heat rejection system performance—comparison of ground and flight data, SAE Paper 2004-01-2413, 2004.

[2] G.B. Ganapathi, G. Birur, E. Sunada, J. Miller, Two phase vs. single phase thermal loop trades for exploration mission LAT II architecture, SAE Paper 2008-01-1958, 2008.

[3] F.P. Chiaramonte, J.A. Joshi, Workshop on critical issues in microgravity fluids, transport, and reaction processes in advanced human support technology—final report, NASA Report TM-2004-212940, Washington, DC, 2004.

[4] S. Lee, I. Mudawar, M.M. Hasan, Thermal analysis of hybrid single-phase, two-phase and heat pump thermal control system (TCS) for future spacecraft, Appl. Therm. Eng. 100 (2016) 190–214.

[5] National Research Council, Recapturing a Future for Space Exploration: Life and Physical Sciences Research for a New Era, The National Academies Press, Washington, DC, 2011.

[6] C. Konishi, I. Mudawar, M.M. Hasan, Investigation of the influence of orientation on critical heat flux for flow boiling with two-phase inlet, Int. J. Heat Mass Transfer 61 (2013) 176–190.

[7] European Space Agency (ESA), European users guide to low gravity platforms, UIC-ESA-UM-0001, Issue 2, Noordwijk, The Netherlands, 2005.

[8] N.J. Penley, C.P. Schafer, J.D.F. Bartoe, The international space station as a microgravity research platform, Acta Astronaut. 50 (2002) 691–696.

[9] I. Mudawar, Assessment of high-heat-flux thermal management schemes, IEEE Trans. Compon. Packag. Technol. 24 (2001) 122–141.

[10] I. Mudawar, Two-phase micro-channel heat sinks: theory, applications and limitations, J. Electron. Packag. 133 (2011) 041002.

[11] I. Mudawar, Recent advances in high-flux, two-phase thermal management, J. Therm. Sci. Eng. Appl. 5 (2013). 021012.

[12] P.J. Marto, V.J. Lepere, Pool boiling heat transfer from enhanced surfaces to dielectric fluids, J. Heat Transfer 104 (1982) 292–299.

[13] I. Mudawar, T.M. Anderson, Parametric investigation into the effects of pressure, subcooling, surface augmentation and choice of coolant on pool boiling in the design of cooling systems for high-power density chips, J. Electron. Packag. 112 (1990) 375–382.

[14] T.J. LaClair, I. Mudawar, Thermal transients in a capillary evaporator prior to the initiation of boiling, Int. J. Heat Mass Transfer 43 (2000) 3937–3952.

[15] I. Mudawar, R.A. Houpt, Mass and momentum transport in smooth falling liquid films laminarized at relatively high Reynolds numbers, Int. J. Heat Mass Transfer 36 (1993) 3437–3448.

[16] D.E. Maddox, I. Mudawar, Single- and two-phase convective heat transfer from smooth and enhanced microelectronic heat sources in a rectangular channel, J. Heat Transfer 111 (1989) 1045–1052.

[17] S. Mukherjee, I. Mudawar, Smart pumpless loop for micro-channel electronic cooling using flat and enhanced surfaces, IEEE Trans. Compon. Packag. Technol. 26 (2003) 99–109.

[18] J. Lee, I. Mudawar, Fluid flow and heat transfer characteristics of low temperature two-phase micro-channel heat sinks—part 1: experimental methods and flow visualization results, Int. J. Heat Mass Transfer 51 (2008) 4315–4326.

[19] J. Lee, I. Mudawar, Critical heat flux for subcooled flow boiling in micro-channel heat sinks, Int. J. Heat Mass Transfer 52 (2009) 3341–3352.

[20] M. Monde, T. Inoue, Critical heat flux in saturated forced convective boiling on a heated disk with multiple impinging jets, J. Heat Transfer 113 (1991) 722–727.
[21] D.C. Wadsworth, I. Mudawar, Enhancement of single-phase heat transfer and critical heat flux from an ultra-high-flux simulated microelectronic heat source to a rectangular impinging jet of dielectric liquid, J. Heat Transfer 114 (1992) 764–768.
[22] M.E. Johns, I. Mudawar, An ultra-high power two-phase jet-impingement avionic clamshell module, J. Electron. Packag. 118 (1996) 264–270.
[23] L. Lin, R. Ponnappan, Heat transfer characteristics of spray cooling in a closed loop, Int. J. Heat Mass Transfer 46 (2003) 3737–3746.
[24] M. Visaria, I. Mudawar, Effects of high subcooling on two-phase spray cooling and critical heat flux, Int. J. Heat Mass Transfer 51 (2008) 5269–5278.
[25] M.K. Sung, I. Mudawar, Experimental and numerical investigation of single-phase heat transfer using a hybrid jet-impingement/micro-channel cooling scheme, Int. J. Heat Mass Transfer 49 (2006) 682–694.
[26] S.S. Kutateladze, A.I. Leont'ev, in: Some applications of the asymptotic theory of the turbulent boundary layer, Proceedings of the Third International Heat Transfer Conference, Chicago, Illinois, vol. 3, 1966, pp. 1–6.
[27] L.S. Tong, Boundary-layer analysis of the flow boiling crisis, Int. J. Heat Mass Transfer 11 (1968) 1208–1211.
[28] W. Hebel, W. Detavernier, M. Decreton, A contribution to the hydrodynamics of boiling crisis in a forced flow of water, Nucl. Eng. Des. 64 (1981) 443–445.
[29] J. Weisman, B.S. Pei, Prediction of critical heat flux in flow boiling at low qualities, Int. J. Heat Mass Transfer 26 (1983) 1463–1477.
[30] C.H. Lee, I. Mudawar, A mechanistic critical heat flux model for subcooled flow boiling based on local bulk flow conditions, Int. J. Multiphase Flow 14 (1988) 711–728.
[31] J.E. Galloway, I. Mudawar, CHF mechanism in flow boiling from a short heated wall—part 1. Examination of near-wall conditions with the aid of photomicrography and high-speed video imaging, Int. J. Heat Mass Transfer 36 (1993) 2511–2526.
[32] J.E. Galloway, I. Mudawar, CHF mechanism in flow boiling from a short heated wall—part 2. Theoretical CHF model, Int. J. Heat Mass Transfer 36 (1993) 2527–2540.
[33] J.C. Sturgis, I. Mudawar, Critical heat flux in a long, rectangular channel subjected to one-sided heating—I. Flow visualization, Int. J. Heat Mass Transfer 42 (1999) 1835–1847.
[34] J.C. Sturgis, I. Mudawar, Critical heat flux in a long, rectangular channel subjected to onesided heating—II. Analysis of critical heat flux data, Int. J. Heat Mass Transfer 42 (1999) 1849–1862.
[35] C.R. Class, J.R. DeHaan, M. Piccone, R.B. Cost, Boiling heat transfer to liquid hydrogen from flat surfaces, in: K.D. Timmerhaus (Ed.), Advances Cryogenic Engineering, vol. 5, Plenum Press, New York, NY, 1960.
[36] P.M. Githinji, R.H. Sabersky, Some effects of orientation of the heating surface in nucleate boiling, J. Heat Transfer 85 (1963) 379.
[37] W.R. Marcus, D. Dropkin, The effect of surface configuration on nucleate boiling heat transfer, Int. J. Heat Mass Transfer 6 (1963) 863–867.
[38] L.T. Chen, Heat transfer to pool-boiling Freon from inclined heating plate, Lett. Heat Mass Transfer 5 (1978) 111–120.
[39] K. Nishikawa, Y. Fujita, S. Uchida, H. Ohta, in: Effect of heating surface orientation on nucleate boiling heat transfer, Proceedings of ASME-JSME Thermal Engineering Joint Conference, Honolulu, HI, vol. 1, 1983, pp. 129–136.
[40] V. Kumar, M. Prasad, M.K. Verma, N.S. Garg, Effect of inclination on pool boiling heat transfer from a flat plate, Indian Chem. Eng. 32 (1990) 61–64.

[41] N. Zuber, M. Tribus, J.W. Westwater, in: The hydrodynamic crisis in pool boiling of saturated and subcooled liquids, Proceedings of the International Heat Transfer Conference, Boulder, CO, 1961, pp. 230–236.
[42] I. Mudawar, A.H. Howard, C.O. Gersey, An analytical model for near-saturated pool boiling CHF on vertical surfaces, Int. J. Heat Mass Transfer 40 (1997) 2327–2339.
[43] A.H. Howard, I. Mudawar, Orientation effects on pool boiling CHF and modeling of CHF for near-vertical surfaces, Int. J. Heat Mass Transfer 42 (1999) 1665–1688.
[44] R.J. Simoneau, F.F. Simon, A visual study of velocity and buoyancy effects on boiling nitrogen, NASA Tech Note TN D-3354, 1966.
[45] K. Mishima, H. Nishihara, The effect of flow direction and magnitude on CHF for low pressure water in thin rectangular channels, Nucl. Eng. Des. 86 (1985) 165–181.
[46] C.O. Gersey, I. Mudawar, Effects of heater length and orientation on the trigger mechanism for near-saturated flow boiling CHF—I. Photographic and statistical characterization of the near-wall interfacial features, Int. J. Heat Mass Transfer 38 (1995) 629–642.
[47] C.O. Gersey, I. Mudawar, Effects of heater length and orientation on the trigger mechanism for near-saturated flow boiling CHF—II. CHF model, Int. J. Heat Mass Transfer 38 (1985) 643–654.
[48] H. Zhang, I. Mudawar, M.M. Hasan, Experimental assessment of the effects of body force, surface tension force, and inertia on flow boiling CHF, Int. J. Heat Mass Transfer 45 (2002) 4079–4095.
[49] H. Zhang, I. Mudawar, M.M. Hasan, Experimental and theoretical study of orientation effects on flow boiling CHF, Int. J. Heat Mass Transfer 45 (2002) 4463–4478.
[50] H. Zhang, I. Mudawar, M.M. Hasan, Investigation of interfacial behavior during the flow boiling CHF transient, Int. J. Heat Mass Transfer 47 (2004) 1275–1288.
[51] C.R. Kharangate, L.E. O'Neill, I. Mudawar, Effects of two-phase inlet quality, mass velocity, flow orientation, and heating perimeter on flow boiling in a rectangular channel: part 1—two-phase flow and heat transfer results, Int. J. Heat Mass Transfer 103 (2016) 1261–1279.
[52] C.R. Kharangate, L.E. O'Neill, I. Mudawar, Effects of two-phase inlet quality, mass velocity, flow orientation, and heating perimeter on flow boiling in a rectangular channel: part 2—CHF experimental results and model, Int. J. Heat Mass Transfer 103 (2016) 1280–1296.
[53] H. Zhang, I. Mudawar, M.M. Hasan, A method for assessing the importance of body force on flow boiling CHF, J. Heat Transfer 126 (2004) 161–168.
[54] G.B. Wallis, One-Dimensional Two-Phase Flow, McGraw-Hill, New York, 1969.
[55] C. Konishi, I. Mudawar, Review of flow boiling and critical heat flux in microgravity, Int. J. Heat Mass Transfer 80 (2015) 469–493.
[56] T. Oka, Y. Abe, Y.H. Mori, A. Nagashima, Pool boiling of n-pentane, CFC-113, and water under reduced gravity: parabolic flight experiments with a transparent heater, J. Heat Transfer 117 (1995) 408–417.
[57] T. Oka, Y. Abe, Y.H. Mori, A. Nagashima, Pool boiling heat transfer in microgravity (experiments with CFC-113 and water utilizing a drop shaft facility), JSME Int. J. 39 (1996) 798–807.
[58] J. Straub, Microscale boiling heat transfer under 0g and 1g conditions, Int. J. Therm. Sci. 39 (2000) 490–497.
[59] J. Straub, Origin and effect of thermocapillary convection in subcooled boiling. Observations and conclusions from experiments performed at microgravity, Ann. N. Y. Acad. Sci. 974 (2002) 348–363.
[60] H. Merte, Momentum effects in steady nucleate pool boiling during microgravity, Ann. N. Y. Acad. Sci. 1027 (2004) 196–216.

[61] H. Merte, Some parameter boundaries governing microgravity pool boiling modes, Ann. N. Y. Acad. Sci. 1077 (2006) 629–649.
[62] J. Kim, J.F. Benton, D. Wisniewski, Pool boiling heat transfer on small heaters: effect of gravity and subcooling, Int. J. Heat Mass Transfer 45 (2002) 3919–3932.
[63] C.D. Henry, J. Kim, A study of the effects of heater size, subcooling, and gravity level on pool boiling heat transfer, Int. J. Heat Fluid Flow 25 (2004) 262–273.
[64] R. Raj, J. Kim, J. McQuillen, Pool boiling heat transfer on the International Space Station: experimental results and model verification, J. Heat Transfer 134 (2012) 1–14.
[65] V.K. Dhir, G.R. Warrier, E. Aktinol, D.F. Chao, J. Eggers, W. Sheredy, W. Booth, Nucleate pool boiling experiments (NPBX) on the International Space Station, Microgravity Sci. Technol. 24 (2012) 307–325.
[66] G. Son, V.K. Dhir, N. Ramanuju, Dynamics and heat transfer associated with a single bubble during nucleate boiling on a horizontal surface, J. Heat Transfer 121 (1999) 623–631.
[67] L. Zhao, K.S. Rezkallah, Gas-liquid flow patterns at microgravity, Int. J. Multiphase Flow 19 (1993) 751–763.
[68] B. Choi, T. Fujii, H. Asano, K. Sugimoto, A study of gas-liquid two-phase flow in a horizontal tube under microgravity, Ann. N. Y. Acad. Sci. 974 (2002) 316–327.
[69] A.E. Dukler, J.A. Fabre, J.B. McQuillen, R. Vernon, Gas-liquid flow at microgravity conditions: flow patterns and their transitions, Int. J. Multiphase Flow 14 (1988) 389–400.
[70] W.S. Bousman, Studies of two-phase gas-liquid flow in microgravity, PhD Thesis, University of Houston, Texas, 1994.
[71] W.S. Bousman, J.B. McQuillen, in: Characterization of annular two-phase gas-liquid flows in microgravity, Proceedings of the Second Microgravity Fluid Physics Conference, Cleveland, Ohio, 1994, pp. 227–232.
[72] W.S. Bousman, J.B. McQuillen, L.C. Witte, Gas-liquid flow patterns in microgravity: effects of tube diameter, liquid viscosity and surface tension, Int. J. Multiphase Flow 22 (1996) 1035–1053.
[73] C. Colin, J. Fabre, A.E. Dukler, Gas-liquid flow at microgravity conditions—I. Dispersed bubble and slug flow, Int. J. Multiphase Flow 17 (1991) 533–544.
[74] C. Colin, J. Fabre, J. McQuillen, Bubble and slug flow at microgravity conditions: state of knowledge and open questions, Chem. Eng. Commun. 141–142 (1996) 155–173.
[75] D. Lee, Thermohydraulic and flow regime analysis for condensing two-phase flow in a microgravity environment, PhD Thesis, Texas A&M University, 1987.
[76] D. Lee, F.R. Best, N. McGraw, in: Microgravity two-phase flow regime modeling, Proceedings of the Third Nuclear Thermal Hydraulics Winter Meeting, Los Angeles, CA, 1987.
[77] T.R. Reinarts, Adiabatic two phase flow regime data and modeling for zero and reduced (horizontal flow) acceleration fields, PhD Thesis, Texas A&M University, 1993.
[78] C. Colin, J. Fabre, A. Kamp, Turbulent bubble flow in pipe under gravity and microgravity conditions, J. Fluid Mech. 711 (2012) 469–515.
[79] L. Zhao, K.S. Rezkallah, Pressure drop in gas-liquid flow at microgravity conditions, Int. J. Multiphase Flow 21 (1995) 837–849.
[80] R.W. Lockhart, R.C. Martinelli, Proposed correlation of data for isothermal two-phase, two-component flow in pipes, Chem. Eng. Prog. 45 (1949) 39–48.
[81] I. Chen, R. Downing, E.G. Keshock, M. Al-Sharif, Measurements and correlation of two-phase pressure drop under microgravity conditions, J. Thermophys. Heat Transfer 5 (1991) 514–523.
[82] J.F. Zhao, H. Lin, J.C. Xie, W.R. Hu, Pressure drop of bubbly two-phase flow in a square channel at reduced gravity, Adv. Space Res. 29 (2002) 681–686.

[83] R. Siegel, C. Usiskin, A photographic study of boiling in the absence of gravity, J. Heat Transfer 81 (1959) 230–236.
[84] M. Misawa, An experimental and analytical investigation of flow boiling heat transfer under microgravity conditions, PhD Thesis, University of Florida, 1993.
[85] M. Saito, N. Yamaoka, K. Miyazaki, M. Kinoshita, Y. Abe, Boiling two-phase flow under microgravity, Nucl. Eng. Des. 146 (1994) 451–461.
[86] H. Ohta, Experiments on microgravity boiling heat transfer by using transparent heaters, Nucl. Eng. Des. 175 (1997) 167–180.
[87] S. Luciani, D. Brutin, C. Le Niliot, O. Rahli, L. Tadrist, Flow boiling in minichannels under normal, hyper-, and microgravity: local heat transfer analysis using inverse methods, J. Heat Transfer 130 (2008) 1–13.
[88] S. Luciani, D. Brutin, C. Le Niliot, O. Rahli, Boiling heat transfer in a vertical microchannel: local estimation during flow boiling with a non intrusive method, Multiphase Sci. Technol. 21 (2009) 297–328.
[89] G.P. Celeta, M. Cumo, M. Gervasi, G. Zummo, Quenching experiments inside 6.0 mm tube at reduced gravity, Int. J. Heat Mass Transfer 52 (2009) 2807–2814.
[90] C. Baltis, G.P. Celeta, M. Cumo, L. Saraceno, G. Zummo, Gravity influence on heat transfer rate in flow boiling, Multiphase Sci. Technol. 24 (2012) 203–213.
[91] D. Brutin, V.S. Ajaev, L. Tadrist, Pressure drop and void fraction during flow boiling in rectangular minichannels in weightlessness, Appl. Therm. Eng. 51 (2013) 1317–1327.
[92] Y. Ma, J.N. Chung, An experimental study of critical heat flux (CHF) in microgravity forced-convection boiling, Int. J. Multiphase Flow 27 (2001) 1753–1767.
[93] H. Zhang, I. Mudawar, M.M. Hasan, Flow boiling CHF in microgravity, Int. J. Heat Mass Transfer 48 (2005) 3107–3118.
[94] C. Konishi, H. Lee, I. Mudawar, M.M. Hasan, H.K. Nahra, N.R. Hall, J.D. Wagner, R.L. May, J.R. Mackaey, Flow boiling in microgravity: part 1—interfacial behavior and experimental heat transfer results, Int. J. Heat Mass Transfer 81 (2015) 705–720.
[95] C. Konishi, H. Lee, I. Mudawar, M.M. Hasan, H.K. Nahra, N.R. Hall, J.D. Wagner, R.L. May, J.R. Mackaey, Flow boiling in microgravity: part 2—Critical heat flux interfacial behavior, experimental data, and model, Int. J. Heat Mass Transfer 81 (2015) 721–736.
[96] W.W. Akers, H.A. Deans, O.K. Crosser, Condensing heat transfer within horizontal tubes, Chem. Eng. Prog. 54 (1958) 89–90.
[97] A. Cavallini, R. Zecchin, A dimensionless correlation for heat transfer in forced convection condensation, Proceedings of the Fifth International Heat Transfer Conference, Tokyo, Japan, vol. 3, 1974.
[98] M.M. Shah, A general correlation for heat transfer during film condensation inside pipes, Int. J. Heat Mass Transfer 22 (1979) 547–556.
[99] K.W. Moser, R.L. Webb, B. Na, A new equivalent Reynolds number model for condensation in smooth tubes, J. Heat Transfer 120 (1998) 410–417.
[100] M.K. Dobson, J.C. Chato, Condensation in smooth horizontal tubes, J. Heat Transfer 120 (1998) 193–213.
[101] W.-W. Wang, T.D. Radcliff, R.N. Christensen, A condensation heat transfer correlation for millimeter-scale tubing with flow regime transition, Exp. Therm. Fluid Sci. 26 (2002) 473–485.
[102] S. Koyama, K. Kuwahara, K. Nakashita, K. Yamamoto, An experimental study on condensation of refrigerant R134a in a multi-port extruded tube, Int. J. Refrig. 24 (2003) 425–432.
[103] X. Huang, G. Ding, H. Hu, Y. Zhu, H. Peng, Y. Gao, B. Deng, Influence of oil on flow condensation heat transfer of R410A inside 4.18 mm and 1.6 mm inner diameter horizontal smooth tubes, Int. J. Refrig. 33 (2010) 158–169.

[104] S.M. Kim, I. Mudawar, Theoretical model for annular flow condensation in rectangular micro-channels, Int. J. Heat Mass Transfer 55 (2012) 958–970.
[105] S.M. Kim, I. Mudawar, Universal approach to predicting two-phase frictional pressure drop for adiabatic and condensing mini/micro-channel flows, Int. J. Heat Mass Transfer 55 (2012) 3246–3261.
[106] S.M. Kim, I. Mudawar, Universal approach to predicting heat transfer coefficient for condensing mini/micro-channel flows, Int. J. Heat Mass Transfer 56 (2013) 238–250.
[107] G.L. Hubbard, A.F. Mills, D.K. Chung, Heat transfer across a turbulent falling film with cocurrent vapor flow, J. Heat Transfer 98 (1976) 319–320.
[108] H. Ueda, R. Moller, S. Komori, T. Mizushima, Eddy diffusivity near the free surface of open channel flow, Int. J. Heat Mass Transfer 20 (1977) 1127–1136.
[109] I. Mudawar, M.A. El-Masri, Momentum and heat transfer across freely-falling turbulent liquid films, Int. J. Multiphase Flow 12 (1986) 771–790.
[110] J.A. Shmerler, I. Mudawar, Local heat transfer coefficient in wavy free-falling turbulent liquid films undergoing uniform sensible heating, Int. J. Heat Mass Transfer 31 (1988) 67–77.
[111] J.A. Shmerler, I. Mudawar, Local evaporative heat transfer coefficient in turbulent free-falling liquid films, Int. J. Heat Mass Transfer 31 (1988) 731–742.
[112] T.H. Lyu, I. Mudawar, Statistical investigation of the relationship between interfacial waviness and sensible heat transfer to a falling liquid film, Int. J. Heat Mass Transfer 34 (1991) 1451–1464.
[113] T.H. Lyu, I. Mudawar, Determination of wave-induced fluctuations of wall temperature and convective heat transfer coefficient in the heating of a turbulent falling liquid film, Int. J. Heat Mass Transfer 34 (1991) 2521–2534.
[114] I. Mudawar, R.A. Houpt, Measurement of mass and momentum transport in wavy-laminar falling liquid films, Int. J. Heat Mass Transfer 36 (1993) 4151–4162.
[115] J.M. Mandhane, G.A. Gregory, K. Aziz, A flow pattern map for gas—liquid flow in horizontal pipes, Int. J. Multiphase Flow 1 (1974) 537–553.
[116] G. Breber, J. Palen, J. Taborek, Prediction of horizontal tube-size condensation of pure components using flow regime criteria, J. Heat Transfer 102 (1980) 471–476.
[117] H.M. Soliman, On the annular-to-wavy flow pattern transition during condensation inside horizontal tubes, Can. J. Chem. Eng. 60 (1982) 475–481.
[118] H.M. Soliman, The mist-annular transition during condensation and its influence on the heat transfer mechanism, Int. J. Multiphase Flow 12 (1986) 277–288.
[119] A. Miyara, K. Nonaka, M. Taniguchi, Condensation heat transfer and flow pattern inside a herringbone-type micro-fin tube, Int. J. Refrig. 23 (2000) 141–152.
[120] Q. Chen, R.S. Amano, M. Xin, Experimental study of flow patterns and regimes of condensation in horizontal three-dimensional micro-fin tubes, Int. J. Heat Mass Transfer 43 (2006) 201–206.
[121] J.A. Olivier, L. Liebenberg, J.R. Thome, J.P. Meyer, Heat transfer, pressure drop, and flow pattern recognition during condensation inside smooth, helical micro-fin and herringbone tubes, Int. J. Refrig. 30 (2007) 609–623.
[122] S.M. Kim, I. Mudawar, Flow condensation in parallel micro-channels—part 2: heat transfer results and correlation technique, Int. J. Heat Mass Transfer 55 (2012) 984–994.
[123] S. Lips, J.P. Meyer, Two-phase flow in inclined tubes with specific reference to condensation: a review, Int. J. Multiphase Flow 37 (2011) 845–859.
[124] D. Barnea, A unified model for predicting flow-pattern transitions for the whole range of pipe inclinations, Int. J. Multiphase Flow 13 (1987) 1–12.
[125] P.L. Spedding, J.J.J. Chen, V.T. Nguyen, Pressure drop in two phase gas-liquid flow in inclined pipes, Int. J. Multiphase Flow 8 (1982) 407–431.

[126] D.H. Beggs, J.P. Brill, A study of two-phase flow in inclined pipes, J. Petrol. Technol. 25 (1973) 607–617.
[127] J.C. Chato, Laminar condensation inside horizontal and inclined tubes, Doctoral Dissertation, Massachusetts Institute of Technology, Cambridge, Massachusetts, 1960.
[128] B.X. Wang, X.Z. Du, Study on laminar film-wise condensation for vapor flow in an inclined small/mini-diameter tube, Int. J. Heat Mass Transfer 43 (2000) 1859–1868.
[129] M.A. Akhavan-Behabadi, R. Kumar, S.G. Mohseni, Condensation heat transfer of R-134a inside a microfin tube with different tube inclinations, Int. J. Heat Mass Transfer 50 (2007) 4864–4871.
[130] T. Nitheanandan, H.M. Soliman, Influence of tube inclination on the flow regime boundaries of condensing steam, Can. J. Chem. Eng. 71 (1993) 35–41.
[131] T. Nitheanandan, H.M. Soliman, Analysis of the stratified/nonstratified transitional boundary in horizontal and slightly inclined condensing flows, Can. J. Chem. Eng. 72 (1994) 26–34.
[132] S. Lips, J.P. Meyer, Experimental study of convective condensation in an inclined smooth tube. Part I: inclination effect on flow pattern and heat transfer coefficient, Int. J. Heat Mass Transfer 55 (2012) 395–404.
[133] H.S. Wang, J.W. Rose, in: Film condensation in microchannels: effect of tube inclination, Proceedings of the ASME 4th International Conference on Nanochannels, Microchannels, and Minichannels, Limerick, Ireland, 2006, pp. 133–137.
[134] H. Saffari, V. Naziri, Theoretical modeling and numerical solution of stratified condensation in inclined tube, J. Mech. Sci. Technol. 24 (2010) 2587–2596.
[135] E. Da Riva, D. Del Col, Effect of gravity during condensation of R134a in a circular minichannel, Microgravity Sci. Technol. 23 (2011) 87–97.
[136] I. Park, L.E. O'Neill, I. Mudawar, Assessment of body force effects in flow condensation, part I: experimental investigation of liquid film behavior for different orientations, Int. J. Heat Mass Transfer 106 (2017) 295–312.
[137] L.E. O'Neill, I. Park, C.R. Kharangate, V.S. Devahdhanush, V. Ganesan, I. Mudawar, Assessment of body force effects in flow condensation, part II: criteria for negating influence of gravity, Int. J. Heat Mass Transfer 106 (2017) 313–328.
[138] H. Lamb, Hydrodynamics, sixth ed., Dover Publications, New York, 1945.
[139] L.M. Milne-Thompson, Theoretical Hydrodynamics, fourth ed., Macmillan, New York, 1960.
[140] H. Lee, I. Mudawar, M.M. Hasan, Experimental and theoretical investigation of annular flow condensation in microgravity, Int. J. Heat Mass Transfer 61 (2013) 293–309.
[141] R.K. Shah, A.L. London, Laminar Flow Forced Convection in Ducts: A Source Book for Compact Heat Exchanger Analytical Data, Academic Press, New York, 1978.
[142] E.R. Van Driest, On turbulent flow near a wall, J. Aeronaut. Sci. 23 (1956) 1007–1011.
[143] W.M. Kays, Heat transfer to the transpired turbulent boundary layer, Int. J. Heat Mass Transfer 15 (1972) 1023–1044.
[144] W.M. Kays, M.E. Crawford, Convective Heat and Mass Transfer, second ed., McGraw-Hill, New York, 1980.